EPFL

Thèse n° 8705

Protein Engineering for Personalized therapy and diagnosis

Présentée le 25 mars 2022

Faculté des sciences et techniques de l'ingénieur
Laboratoire des nanomatériaux supramoléculaires et interfaces - Chaire Constellium
Programme doctoral en science et génie des matériaux

pour l'obtention du grade de Docteur ès Sciences

par

Lixia WEI

Acceptée sur proposition du jury

Prof. Ph. Spätig, président du jury
Prof. F. Stellacci, Prof. L. Tang, directeurs de thèse
Prof. J.-C. Leroux, rapporteur
Prof. J. Hubbell, rapporteur
Prof. R. Mezzenga, rapporteur

École polytechnique fédérale de Lausanne

2022

Acknowledgements

My PhD journey starts with a serious question: "Are you sure you want to do a PhD?" Me: "Yes, I'm always sure, 100%." I still remember the moment of this certainty five years ago. The reason is very simple: because I hate repeated boring daily work.

Applying EPFL PhD program is not easy, it's kinda like a "Game Show", in which we all need to display our capability and specialty in our application materials to earn the "Award (be recruited)". Here the first person I would like to thank is Prof. Holger Frauenrath. As a PhD program director five years ago, he is the person who saw my potential and selected me as a PhD candidate in EPFL. He is also the person who recommends me to my first host lab LBI according to my background. This is how my PhD starts.

My first part of PhD research begins in LBI with Prof. Li Tang. My research topic was focused on "Cancer Vaccine development". On one side, I was very excited about this interesting topic, on the other side, I never expected such big challenges which I was going to meet. It's like you open a pure blank paper starting sketching when you were five years old naive girl, but needs to submit a delicate painting. When intensive training, learning, and practicing become routine, life fuses with work, the 3 am moon looks particularly bright, the stairs to success are closer. Luckily, I was not alone on this journey. Li offered a lot of support on the scientific part, it was harsh, but also very useful later in my career.

I think every PhD has its own unique path, can be relatively lucky, or can be very tough. So, mine is definitely not an easy mode. I had difficulties: stress, anxiety on the research; arguments with PI; insomnia nights by nights; depression... But luckily there are so many nice people surrounded offered their hands. Prof. Karen Scrivener as my PhD mentor and Prof. Dirk Grundler as EDMX PhD program director offered a lot of support during my difficult time. Ms. Nathalie Ritter helped me to manage my stress. And of course, my dear friends: Sailan, Wei, Oh-Hyeon, Céline, Suiyang... and my dear family members: my parents, my sister and my brother-in-law. I would like to thank all of you for your unconditional accompany and trust during this special period.

There is an important person during my PhD that I would like to thank most is Prof. Francesco Stellacci. I still can recall every single detail during our first interview. He

was so relaxed and kind, smiling all the time. And I think I never received so much encouragement compared to before. My torch was lighted up again on my lost way of PhD. This is how I started the second part of my PhD. SuNMIL is a big family with a lot of diversities not only in nationalities but also in research topics. Every group member is pretty open-minded, we can talk, discuss, and form internal collaborations freely. I never experienced such friendly freedom before. And Francesco is always in the role to encourage and support us. Besides, he is the first professor I met who always keeps his office door open no matter how busy he is, we can always step in and talk to him freely, which really makes us feel close to him. I would say this is the first time I experienced doing my research in a happy enjoyable way, and this is definitely credit to Francesco and SuNMIL group members.

Besides, I would particularly mention and thank my colleagues who stand their unique importance to my PhD: Colleen, Quy, Suiyang, and Yong, we shared our internal collaborations, they were really nice and enjoyable time working together. Paulo, Lukasz, Matteo, you were always ready to answer all kinds of questions in the lab, and it was super cool. All together plus the rest: Melis, Cécilia, Chihui, Hanna, Xufeng, Weina, Ting, Francesca, Sujeet, Fiora, Jay, Gadis, Inês, Soumaila, Kerem, Pamina, Heyun, Vincenzo, Laura, Simone, Anna, Camilla, and Ula, it was really nice time to spend together in SuNMIL.

Thirdly, a good PhD research project processing always needs a lot of support internally and externally. Here I would like to thank all of our nice collaborators: Prof. Bruno Correia group, Prof. Daniel Speiser group, and Dr. Valeria Cargo group. Besides, EPFL core facilities definitely play an important role during my PhD research: Flow Cytometry Core Facility (FCCF), Center of PhenoGenomics (CPG), Molecular and Hybrid Materials Characterization Center (MHMC), Interdisciplinary center for Electron Microscopy (CIME), Bioimaging and optics platform (BIOP), Institute of chemical sciences and engineering (ISIC) particularly Dr. Laure Menin, Proteomics Core Facility (PCF) particularly Dr. Diego Chiappe, and Protein Production and Purification (PTPSP) particularly Dr. Kelvin Lau. I really appreciate all your kind support on my PhD research journey.

At the end of this journey, I had my PhD thesis defense. I would like to thank all my jury members: Prof. Jeffrey Hubbell, Prof. Jean-Christophe Leroux, Prof. Raffaele Mezzenga, president Prof. Philippe Spätig, and my two thesis supervisors: Prof. Francesco Stellacci and Prof. Li Tang. All of you spent some time reading my thesis report, listening

to my defense presentation even with your super busy schedule in your daily life. I really appreciate and enjoy the time of Q & A and discussions. Hope we will have a chance to meet each other again in the near future.

Except for the scientific working part, there is another important part during my PhD: my life with family and friends, which completes another half of my PhD. I'm from a small city in big China, but my parents are not the typical traditional parents in China. From my childhood till now, I barely had any restrictions about what I should do according to their preferences, I had a lot of freedom to study what I'm interested in, choose the path I want to go, and date the man I like. As long as I ask for some help, even with difficulties, they always say yes and support me. My sister together with my brother-in-law, they supported me a lot on my long journey from China to France then to Switzerland. I'm really appreciative for all your unconditional support behind me, which makes me as me today.

Secondly, there is one special person that I particularly would like to thank is my boyfriend Siméon. We shared so many similarities, also some cute differences. We enjoy discovering Switzerland together by hiking, climbing, skiing...and we love to cook together, we both like cats so much but at the same time so bad at taking care of plants. We can open our minds discuss and share our opinions in some deep conversations, and also keep making fun of each other in our daily life. I'm so happy to have you walking into my life, which makes it way more colorful. Besides, I also would like to thank all your family members: Ariane, Philippe, Jean-Baptiste, Claire May, Souqui, Francis, Olivier, Cédric... You are always so nice to me, that gives me another home feeling in Switzerland.

At last, I would like to thank all my dear friends in Switzerland: Oh-Hyeon, Edu, Inés, Suiyang, Arnaud, Evelyne, Andreas, Xiangwei, Mei, Nicola, Savanne, Quentin, Sailan, Wei, Yuan, Yi-Ho, Junwen, Jiangtao... You definitely contributed so much to my beautiful PhD life. We enjoy climbing together, skiing together, coffee time, dinner time, and of course, parties. You let me know PhD is not only about research work, but also necessary to enjoy a beautiful life; not only about building a strong mind on work, but also about creating a happy mind in life. I feel I'm so lucky to have you in my PhD journey.

Lausanne, 28-February-2022

Lixia Wei

Abstract

Protein Engineering, especially protein post-translational modification (PTM), extends proteomes in a more complex way than one can expect from analysis of their encoding genomes. It can activate or deactivate certain catalytic functions, add new desired functions, or change some biological activity of the protein. In this thesis work, we use protein engineering tools to show that a number of functions can be engineered to improve protein-based therapeutics.

First, on melanoma cancer vaccine development, we demonstrated a new and versatile nanovaccine platform to address the major challenges in neoantigen cancer vaccine delivery by "polymerizing" the neoepitopes through a reversible polycondensation reaction. Using synthetic long peptide (SLP) bearing a neoepitope and multiple amine groups as one monomer (monomer A) mixed with another reactive bi-functional monomer (monomer B), we prepared a polycondensate neoepitope (PNE) with controlled sizes and responsiveness, which showed superior LN targeting and efficient activation of antigen-presenting cells (APCs). Upon internalization by APCs, redox-responsiveness antigen release facilitated the endosome escape and cytosol delivery of peptide antigens and markedly promoted the cross-presentation, and elicited potent antigen-specific $CD8^+$ T cell responses in immunized mice, therefore, enabling markedly enhanced antitumor efficacy in a prophylactic mouse model.

Second, on antivirals development, we demonstrated a protein-based new and versatile approach for broad-spectrum virucidal material through a one-step reaction by simply chemically conjugating a long flexible and hydrophobic ligand onto the surface of a protein core. Modified proteins reproducibly showed not only effective antiviral inhibition but also a good virucidal effect. Broad-spectrum antiviral inhibition effect was observed against HSV-2, Influenza H1N1, and SARS-CoV-2. Two important key factors, ligand density, and ligand hydrophobic force, significantly influenced antiviral inhibition and virucidal effect. This protein-based antiviral platform provided an easy-manufactured, versatile, broad-spectrum effective, and potentially translatable antiviral solution.

At last, we demonstrated a lipoprotein-cholesterol nanoparticle-based non-invasive cancer diagnosis system. In this preliminary test and proof of concept, lipoprotein-

cholesterol nanoparticles were extracted from 5 melanoma cancer patients' serum by a lab-developed simple and reproducible technique with a high yield. This method successfully eliminated the most abundant inert protein serum albumin and accumulated low abundance proteins, which are usually masked by serum albumins. LC-MS/MS proteomic analysis data indicates within a false discovery rate less than 0.05, differentially expressed proteins, either up-or down-regulated proteins with fold-change over 2, were identified and can potentially be used as cancer biomarkers.

Keywords

protein engineering, polycondensate neoepitope (PNE), cancer vaccine, protein functionalization, broad-spectrum antiviral, virucidal, lipoprotein-cholesterol nanoparticle, non-invasive, cancer biomarker

Résumé

L'ingénierie des protéines, principalement la modification post-traductionnelle, étend les protéomes d'une façon plus complexe que l'analyse de leur génome. L'ingénierie des protéines permet d'activer ou désactiver certaines fonctions catalytiques ou de changer l'activité biologique des protéines. Dans cette thèse, nous utilisons des outils d'ingénierie des protéines pour montrer que certaines fonctions peuvent être conçues pour améliorer les médicaments à base de protéines.

Tout d'abord, en ce qui concerne le développement d'un vaccin contre le cancer du mélanome, nous proposons une nouvelle plateforme nanovaccinale polyvalente permettant de relever les principaux défis liés à l'administration d'un vaccin anticancéreux néoantigène en polymérisant les néoépitopes par une réaction de polycondensation réversible. En utilisant un long peptide synthétique (SLP) portant un néoépitope et de multiples groupes amine comme monomère (monomère A) mélangé à un autre monomère bi-fonctionnel réactif (monomère B), nous avons préparé un néoépitope polycondensé (PNE) avec une taille et une réactivité contrôlée, qui montre un ciblage LN supérieur et une activation efficace des cellules présentatrices d'antigènes (CPA). Lors de l'internalisation par les CPA, la libération de l'antigène sensible à l'oxydoréduction facilite la libération des endosomes et des antigènes polypeptidiques dans le cytosol. Ceci favorise nettement la présentation croisée, et provoque une forte réponse des cellules T CD8+ spécifiques à l'antigène chez les souris immunisées, permettant ainsi une efficacité antitumorale nettement accrue dans un modèle de souris prophylactique.

Deuxièmement, en ce qui concerne le développement d'antiviraux, nous proposons une approche nouvelle et polyvalente à base de protéines pour un matériau virucide à large spectre en conjuguant par voie chimique un long ligand flexible et hydrophobe à la surface d'un noyau protéique. Les protéines modifiées montrent de manière reproductible non seulement une inhibition antivirale efficace mais aussi un bon effet virucide. Un effet d'inhibition antivirale à large spectre a été observé contre le HSV-2, la grippe H1N1 et le SARS-CoV-2. Deux facteurs clés importants, la densité du ligand et la force hydrophobe du ligand, influencent considérablement l'inhibition antivirale et l'effet virucide. Cette

plateforme antivirale à base de protéines constitue une solution antivirale facile à fabriquer, polyvalente, efficace à large spectre et potentiellement transposable.

Enfin, nous proposons un système de diagnostic non invasif du cancer basé sur des nanoparticules de lipoprotéine-cholestérol. Lors des premiers tests, des nanoparticules de lipoprotéine-cholestérol ont été extraites du sérum de 5 patients atteints de mélanome par une technique simple et reproductible développée en laboratoire avec un rendement élevé. Cette méthode permet d'éliminer la protéine inerte la plus abondante, l'albumine sérique, et d'accumuler les protéines en faible abondance, qui sont généralement masquées par les albumines sériques. Les données de l'analyse protéomique LC-MS/MS indiquent qu'avec un taux de fausse découverte inférieur à 0.05, des protéines exprimées de manière différentielle, soit des protéines régulées à la hausse ou à la baisse avec un changement de pli supérieur à 2, peuvent être identifiées et potentiellement utilisées comme biomarqueurs du cancer.

Mots-clés

ingénierie des protéines, néoépitope polycondensé (PNE), vaccin contre le cancer, fonctionnalisation des protéines, antiviral à large spectre, virucide, nanoparticule de lipoprotéine-cholestérol, non invasif, biomarqueur du cancer

List of abbreviations

APC: Antigen Presenting Cell

AFM: Atomic force microscopy

AUC: Analytical ultracentrifugation

BMDCs: Bone-marrow derived dendritic cells

CTLs: Cytotoxic T lymphocytes

CFSE: 5(6) -carboxyfluorescein diacetate N-succinimidyl ester

CDs: Carbon dots

CD: Circular dichroism

CRISPR: Clustered regularly interspaced short palindromic repeats

Cas: CRISPR-associated protein

DC: Dendritic Cell

DMSO: Dimethyl sulfoxide

DLS: Dynamic light scattering

DTT: DL-dithiothreitol

DMPA: N, N′-Dimethyl-1,3-propane diamine

DMHA: N, N′-Dimethyl-1,6-hexane diamine

DMDA: N, N'-Dimethyldodecane-1,12-diamine

DEPs: Differentially expressed proteins

ESIMS: Electrospray ionization mass spectra

EIS: Electrochemical impedance spectroscopy

ECL: Electrochemiluminescence

EDC: 1-Ethyl-3-(3-dimethylaminopropyl) carbodiimide

EVs: Extracellular versicles

FDA: Food and Drug Administration

FPLC: Fast protein liquid chromatography

FET: Field effect transistors

FACS: Fluorescence-activated cell sorting

GPC: Gel permeation chromatography

GM-CSF: Granulocyte-macrophage colony-stimulating factor

GSH: Glutathione

GNPs: Gold nanoparticles

HPV: Human Papillomavirus

HIV/AIDS: Human immunodeficiency virus/acquired immune deficiency syndrome

HSV-2: Herpes simplex virus -2

HBV: Hepatitis B virus

HSPGs: Heparan sulfate proteoglycans

HCC: Hepatocellular carcinoma

HSA: Human serum albumin

HDL: High-density lipoprotein

iDR-NCs: Intertwining DNA-RNA nanocapsules

LN: Lymph Node

LPS: Lipopolysaccharide

LDL: Low-density lipoprotein

MHC: Major histocompatibility complex

MALDI-TOF: Matrix-assisted laser desorption/ionization time-off light

MFI: Mean fluorescence intensity

MW: Molecular weight

MERS: Middle East respiratory syndrome

mtDNA: Mitochondrial DNA

mRNAs: Messenger ribonucleic acids

NHS: N-hydroxysuccinimide

NMR: Nuclear magnetic resonance

NTDs: Neglected tropical diseases

OVA: Ovalbumin

PNE: Polycondensate neoepitope

PBMCs: Peripheral blood mononuclear cells

PD: Proteome Discoverer

PSM: Peptide-spectrum match

PTM: Post-translational modification

PPIs: Protein-protein interactions

pMHC: Peptide-MHC complexes

PEG: Polyethylene glycol

RCR: Rolling circle replication

RCT: Rolling circle transcription

ROS: Reactive oxygen species

RBCs: Red blood cells

SEC: Size-exclusion column

SLPs: Synthetic long peptides

SII: SIINFEKL

SDS-PAGE: Sodium dodecyl sulfate-polyacrylamide gel electrophoresis

SARS: Severe acute respiratory syndrome

SARS-CoV-2: Severe acute respiratory syndrome coronavirus 2

shRNA: Hairpin RNA

TAA: Tumor-associated antigens

TEA: Triethylamine

TLR: Toll-like receptor

TEM: Transmission electron microscope

TB: Tuberculosis

TCPP: Meso-tetra (4-carboxyphenyl) porphyrin

TMT: Tandem mass tag

TMM: Trimmed M-Mean

TME: Tumor microenvironment

UHPLC: Ultra-high-performance liquid chromatography

VAP: Virus-associated protein

VLPs: Virus-like particles

VLDL: Very low-density lipoprotein

Contents

List of Figures

List of Tables

Chapter 1 Introduction of Protein Engineering

Protein Engineering is a process of developing useful or valuable proteins. There are in general two common strategies: rational protein design and directed evolution, but these two methods are not exclusively different.[1] Researchers always apply both based on currently available knowledge of protein structure and its function, and high-throughput screening technology greatly speeds up and expands the abilities of protein engineering. Synthetic protein structures and desired functions can now be rational designed entirely on a computer or produced in a laboratory via directed evolution. Even unnatural amino acids are possible to be included with newly developed methods such as expanded genetic code.[2]

However, another type of protein engineering is termed protein post-translational modification (PTM). It refers to enzymatic, covalent chemical modifications of proteins that typically occur after translating messenger ribonucleic acids (mRNAs). PTMs, as one of the later stages in protein biosynthesis, in other words, is called chemical modifications of a polypeptide chain. It includes enzymatic cleavage of peptide bonds or covalently adding particular desired functional groups, lipids, ligands, carbohydrates, or entire proteins to amino acids "C" or "N" terminals and side chains. The aim of these modifications can usually diversify structures and properties and eventually aim for changing a protein's physical or chemical properties, activity function, localization, interaction, or stability.[3] As a result, PTMs extend proteomes in a more complex way than one can expect from analysis of their encoding genomes. PTMs can be done at any stage of the protein life. If modification is inserted into the polypeptide chain prior to the final step of their folding, it might affect the protein folding efficiency, conformational stability or even lead the protein to a totally new and unknown fate. Most proteins are modified after their folding. It can activate or deactivate certain catalytic functions or add new desired functions; or it changes some biological activity of the protein.

PTMs are widespread nowadays and have important unique roles in regulating many protein functions. Since about half of all proteinogenic amino acids can be modified, and amino acids side chains with functional groups like hydroxyl, amine, carboxyl, or thiol (lysine, arginine, cysteine, tyrosine, histidine, asparagine, aspartate, threonine, and serine) are the most

common modification sites, most PTMs are dynamic and reversible, the modification can be added or removed from the polypeptide chain by specialized enzymes, and some PTMs are irreversible such as lysine acetylation and S-thiolation,[4] thus, the chemical repertoire and information from at the beginning of 20 proteinogenic amino acids can extend into an almost limitless level.

Based on so many possibilities of PTMs, the design of protein-based functional biomaterials that elicit specific cellular behavior -although with a lot of challenges- seems possible with the solution of protein engineering. In recent decades, researchers spent a lot of efforts developing protein-based well-defined, multifunctional materials that can guide cell and tissue behaviors.[5] For instance, incorporating extracellular adhesion ligands or growth factors into protein materials for directing cellular responses, or incorporating pH, thermal, magnetic, photon, etc., stimuli-responsive biomaterials for specific cell-mediated processes or therapy.[6–9] In order to promote these protein-based biomaterials for specific cellular fates, control over both chemical structural properties and biomedical characteristics of the materials is essential.

On biopharmaceuticals, the majority of therapeutic proteins have one or more PTMs. Protein engineering efforts were focused on improving therapeutical efficacy and pharmacokinetic profiles. For instance, dimeric or hexametric insulin structures were developed through alterations of amino acids sequence in the protein associated with propensity regions in order to increase the residence at the injection site for lowing onset therapeutic effect.[10] Another smart insulin modification enables its reversible binding to albumin both at the injection site and in the plasma for prolonged drug release and action of the drug half-life.[11] On cancer immunotherapy, a lot of researchers tried to develop novel drug delivery system or modify immunomodulators for better therapeutic efficacy. For instance, Perego *et al*. conjugated immunotherapeutic drugs with ligands to decrease the "off-target" effect and lower the side-effect;[12] Pan *et al*. developed LyP1 polypeptide-modified outer-membrane vesicle for checkpoint inhibitor PD-1 plasmid delivery to achieve self-blockade of PD-L1 in tumor cells.[13] Besides, a lot of intelligent delivery systems with endogenous stimuli of the tumor microenvironment (TME) such as acidosis, reactive oxygen species (ROS), increased glutathione (GSH), overexpressed enzymes, hypoxia, elevated ATP, etc. were utilized for target delivery of clustered regularly interspaced short palindromic repeats (CRISPR)/CRISPR-associated protein (Cas) systems for enhanced therapeutic effect.[14–16]

Except applying protein engineering to cancer therapy, it also displays unique advantages on infectious disease while combining with nanotechnology. For instance, researchers utilized nonviral virus-like particles (VLPs) to deliver the extracellular domain of matrix protein M2 (M2e) and stem domain of the major envelope glycoprotein hemagglutinin (HA2) via SpyTag/SpyCatcher conjugation to enhance immune response for potential vaccine development.[17] Kang *et al*. also developed another Influenza vaccine platform by genetic engineering of an immunogenic Brucella outer membrane protein BP26 fusion with multiple pieces of influenza M2e self-assembly into adjuvant-free potent versatile vaccine platform.[18] Hoffmann *et al*. generated nanoparticle conjugating with membrane-associated CD4 in order to permit high-avidity binding of trimeric HIV-1 envelope spikes. Another powerful erythroid-specific expression system and transgene codon optimization on engineered red blood cells (RBCs) which expressing viral receptors CD4 or CD4-glycophorin A (GpA) and CCR5 for HIV-1 and expressing ACE2-GpA fusion proteins for SARS-CoV-2 were developed.[19,20]

Another important application for protein engineering is for improvement in diagnosis and sensing. In the recent decade, peptide-functionalized gold nanoparticles (GNPs) showed unique optical and electronic properties; increasing studies have been investigated applying these properties in biomedical detection areas. For instance, CALNN and glutathione (Glu-Cys-Gly) functionalized GNPs were utilized, developing into a colorimetric assay for detecting Pb^{2+} in the presence of living cells.[21] Many enzymes hydrolyze peptide bonds were used to design a detection method for target enzymes,[22,23] and antigenic peptide-functionalized GNPs were utilized for detection of antigen-specific antibodies.[24] Other biomaterials, like peptide-functionalized graphene as a biomimetic live-cell sensor for real-time detection of nitric oxide molecules, for field-effect chemical sensing, for biomarker detection, or like egg albumin based all printed organic humidity sensors, etc. were also being used.[25–28] Besides, Researchers also developed several protein/peptide-responsive (temperature, pH, thermal, light, etc.) polymers conjugations as smart hybrid systems to control enzyme activity and substrate access in sensor development.[29–31]

In this PhD thesis work, we use protein engineering tools on antigen polypeptide for enhancement of immune response for cancer vaccine, on protein for developing non-toxic broad-spectrum antivirals. Besides, we also extracted lipoprotein-cholesterol nanoparticles from serum to improve cancer biomarker detection sensitivity and accuracy. Each chapter presented a protein engineering corrective but independent purposes research work. Rational

designs, manufacturers, characterizations, and biomedical applications were presented respectively below.

1.1 Peptide engineering for personalized cancer vaccine development

In this chapter, a neoantigen cancer vaccine delivery system by “polymerizing” the neoepitopes-based polypeptides through a reversible polycondensation reaction was presented. A lab synthesized bi-functional (NHS) linker was used to crosslink neoepitope-based polypeptides and toll-like receptor immune agonists together into a gel-like nanoparticle with controlled sizes and responsiveness. The product was characterized by multiple tools such as nuclear magnetic resonance (NMR), mass spectrometry, dynamic light scattering (DLS), transmission electron microscopy (TEM), high-performance liquid chromatography (HPLC), gel permeation chromatography (GPC), and SDS-PAGE electrophoresis. This engineered product showed superior lymph node (LN) targeting compared to monomeric antigen peptides due to the increased sizes. Controlled antigen release was rapidly in response to intracellular reduction activity facilitating the endosomal escape and cytosol delivery of peptide antigens and markedly promoted the cross-presentation. Furthermore, it also elicited potent antigen-specific $CD8^+$ T cell responses in immunized mice and expanded the effector memory $CD8^+$ T ($T_{EM)}$ cells, therefore enabling markedly enhanced antitumor efficacy in a prophylactic mouse model.

1.2 Protein engineering for antivirals development

In this chapter, a protein-based novel and versatile approach for broad-spectrum virucidal materials development are presented. We prepared protein functionalized with long flexible hydrophobic ligands using a simple one-step chemical reaction. These modified proteins showed virucidal activity with good safety and effectiveness against viruses in *vitro*. The functionalized proteins were carefully characterized by DLS, Zeta potential, mass spectrometry, circular dichroism (CD), and analytical ultracentrifugation (AUC). In this work, the influence on antiviral inhibition of ligand density, protein core, and ligand length were investigated. As a conclusion, these protein-based antivirals showed less than 1 μM EC_{50} antiviral inhibition against Herpes simplex 2 (HSV-2), Influenza H1N1, and around 2.5 μM EC_{50} inhibition against SARS-CoV-2, besides, one DMDA ligand functionalized protein displayed virucidal effect. Thus, this engineered protein-based antiviral platform provided an easy-manufacture, versatile, broad-spectrum effective, and potentially translatable antiviral solution.

1.3 Lipoprotein-cholesterol nanoparticle for cancer diagnosis

In this chapter, a non-invasive lipoprotein-cholesterol nanoparticles-based cancer diagnosis system is presented. Lipoprotein-cholesterol nanoparticles were extracted from patients' serum after blood clotting by a simple and reproducible method with a high yield. They were characterized by SDS-PAGE electrophoresis, DLS, AUC, and TEM. Proteomics analysis was performed via LC-MS/MS with TMT isobaric labeling. In this preliminary test and proof of concept, we first performed the test with five human patients with melanoma cancer (2 females aged between 30 to 50 and 3 males aged between 25 to 60) together with pooled healthy donors' serum from a commercial source. After confirming our hypothesis, we would expand to a large number of patients, including evaluation of different cancer types, the influence of patients' gender, age, and stage of cancer.

Chapter 2 Peptide Engineering for Enhanced Personalized Cancer Vaccine

Immune system is known as a host defense system comprising many biological structures and processes within an organism that protects against disease through recognizing and attacking foreign invaders. Cancer researchers have long sought to harness this capability to make the immune system recognize tumor-derived antigens and attack tumors. In the past two decades, cancer immunotherapy has made unprecedented progress. In particular, checkpoint blockade and adoptive T cell therapy have shown remarkable clinical results. Cancer vaccine is one of the most studied cancer immunotherapies that has been exploited for more than one hundred years. There are two main types of cancer vaccines: prophylactic cancer vaccine and therapeutic cancer vaccine. Prophylactic cancer vaccines are preventive vaccines such as Human Papillomavirus (HPV) vaccine, which works by preventing an infection that might lead to cancer. A therapeutic cancer vaccine, on the other hand, would be used to treat cancer after it has already appeared.

Compared to the prophylactic vaccine against infectious disease, therapeutic vaccines against cancer have been much less successful. Subunit cancer vaccines, such as protein-, peptide-, or nuclear acid-based vaccines, are also developed to treat malignancies, including pancreatic cancer, melanoma, leukemia, non-small cell lung cancer, prostate cancer, and so on. They also show they augmented anticancer T cell responses in some clinical phase I/II.[32] However, the efficacy of therapeutic cancer vaccine remains modest. So far, there is only one therapeutic cancer vaccine, sipuleucel-T (Provenge®), that has received approval from Food and Drug Administration (FDA).[32,33] This failure can be attributed to several causes, such as immunosuppression by some tumors and ineffective immunologic adjuvants in the vaccine. One of the major causes is inefficient delivery of antigen/adjuvant to secondary lymphoid organs, where immune responses are initiated and orchestrated.[34] In addition, the cellular delivery of antigen to cytosol in antigen-presenting cells for cross-presentation is another major hurdle. Most soluble antigens are proteins, peptides, and nuclear acids with small size (<5 nm), which disseminate into the bloodstream and may be degraded quickly upon parenteral injections.[35] In addition, these antigens are not efficiently internalized by APCs and are almost exclusively loaded on MHC class II molecules failing to elicit potent cytotoxic $CD8^+$ T cell response.[36,37]

Therefore, most current cancer vaccines fail to induce potent and durable immunity against cancer.

A fundamental issue in generating robust immunity with cancer vaccines is the efficient delivery of vaccine components to lymphoid organs. Following injection of soluble protein, peptide, nuclear acids vaccines either intramuscularly or subcutaneously, antigens arrive in the draining lymph nodes (LNs) and will be uptake by LN-resident dendritic cells (DCs) or phagocytosed by migratory DCs, monocytes at the injection sites.[38] LN delivery is key to vaccine potency was shown by studies of intra-LN injections directly of peptide or DNA vaccines, injected directly into LNs are at least 100 fold more potent than the same vaccine administered subcutaneously.[39,40] Although the fate of injected vaccines is a complex interplay of numerous parameters, the physical size of vaccine components plays a significant role in determining the outcome.[41,42] A linear correlation is observed between molecular weight and the fraction of LN uptake up to a threshold of 45 kDa (corresponding to size around 4-5 nm in diameter for a globular protein).[43] Consistent with this finding, unformulated soluble peptides, molecular adjuvants, and small protein antigens show very poor uptake in LNs,[44] besides; soluble small molecule adjuvants often show significant systemic inflammatory toxicity.[45,46]

The size-dependent physiology of lymphatic trafficking has motivated researchers to develop synthetic nanoparticles larger than individual proteins as carriers to deliver peptides, molecular adjuvants, or small proteins to LNs efficiently. As lymphatic endothelium has valve-like openings to enable large particles to enter, and the capillary endothelium is lined by an uninterrupted basement membrane that blocks large macromolecules to transit, to maximize LN targeting becomes a size optimization problem. A serial study by three groups has demonstrated that nanoparticles with diameters under approximately 50 nm can target LN much more efficiently than larger particles. Reddy *et al*.[47] investigated LNs targeting efficiency with three different nanoparticle sizes by injecting dye-labeled 20 nm, 45 nm, and 100 nm poly (propylene sulfide) nanoparticles intradermal for 120 hours LNs sampling. The particle size of 20 nm and 45 nm can always be detected for all the sampling time points; however, particle size with 100 nm cannot be detected. The other two groups, Manolova *et al*.[48] and Fifis *et al*.[49], also reached similar conclusions with virus-like particles and synthetic polystyrene nanoparticles of different sizes for vaccine components delivery. Both groups demonstrated that particles between 20 nm and 40 nm can have more effective LN targeting and trigger the subsequent immune response.

Upon arrival in the LNs, nanoparticles can also have the potential to affect multiple aspects of antigen presentation in antigen-presenting cells (APCs). For instance, nanoparticles designed for co-deliver antigen and adjuvant can promote the cross-presentation of antigens.[50,51] Fang *et al*.[52] developed a method to coat polymer nanoparticles with native tumor cell-derived plasma membranes to enhance the cross-presentation of tumor membrane-associated antigens. Liu *et al*.[44] conjugated peptide antigens and CpG adjuvant to saturated hydrocarbon lipid tails chosen to promote binding to fatty acid-binding pockets of albumin, led around more than 10-fold increase in LN accumulation compared to parent vaccine molecules, and showed significant delay growth of established tumors in therapeutic melanoma and cervical cancer tumor models, while the same doses of traditional peptide/adjuvant vaccines were completely ineffective.

On the other hand, traditionally, cancer vaccines were designed to target tumor-associated antigens (TAAs), which are typically expressed on normal tissues but overexpressed in tumor tissues. Unfortunately, most clinical trials of cancer vaccine targeting TAAs have failed to demonstrate durable benefits compared to standard treatments.[32] In contrast, neoantigens are tumor-specific antigens resulting from somatic mutation, which is only expressed on tumor tissues. Recently, the powerful genomic sequencing technology provided the possibility of identifying neoantigens for vaccines targeting.[53–56] Neoantigens have potential high binding affinity to major histocompatibility complex (MHC) molecules. Neoantigen-based cancer vaccines also have generated great potential advantages of decreasing central immune tolerance and improving safety profile. This enthusiasm largely encouraged cancer researchers to investigate their potential therapeutic efficacy both in preclinical and clinical trials.

In a preclinical melanoma model, Castle *et al*.[57] used 50 validated mutated synthetic long peptides (SLPs) for immunization studies on C57BL/6 mice and two mutated antigens, MUT30 and MUT44, conferred a remarkable in *vivo* antitumor effect in both preventive and therapeutic efficacies. In other tumor models such as sarcoma T3, 4T1, and E0771 breast tumor models, identified specific neoantigens-based cancer vaccines also successfully induced potent anti-tumor immunity.[53] In 2015, Sahin group developed an mRNA vaccine based on neoepitopes which induced more potent cytotoxic T lymphocyte responses than the mRNA vaccines encoding the self-antigens and eradicated the established tumors in mice (Figure 2.1).[58] The promising results from preclinical studies generated great interest for further tests in the clinical trials for neoantigen-based cancer vaccines. Carreno *et al.* [59]. first reported neoantigen

pulsed DCs could induce neoantigen-specific T cell response in melanoma patients. Results from several phases I clinical trials in patients with advanced melanoma were also quite encouraging, especially by Ott *et al*. and Sahin *et al*..[60,61] Currently, there are already seven clinical trials ongoing to evaluate the efficacy of peptide-based neoantigen vaccines in patients with various cancers.[62] These studies show the promising prospect of neoantigen-based cancer vaccines.

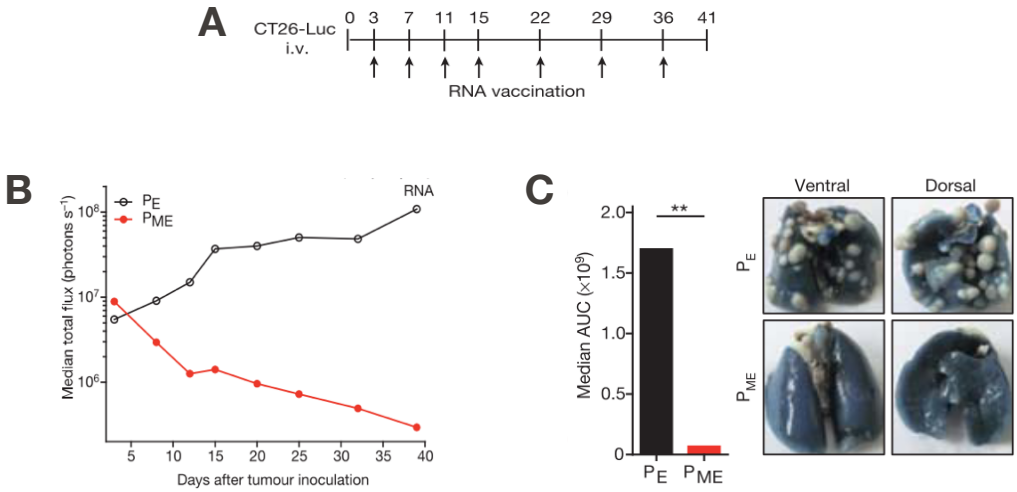

Figure 2.1. mRNA vaccines with mutated epitope confer potent antitumor immunity.

A) Immunization timeline; B) CT26-Luc tumor growth curve at day 40; C) Ink-treated lungs for tumor metastasis.

Despite recent advances, many challenges remain in the development of neoantigen vaccines. Except for the cost and time of the neoantigen identification and manufacture, the inefficient delivery of soluble neoantigen peptides to LNs and cellular cytosol for effective cross-presentation is still the major cause for less potent anti-tumor immunity. In order to address this problem, researchers are actively developing multiple delivery strategies. Zhu *et al*.[63] developed self-assembled intertwining DNA-RNA nanocapsules (iDR-NCs) (Figure 2.2), which can efficiently deliver synergistic adjuvant CpG and short hairpin RNA (shRNA), as well as tumor-specific peptide neoantigens into APCs in LNs for cancer immunotherapy. Through concurrent rolling circle replication (RCR) and rolling circle transcription (RCT), CpG and shRNA self-assembling into DNA-RNA microflowers. These microflowers can further shrink into iDR-NCs by using PEG-grafted cationic polypeptides. Neoantigens can physically

be loaded into iDR-NCs through hydrophobic-hydrophobic interaction. This nanovaccine elicited an 8-fold higher frequency of neoantigen-specific peripheral $CD8^+$ T cells than free neoantigen plus CpG leading to increased tumor regression.

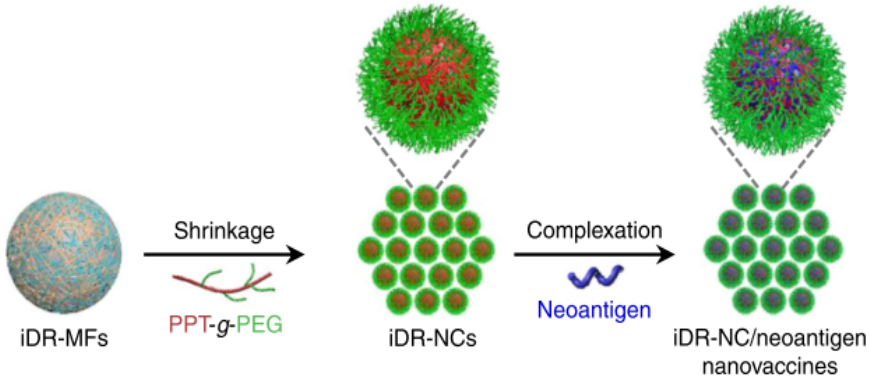

Figure 2.2. Schematics of DNA-RNA nanocapsules (iDR-NCs)/neoantigen nanovaccines for tumor immuno-therapy.

In another elegant example, Kuai *et al*.[64] developed vaccine nanodiscs (Figure 3) for personalized cancer immunotherapy. The nanodiscs that are around 10 nm in size were prepared by self-assembling two lipids, DOPE-PDP and DMPC. Functionalized antigen peptide and adjuvant can be incorporated into this nanodisc through covalent conjugation. These high-density lipoprotein-mimicking nanodiscs coupled with antigen peptides and adjuvants realized antigen/adjuvant co-delivery to LNs and sustained antigen presentation in dendritic cells. Strikingly, these nanodiscs elicited up to 47-fold greater frequencies of neoantigen-specific CTLs than soluble vaccines and even 31-fold greater than soluble vaccines carried by montanide, which is considered as the strongest adjuvant in clinical trials.[65]

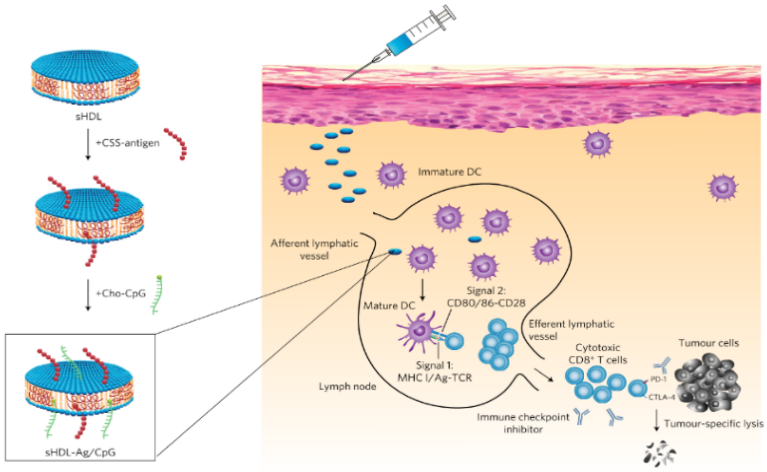

Figure 2.3. Design of synthetic high-density lipoprotein (sHDL) nanodisc platform for personalized cancer vaccines.

Here, we demonstrated a new and versatile nanovaccine platform to address the major challenges in neoantigen cancer vaccine delivery by "polymerizing" the neoepitopes-based polypeptides through a reversible polycondensation reaction. Using SLP bearing a neoepitope and multiple amine groups as one monomer (monomer A) mixed with another reactive bi-functional monomer (monomer B), we prepared a polycondensate neoepitope (PNE) with controlled sizes and responsiveness (Figure 2.4), which showed superior LN targeting compared to monomeric SLP due to the increased sizes of PNEs. Molecularly defined adjuvants, such as toll-like receptor (TLR) ligands that bear the same functional groups, were co-polymerized for the co-delivery with antigens to LNs for efficient activation of APCs. Upon internalization by APCs, PNE released neoepitopes rapidly in response to intracellular reduction activity facilitating the endosomal escape and cytosol delivery of peptide antigens and markedly promoting the cross-presentation. We found PNE elicited potent antigen-specific $CD8^+$ T cell responses in immunized mice and expanded the effector memory $CD8^+$ T (T_{EM}) cells to 22.8-fold greater number than the vaccine of equivalent dose delivered by Montanide emulsion (arguably the most potent vaccine adjuvant used in the clinic to date[64–66]), therefore enabling markedly enhanced anti-tumor efficacy in a prophylactic mouse model.

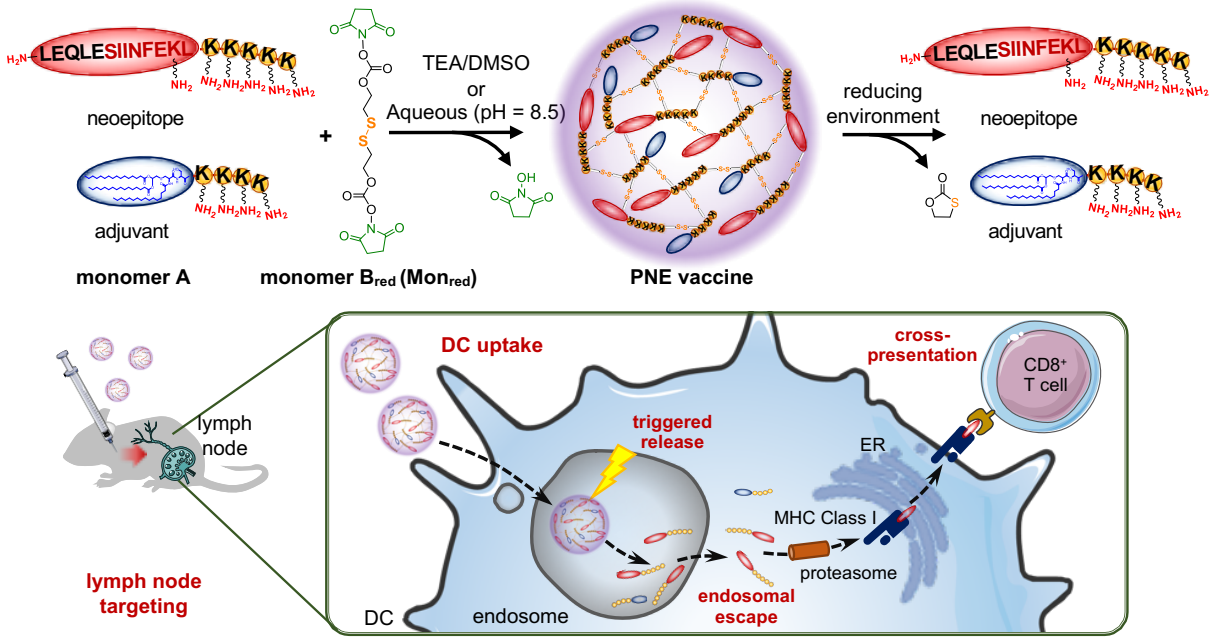

Figure 2.4. Schematic illustration of the synthesis, responsive release, and in *vivo* fate of polycondensate neoepitope (PNE) vaccines.

2.1 Synthesis and Characterization

Since molecular weight (size) has been reported as a key factor that determines the passive distribution of proteins to blood circulation versus lymphatic circulation upon parenteral injections, we sought to co-polymerize the SLP neoantigens and adjuvants through a reversible polycondensation reaction in order to increase the molecular weight and size to target lymphoid organs as illustrated in Figure 2.4. To prove the concept, we first used an SLP containing SIINFEKL (SII), the CD8 epitope of ovalbumin (OVA), as a model neoantigen (LEQ, Table 2-1, Entry 1, the detailed composition and reaction conditions were listed in Table 2-2), which was modified with multiple amine groups by adding flanking lysine residues (monomer A, Figure 2.4). An amine-reactive bi-functional monomer B bearing a disulfide and two N-hydroxysuccinimide (NHS) groups (Mon$_{red}$) were synthesized for the polycondensation reaction (Figure 2.4; Figure 2.6).

Table 2-1. Physicochemical properties of PNE vaccines.

Entry	PNE	Monomer A		Monomer B	Size[a] (nm)
		Antigen (epitope)	Adjuvant		
1	PNE(LEQ)	LEQLESIINFEKLK_5	~	Mon_{red}	8.14 ± 1.54
2	PNE(LEQ-Pam)	LEQLESIINFEKLK_5	Pam_3CSK_4	Mon_{red}	18.69 ± 3.14
3	Non-deg. PNE(LEQ-Pam)	LEQLESIINFEKLK_5	Pam_3CSK_4	Mon_{BS3}[b]	45.97 ± 5.70
4	PNE(LEQLEK_5-Pam)	LEQLEK_5AAYSIINFEKL	Pam_3CSK_4	Mon_{red}	13.62 ± 1.41
5	PNE(K_5LEQ-Pam)	K_5LEQLEAAYSIINFEKL	Pam_3CSK_4	Mon_{red}	21.32 ± 3.04
6	PNE(ELE-Pam)	ELEK_5AAYASMTNMELM	Pam_3CSK_4	Mon_{red}	12.48 ± 1.06
7	PNE(CSV)	CSVYDFFVWLK_5	~	Mon_{red}	8.90 ± 1.10
8	PNE(CLC)	CLCPGNKYEMK_5	~	Mon_{red}	7.40 ± 1.10
9	PNE(LEQ-CpG)	LEQLESIINFEKLK_5	CpG[c]	Mon_{red}	24.97 ± 4.40

[a] Diameter of the PNEs were characterized by DLS

[b] Mon_{BS3}: bis(sulfosuccinimidyl)suberate

[c] Amine functionalized CpG (5'-/5AmMC6/TCCATGACGTTCCTGACGTT/3AmMO/-3)

SD here corresponds to the size distribution profile.

Table 2-2. Synthesis and characterizations of PNEs.

Entry	PNE	Monomer A		Monomer B	mole ratio (A_{ag} : A_{adj} : B)	Antigen Loading efficiency [1]	Loading capacity[2]		Preparation phase[3]
		Antigen (epitope)	Adjuvant				Antigen	Adjuvant	
1	PNE(LEQ)	LEQLESIINFEKLK$_5$	~	Mon_{red}	1 : 0 : 3	97.5%	62.9 %	~	DMSO
2	PNE(LEQ-Pam)	LEQLESIINFEKLK$_5$	Pam_3CSK_4	Mon_{red}	4 : 1 : 20	> 99%	46.4 %	7.9%	DMSO
3	Non-deg. PNE(LEQ-Pam)	LEQLESIINFEKLK$_5$	Pam_3CSK_4	Mon_{BS3}	4 :1 : 80				PBS
4	PNE(LEQLEK$_5$-Pam)	LEQLEK$_5$AAYSIINFEKL	Pam_3CSK_4	Mon_{red}	4 : 1 : 12	96.5%	59%	9.2%	PBS
5	PNE(K$_5$LEQ-Pam)	K$_5$LEQLEAAYSIINFEKL	Pam_3CSK_4	Mon_{red}	4 : 1 : 12				DMSO
6	PNE(ELE-Pam)	ELEK$_5$AAYASMTNMELM	Pam_3CSK_4	Mon_{red}	4 : 1 : 12				DMSO
7	PNE(CSV)	CSVYDFFVWLK$_5$	~	Mon_{red}	1 : 0 : 3				PBS
8	PNE(CLC)	CLCPGNKYEMK$_5$	~	Mon_{red}	1 : 0 : 1				PBS
9	PNE(LEQ-CpG)	LEQLESIINFEKLK$_5$	CpG	Mon_{red}	4 : 1 : 12	> 99%	43.1 %	31.4%	PBS

[1] Loading efficiency was calculated by conjugated antigen peptides in PNE / total antigen peptides added ×100% based on UHPLC characterizations.

[2] Loading capacity was calculated by the weight of conjugated antigen peptides or adjuvants in PNE / total PNE weight × 100%. Weight of conjugated peptide antigen was determined by the feeding amount and the loading efficiency; adjuvant and monomer B were assumed for quantitative loading as non-detectable free adjuvant or monomer B was found in UHPLC characterizations.

[3] Depending on the solubility of peptides and adjuvants, synthesis of PNEs can be done in DMSO or aqueous solution. The aqueous solution is phosphate-buffered saline (PBS) with adjusted pH = 8.5 with Na_2CO_3).

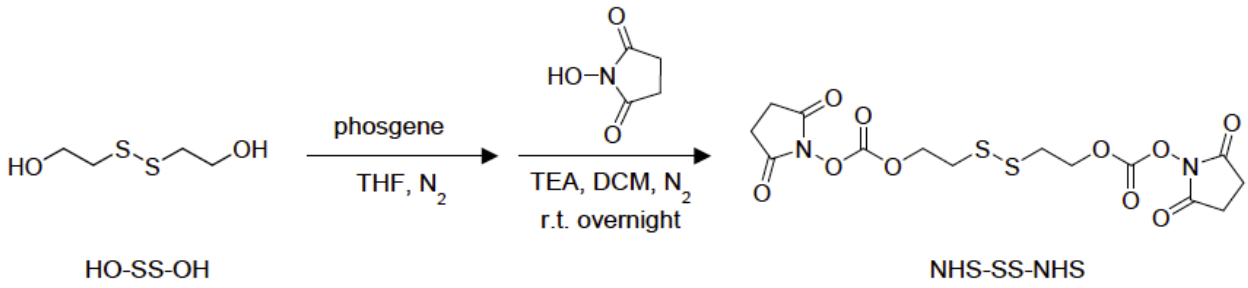

Figure 2.5. Synthesis scheme of bi-functional Mon_{red}.

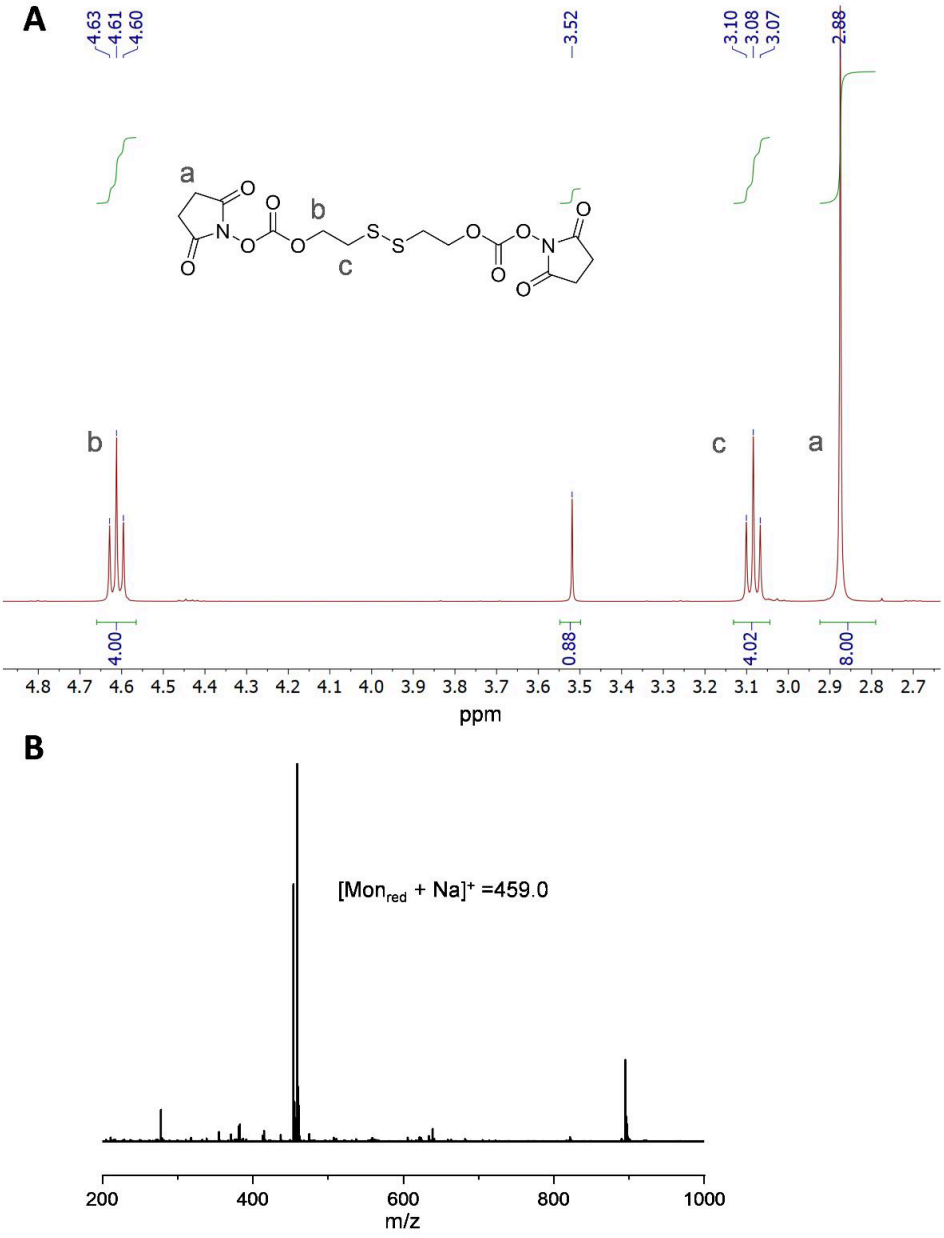

Figure 2.6. Characterizations of molecular Mon_{red} by NMR and MS.

A) ^{1}H NMR spectrum of Mon_{red}; B) ESI-MS spectrum of Mon_{red}.

In order to prepare the nanovaccine, we first mixed monomer A (SLP only) and monomer B in anhydrous dimethyl sulfoxide (DMSO) to prepare the PNE with responsiveness to reduction activity. Triethylamine (TEA) was added as a catalyzer to initiate the polycondensation. The PNE(LEQ) polymer was successfully prepared, evidenced by broadened peaks as compared to the peptide monomer in a ^{1}H NMR spectrum (Figure 2.7) and MW increase shown in traces in ultra-high-performance liquid chromatography (UHPLC) equipped with a size-exclusion column (SEC) (Figure 2.9A). PNE(LEQ) exhibited an average hydrodynamic diameter of 8.14 ± 1.54 nm characterized by dynamic light scattering (DLS) and transmission electron microscope (TEM) (Table 2-1, Entry 1; Table 2, Entry 1; Figure 2.8).

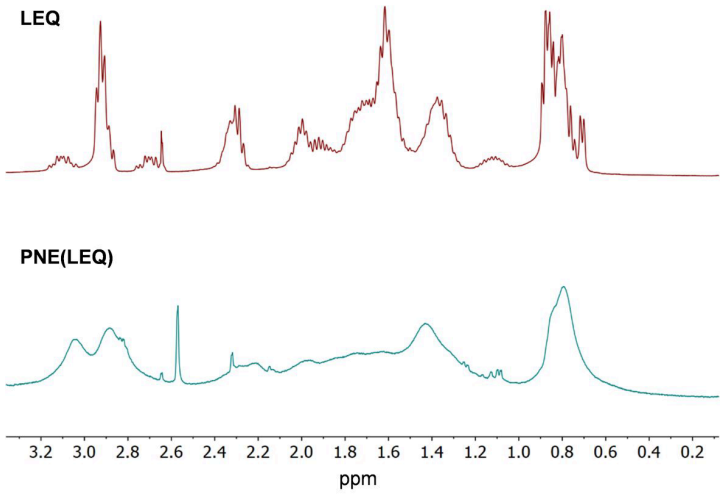

Figure 2.7. ^{1}H NMR spectrum of LEQ and PNE(LEQ).

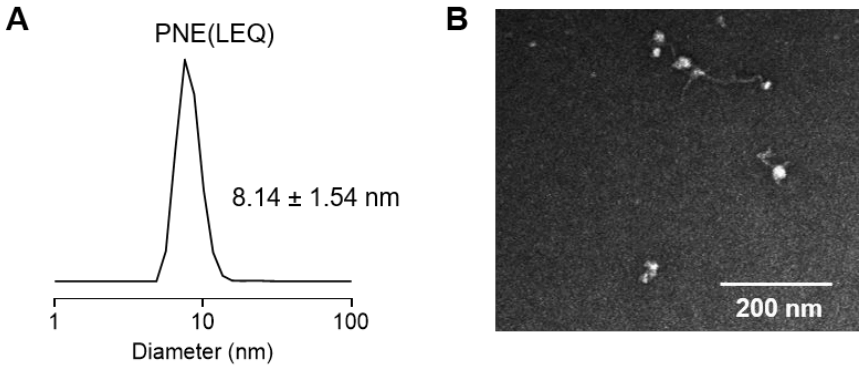

Figure 2.8. Characterizations of PNE(LEQ) nanoparticles by DLS and TEM.

A) Size and size distribution of PNE(LEQ) measured by DLS; B) Representative TEM image of PNE(LEQ).

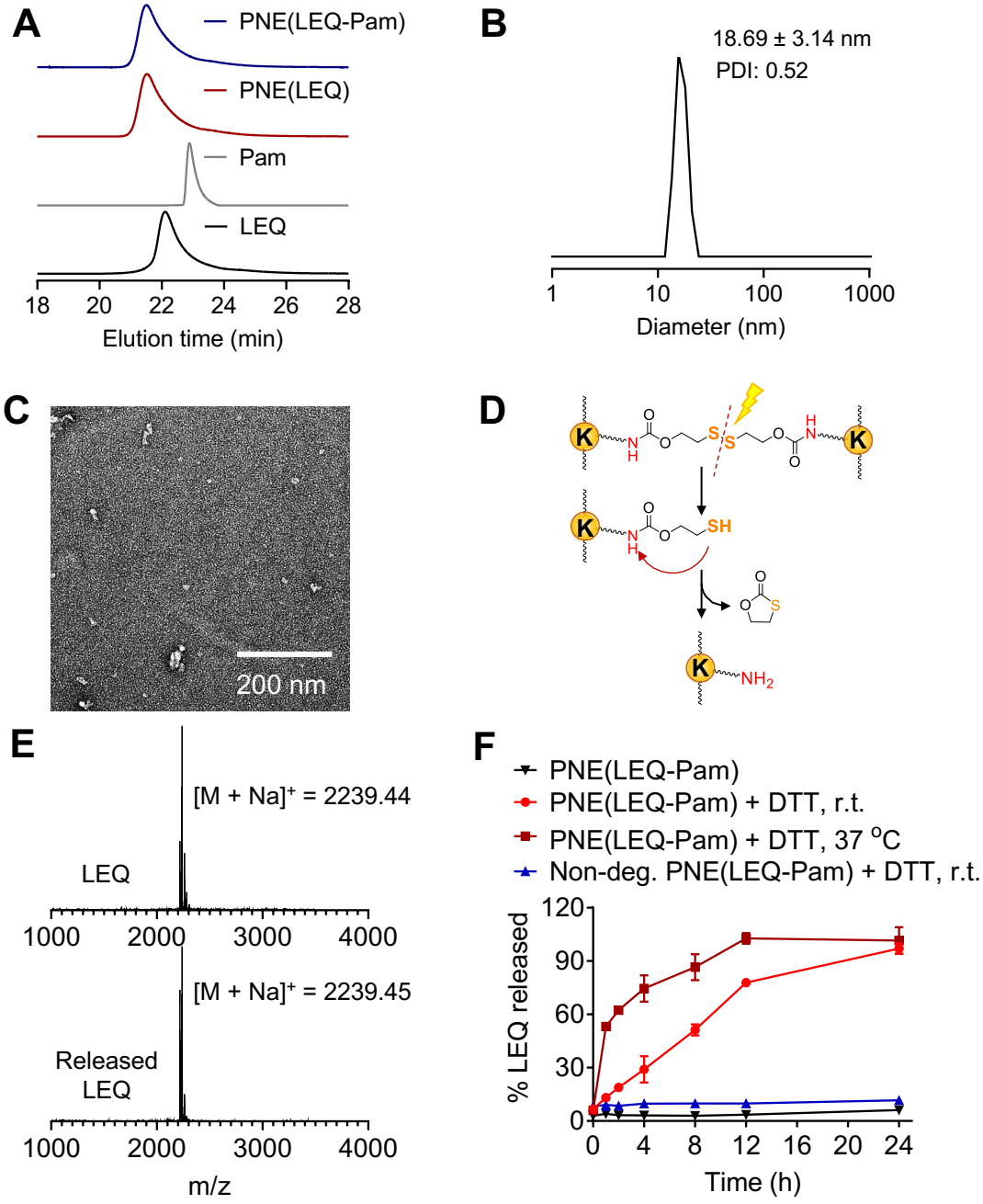

Figure 2.9. Characterizations of PNE vaccines.

A) UHPLC SEC traces of LEQ, Pam, PNE(LEQ), and PNE(LEQ-Pam), detected by UV absorption at a wavelength of 220 nm; B) Size and size distribution measurement of PNE(LEQ-Pam) by DLS; C) TEM imaging of PNE(LEQ-Pam); D) Scheme of the redox-responsive release of antigens or adjuvants from PNE(LEQ-Pam); E) Matrix-assisted laser desorption/ionization time-off-light (MALDI-TOF) mass spectrometric analysis of native and released LEQ from PNE(LEQ-Pam); F) Release kinetics of LEQ from PNEs in the presence or absence of a reducing agent DTT (2 mM).

Co-delivery of antigens and adjuvants to the same endosomal/phagosome compartment of an APC has been shown to be essential for physically instructing DCs to present the foreign antigens.[67] We next copolymerized LEQ and Pam_3CSK_4 (Pam), a TLR1/2 agonist as a molecular adjuvant, with Mon_{red} forming a self-adjuvanted PNE(LEQ-Pam) (Figure 2.4). Pam was selected as it bears multiple amine groups facilitating the direct polycondensation with Mon_{red} and has been shown to potently amplify T cell priming when conjugated with peptides.[68–71] PNE(LEQ-Pam) showed increased MW compared to the monomers as observed in both characterizations of UHPLC-SEC (Figure 2.9A) and gel permeation chromatography (GPC) (Figure 2.10A), suggesting the successful copolymerization. Further, a negligible amount of both monomers (LEQ and Pam) was detected by HPLC equipped with a C18 column (Figure 2.10B, C) or sodium dodecyl sulfate-polyacrylamide gel electrophoresis (SDS-PAGE) (Figure 2.11), indicating a quantitative monomer conversion. Together, >99% incorporation efficiency and remarkably high loading capacity of cargos (~46.4% of dry weight was LEQ, and 7.9% was Pam, Table 2-2, Entry 2) have been achieved with the PNE platform. In addition, the as-prepared PNE(LEQ-Pam) had a relatively homogeneous size with a mean hydrodynamic diameter of 18.69± 3.14 nm (Table 2-1, Entry 2; Figure 2.9B, C).

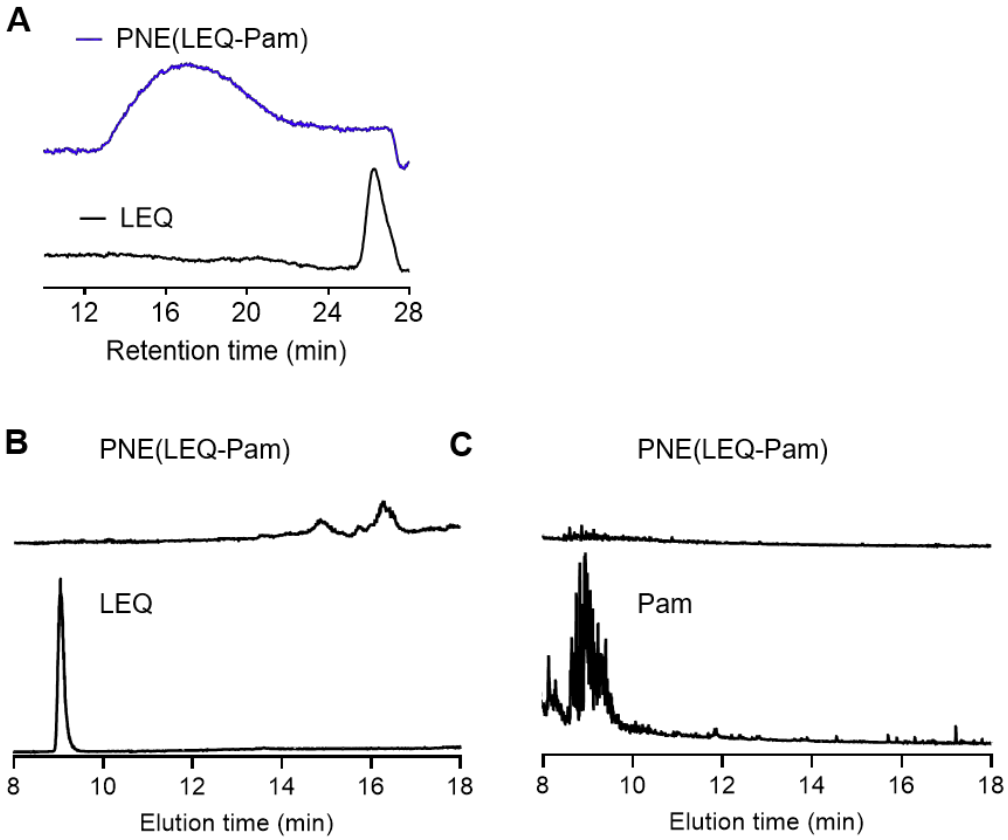

Figure 2.10. GPC and HPLC chromatographic analyses of PNEs.

A) GPC traces showing the MW increase of PNE(LEQ-Pam) compared with free LEQ; B, C) UHPLC-C18 chromatographic traces showing negligible free LEQ or Pam left to post the polycondensation reaction in the synthesis of PNE(LEQ-Pam).

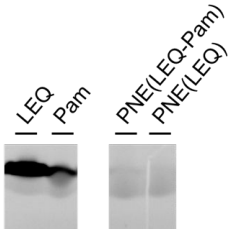

Figure 2.11. SDS-PAGE analyses of free LEQ, Pam, PNE(LEQ-Pam), and PNE(LEQ).

PNE was designed to be degraded in response to intracellular reduction activity, facilitating a traceless release of intact peptide antigens through a self-immolated reaction (Figure 2.4; Figure 2.9D) for unaltered processing and presentation of the designed subunit antigens. Released LEQ peptide from PNE(LEQ-Pam) shared the same MW as the original LEQ peptide providing evidence of releasing unmodified peptide antigens without any residue chemical groups (Figure 2.9E). Consistent with the expectations, reducing agents, such as dithiothreitol (DTT) (Intracellular reducing agent GSH usually found in cytosol around 10 mM, in endosome and lysosome the typical ratio GSH/GSSG is around 1 : 1 to 3 : 1, here we use 2 mM DTT to mimic intracellular GSH environment), accelerated the release of LEQ from the PNE at both room temperature (rt) and 37 ℃ (Figure 2.9F), whereas PNE prepared with a non-degradable monomer B (non-deg. PNE(LEQ-Pam)) (Table 2-1, Entry 3; Figure 2.12) showed no detectable release of antigens even in the presence of DTT (Figure 2.9F). The intracellular traceless release of antigens could be important for the efficient antigen processing and presentation by DCs.[72]

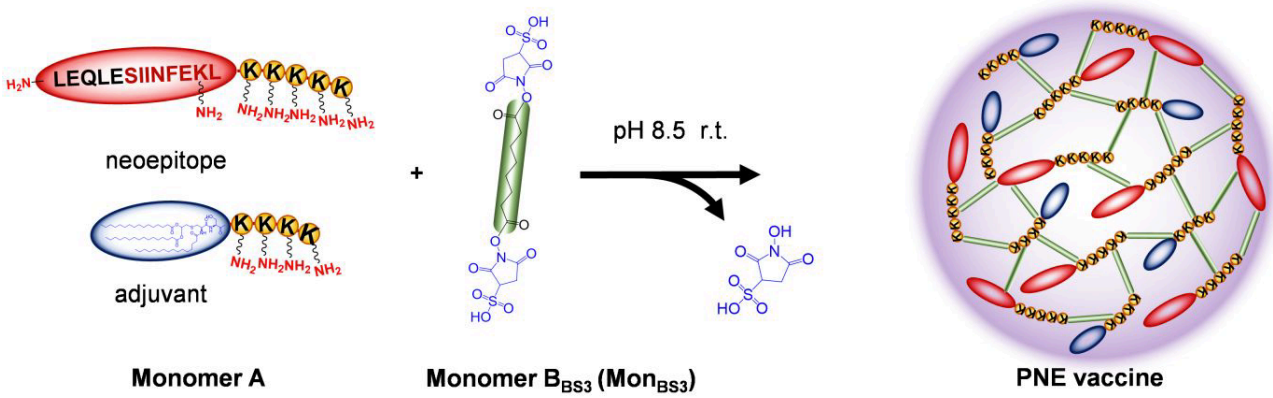

Figure 2.12. Schematic illustration of the synthesis of non-degradable PNE(LEQ-Pam).

To test the versatility, we have extended the preparation of PNEs to a number of peptide antigens with diverse structures and properties, including neoantigens identified from mouse tumors (Table 2-1; Table 2-2). We found the successful formation of PNEs was independent of the sequence or the position of flanking amino acids next to the epitope (Table 2-1, Entry 2, 4-5), or the sequence of epitope itself (Table 2-1, Entry 2, 6-8; including neoantigens identified from MC38 murine colorectal cancer or B16F10 murine melanoma), or the adjuvant molecules (Table 2-1, Entry 2, 9; triacylated lipopeptide Pam_3CSK_4 can be replaced by amine-functionalized CpG oligodeoxynucleotide). Depending on the properties of SLP antigens and adjuvants, the PNE synthesis could be done in DMSO (Table 2-2, Entry 1-2, 5-6) or aqueous solution (Table 2-2, Entry 3-4, 7-9). The amine group was chosen as the chemical handle for the polycondensation due to the ease of adding flanking lysines during the peptide synthesis without significantly changing the properties of SLPs. The amine-NHS conjugation-based polycondensation was rapid and highly efficient in DMSO or aqueous solution at ambient conditions providing PNE a highly versatile and potentially scalable platform for diverse epitopes.

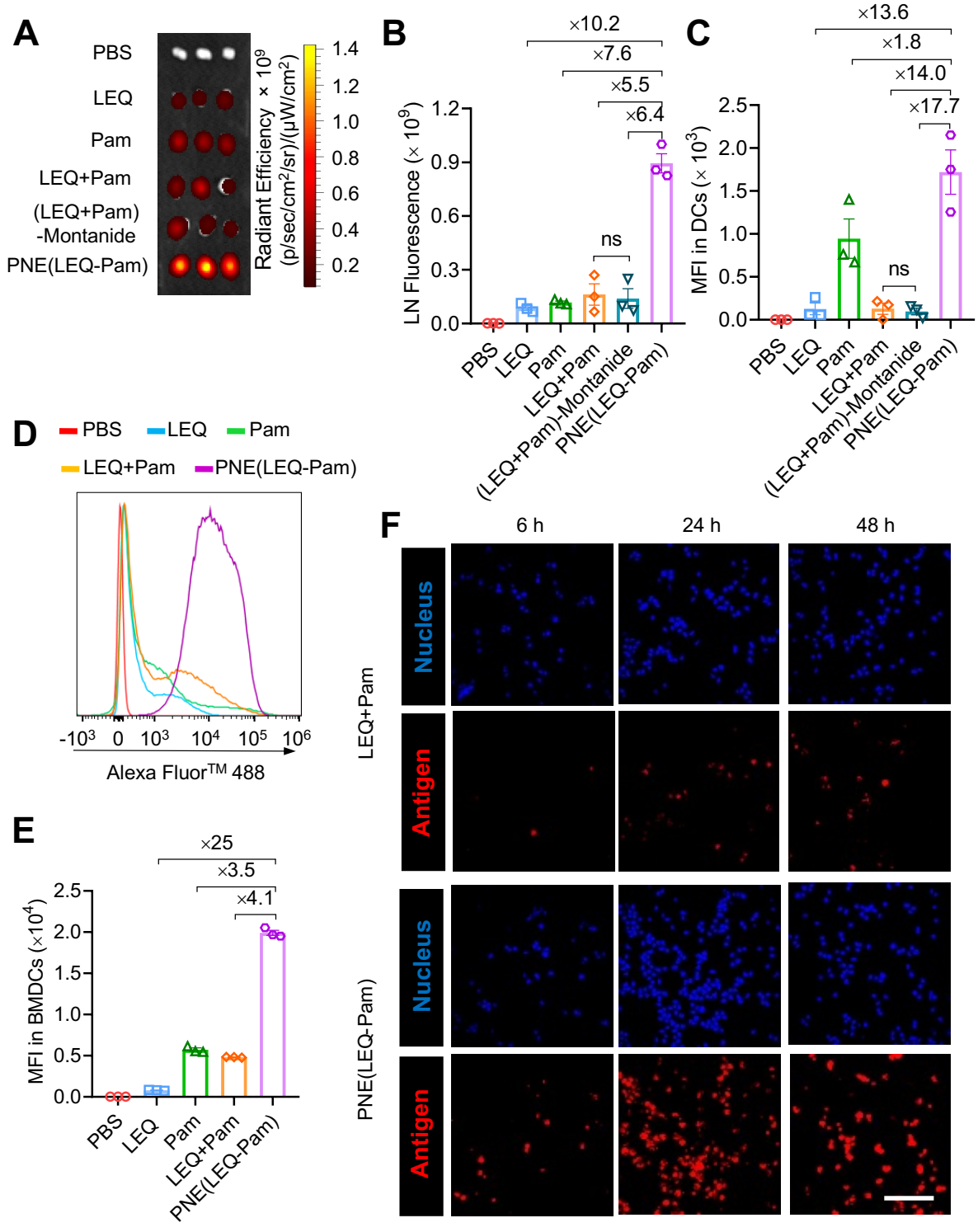

Figure 2.13. Lymph node (LN) and DC targeting of PNE(LEQ-Pam) vaccines in *vivo*.

A) IVIS fluorescence imaging and B) quantification of vaccines accumulated in inguinal draining LNs; C) MFI of fluorescence signal in vaccines that were internalized by DCs in the inguinal LNs; D) Representative flow cytometry histograms of Alexa Fluor™ 488 labeled vaccines that were

internalized by BMDCs; E). MFI of internalized vaccine formulations by BMDCs; F) Confocal microscopy images of BMDCs antigen uptake. Scale bar: 40 μm.

2.2 PNE LN Targeting and accumulation efficiency

We next investigated the targeting efficiency of the responsive PNEs to LNs. Free SLP, adjuvant, or the mixture of two in the presence or absence of Montanide, or PNE(LEQ-Pam) labeled with the equivalent amount of fluorescence dye Alexa Fluor™ 647 was injected subcutaneously into C57BL/6 mice at the tail base. Twenty-four hours later, the draining LNs were excised for whole-tissue fluorescence imaging and measurement. Monomeric SLP or adjuvant or the simple mixture of two showed limited accumulation in LNs (Figure 2.13A, B, Figure 2.14). Formulation of LEQ+Pam in Montanide ((LEQ+Pam) -Montanide) did not improve the LN targeting of the vaccine. By contrast, vaccines delivered by PNE exhibited remarkably high LN accumulation, reaching a level that was 10.2-, 7.6-, and 5.5-fold greater than free SLP, adjuvant, and the simple mixture of two, respectively. The efficient and fast (within 24 hours) LN targeting of PNE can be attributed to the well-controlled small size (~20 nm in diameter), which permits the rapid trafficking to lymphoid organs through afferent lymph.[41,73–75]

After confirming LNs targeting efficiency, next step, we assessed the efficiency of antigen capture by the APCs in LNs by flow cytometry. DCs are critical APCs that efficiently process internalized antigens into peptide-MHC complexes (pMHC), which are required for eliciting T cell immune responses.[76,77] PNE vaccine was captured efficiently by the DCs ($CD11c^+$) in LNs with 14.0- and 17.7-fold higher mean fluorescence intensity (MFI) than that of the mixture of free SLP and adjuvant in the absence or presence of Montanide, respectively (Figure 2.13C). The antigen capture was further examined in *vitro* with bone-marrow-derived dendritic cells (BMDCs). Similar to the in *vivo* results, PNE(LEQ-Pam) exhibited a substantially higher level of antigen internalization compared to the simple mixture LEQ+Pam (Figure 2.13D, E, F). Slightly higher DC internalization of free Pam compared to free LEQ was likely due to the fact that Pam could be self-assembled into some nanosized structures. In general, nano-vaccines are known to be internalized more efficiently by APCs than soluble subunit vaccines.[41,78] As a conclusion, PNE efficiently delivers neoantigen vaccines to LNs and DCs for antigen capture and presentation.

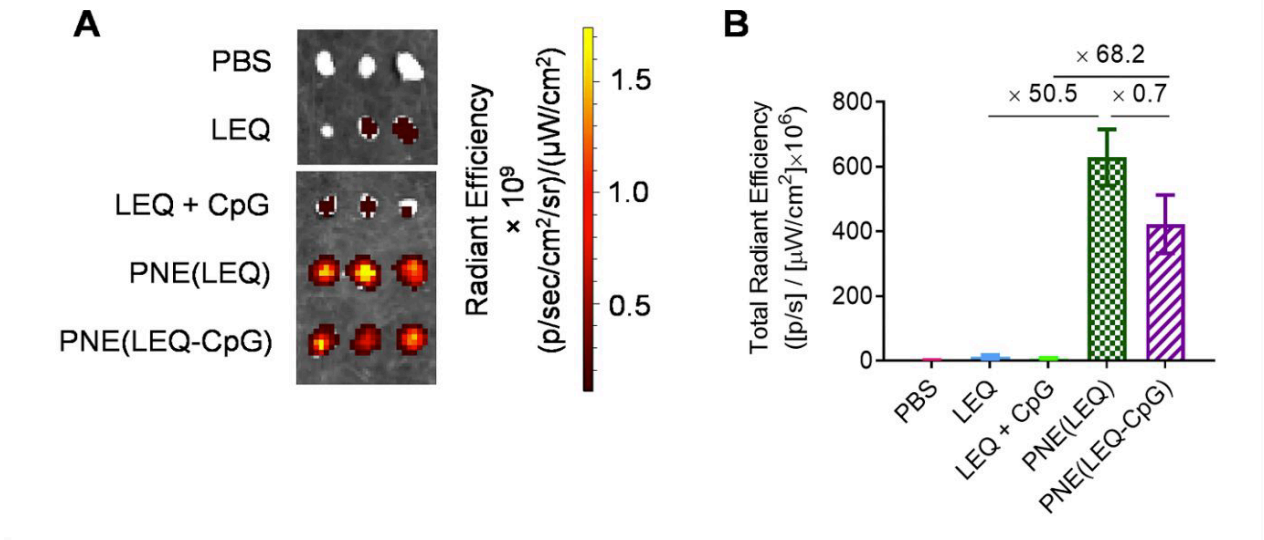

Figure 2.14. Fluorescence imaging (A) and quantification (B) of inguinal draining LNs excised from mice treated with PNEs with and without adjuvants.

2.3 PNE Antigen Cross-presentation

Next, we examined the impact of the PNE platform on antigen cross-presentation. DC maturation is critical for both DC functions, including antigen presentation and expression of co-stimulatory molecules that are required for T cell stimulation. We collected BMDCs from C57BL/6 mice to assess the capacity of PNEs in converting immature DCs into mature DCs in *vitro* by monitoring the expression level of co-stimulatory markers (CD40 and CD80) with flow cytometry analysis (Figure 2.15A, Figure 2.16). PNE with co-polymerized Pam promoted the stimulation of BMDCs to a similar level as monomeric Pam or the mixture of free LEQ and Pam. Importantly, BMDCs pulsed with PNE(LEQ-Pam) cross-primed the SII-antigen-specific naïve OT-1 $CD8^+$ T cells with a greatly enhanced efficiency compared to monomeric SII or LEQ, or the simple mixture of short or long peptides with Pam, assessed by a 5(6) -carboxyfluorescein diacetate N-succinimidyl ester (CFSE) dilution assay (Figure 2.15B, C). We found the redox-responsiveness of the PNE was crucial for enhanced cross-presentation as non-deg. PNE(LEQ-Pam) exhibited substantially lower efficiency of cross-priming of OT-1 $CD8^+$ T cells (Figure 2.17).

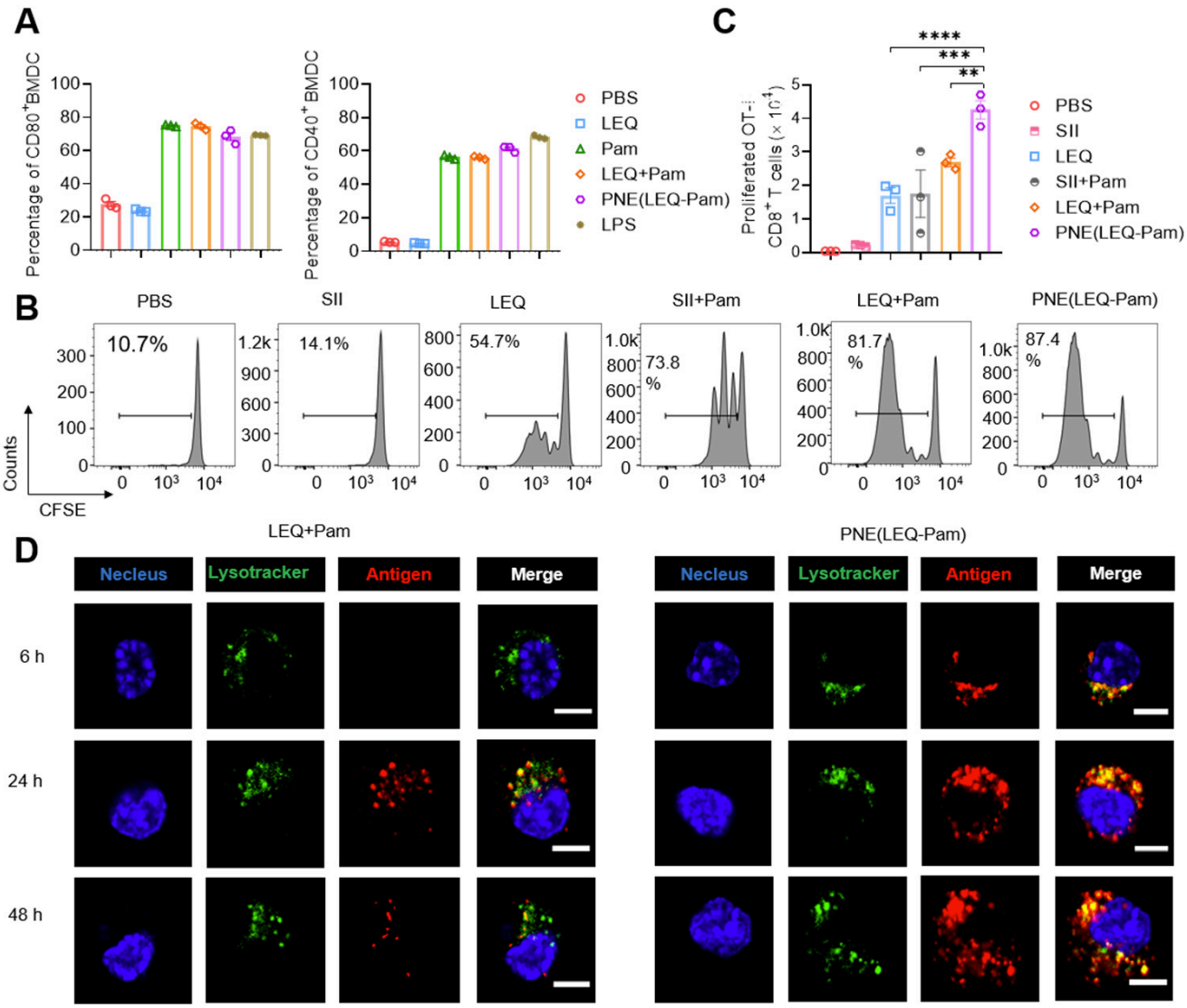

Figure 2.15. In *vitro* BMDC maturation and antigen cross-presentation.

A) Frequencies of BMDCs expressing maturation markers (CD80 and CD40) treated with PNE(LEQ-Pam) vaccine or other indicated formulations; B) Representative flow cytometry plots showing CFSE dilution and gating of the proliferated OT-1 $CD8^+$ T cells co-cultured with BMDCs pulsed with PNE or other indicated formulations. Naïve OT-1 T cells were labeled with CFSE (1 μM for 10 million cells) at the beginning of the assay; C) Counts of proliferated OT-1 $CD8^+$ T cells. *P < 0.05; ** P < 0.01; *** P < 0.001; **** P < 0.0001; D) Confocal microscopic images of BMDCs incubated with fluorescently labeled PNE(LEQ-Pam) or the mixture of free LEQ and Pam. LEQ was labeled with Alexa Fluor™ 647 (red); the endolysosomes were stained with LysoTracker (green); the nuclei were stained with Hoechst (blue). Scale bar: 5 μm.

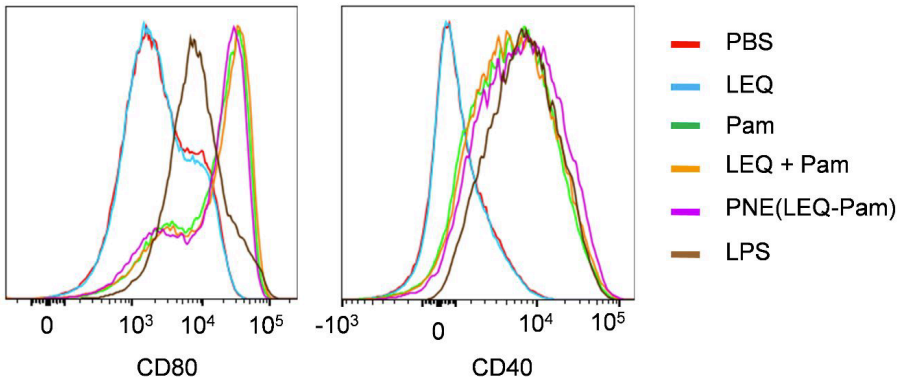

Figure 2.16. Flow cytometry analyses of the activation of BMDCs treated with PNE(LEQ-Pam) vaccine or other indicated formulations.

Shown are the histogram of CD80 and CD40 expression of BMDCs.

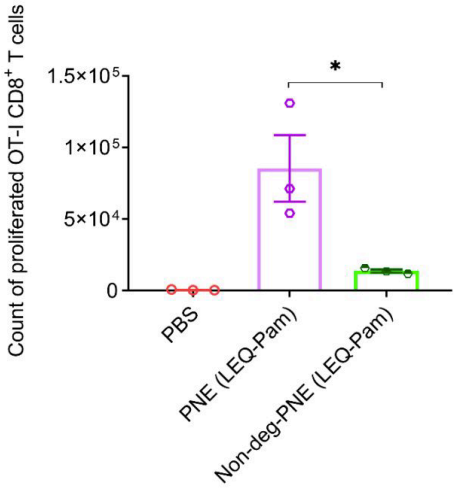

Figure 2.17. In *vitro* cross-priming of OT-I $CD8^+$ T cells by BMDCs pulsed with PNE(LEQ-Pam) and non-deg. PNE(LEQ-Pam).

CFSE-labeled naïve OT-I $CD8^+$ T cells were co-cultured with BMDCs pulsed with PNE(LEQ-Pam) or non-deg. PNE(LEQ-Pam). Proliferated OT-I $CD8^+$ T cells were counted by flow cytometry analysis. *P < 0.05.

To further understand the mechanism by which PNE could promote the cross-presentation of SLPs, we tracked the intracellular trafficking of SLPs delivered by PNE(LEQ-Pam) by labeling the antigen peptides with Alexa Fluor™ 647 and monitoring the antigen localization in BMDCs using confocal microscopy (Figure 2.15D). Upon 24-hour co-incubation of BMDCs

and PNE(LEQ-Pam), significant amounts of antigens (red) were found dis-localized with endolysosomes stained with LysoTracker (green), and the signal in the cytosol was sustained up to 48 hours. By contrast, in BMDCs incubated with the mixture of free LEQ and Pam, a majority of the antigens stayed co-localized with endolysosomes, and the fluorescent signal of total intracellular antigens decreased rapidly after 24-hour incubation. Therefore, the responsive PNE facilitated the endosomal escape of the peptide antigens leading to subsequent MHC class I molecule loading and cross-presentation. Endosomal escape of SLPs was likely through the pH-buffering effect of the released cationic peptides and/or the endosomal membrane fusion with the lipopeptides (Pam).[79,80]

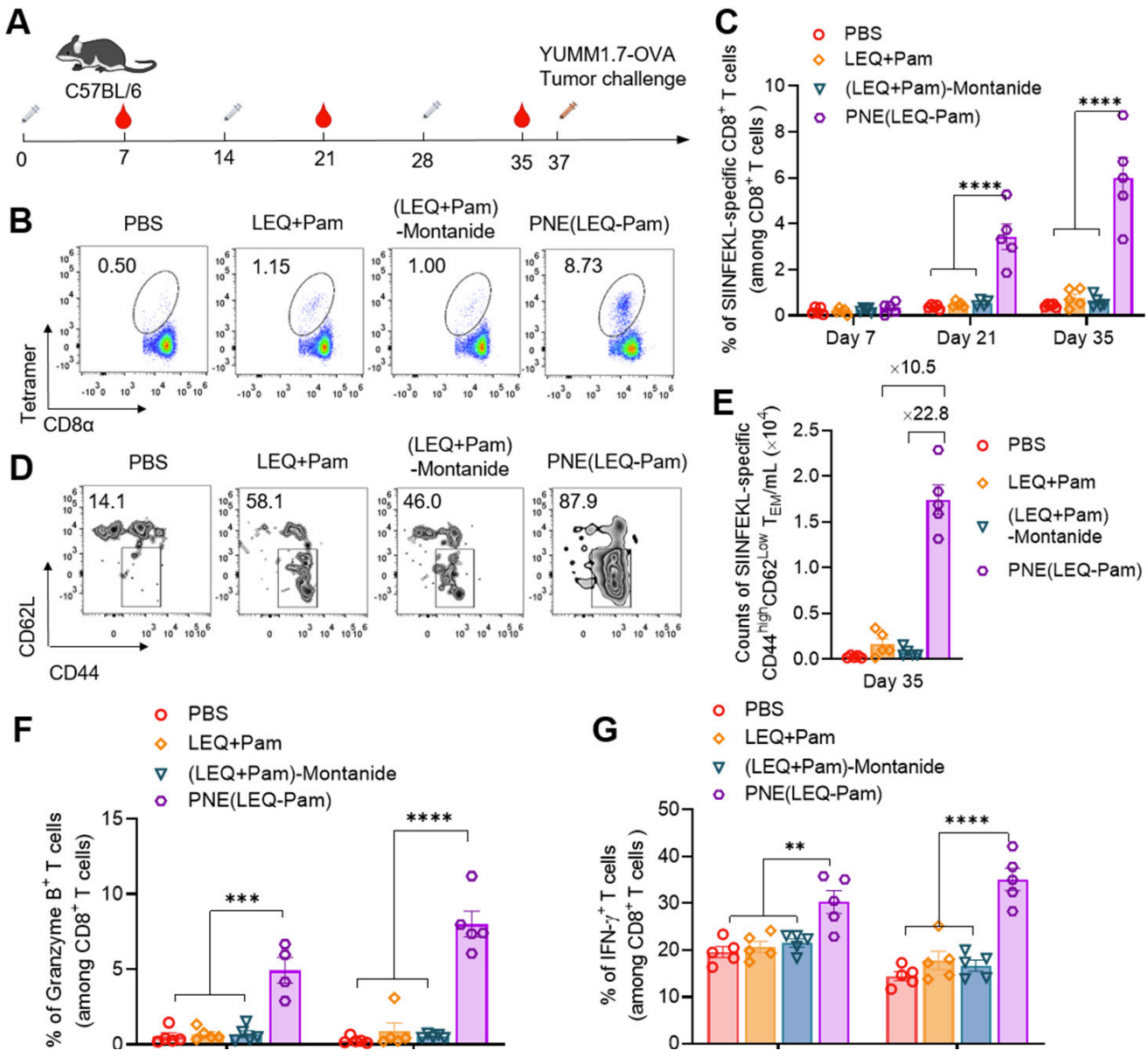

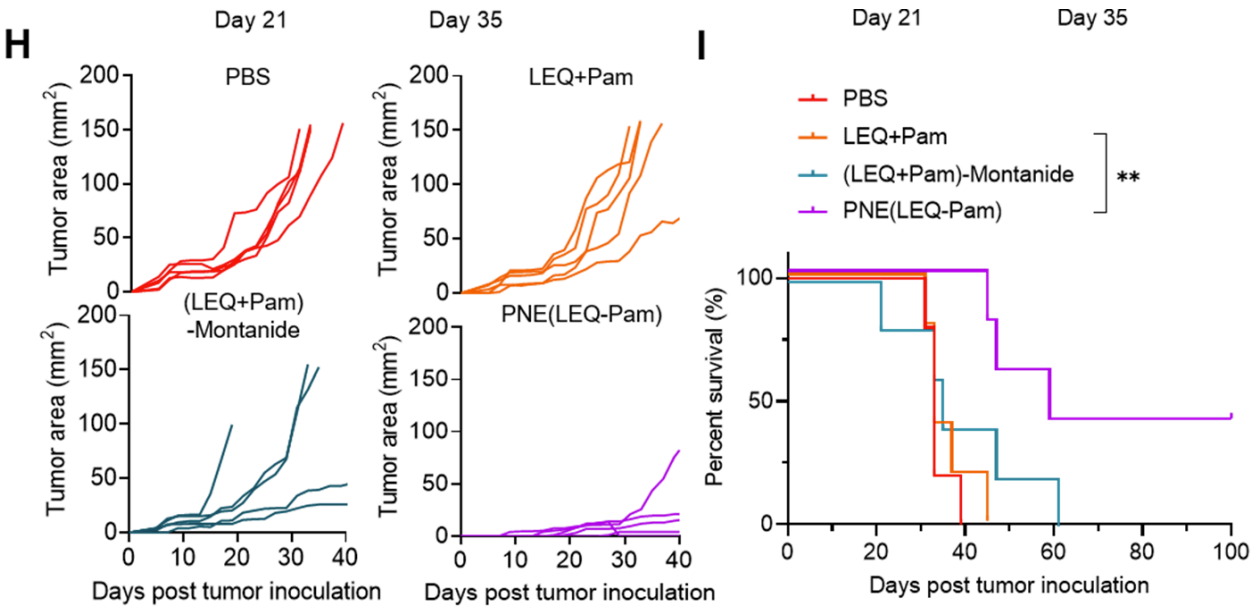

Figure 2.18. PNE(LEQ-Pam) vaccine-elicited potent antigen-specific $CD8^+$ T cell response.

A) C57BL/6 mice were vaccinated with PBS, LEQ+Pam, (LEQ+Pam) - Montanide, or PNE(LEQ-Pam) on day 0, 14, and 28. The peripheral blood was collected 7 days post each vaccination. Mice were subcutaneously challenged with YUMM1.7-OVA cells (5×10^5) on day 37. (n = 5 independent animals each group); B) Representative flow cytometry plots showing the frequencies of SIINFEKL-specific $CD8a^+$ T cells from the PBMCs on day 35; C) The average frequencies of SIINFEKL-specific $CD8^+$ T cells in peripheral blood on day 7, 21, and 35; D) Representative flow cytometry plots showing the frequencies of $CD44^{high}CD62L^{low}$ TEM cells among SIINFEKL-specific $CD8^+$ T cells; E) Counts of SIINFEKL-specific $CD8^+$ TEM cells on day 35; F, G) The frequency of Granzyme B+ (F) and IFN-γ+ T cells (G) in $CD8^+$ T cells in the peripheral blood were measured 7 days post the second and third vaccination by intracellular staining. The data show Mean ± SEM from a representative experiment (n = 5); H) The tumor growth curves of each group in the prophylactic experiment; I) Survival rate of mice in each group. The statistical analysis between groups were performed by one-way ANOVA for flow cytometry data and Log-rank test for survival curves; * $P < 0.05$; ** $P < 0.01$; *** $P < 0.001$; **** $P < 0.0001$.

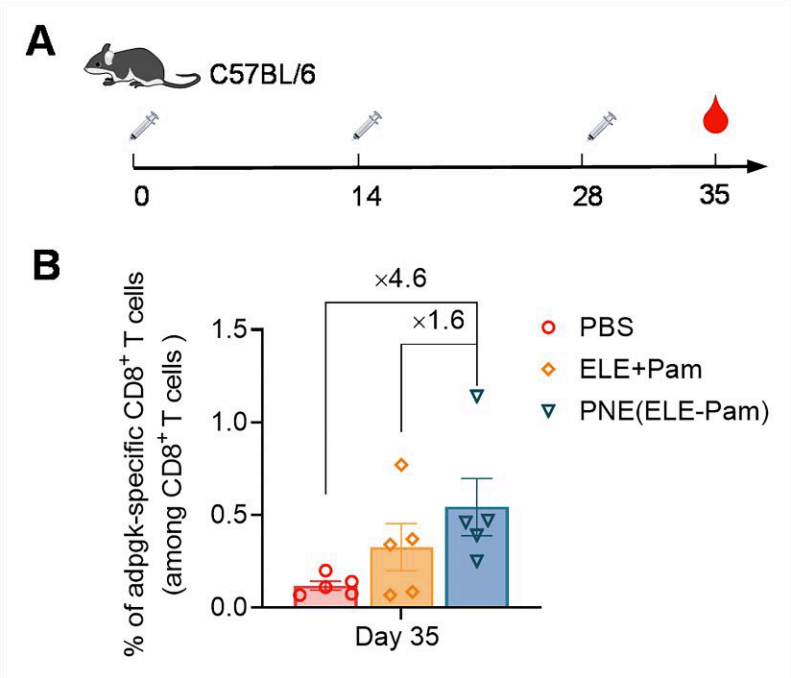

Figure 2.19. PNE(ELE-Pam) elicited potent antigen-specific $CD8^+$ T cell response against adpgk.

A) C57BL/6 mice were vaccinated with PBS, ELE+Pam, (ELE+Pam)-Montanide, or PNE(ELE-Pam) on day 0, 14, and 28. The peripheral blood was collected 7 days post the last vaccination; B) The average frequencies of adpgk-specific $CD8^+$ T cells in peripheral blood on day 35.

2.4 T cell immune response

Encouraged by the results showing enhanced LN targeting and cross-presentation of PNE, we next determined the T cell immune response and anti-tumor activity induced by PNE vaccination in *vivo*. C57BL/6 mice were immunized subcutaneously with one prime (day 0) and 2 boosts (day 14, 28) vaccinations of PNE(LEQ-Pam) (containing 15-nmol LEQ and 5-nmol Pam), or the mixture of equivalent doses of LEQ and Pam in the form of solution or emulsion in Montanide (Figure 2.18A). Peripheral blood mononuclear cells (PBMCs) were collected one week post each immunization and stained with SIINFEKL tetramer to examine the frequency of SIINFEKL-MHC-I tetramer$^+$$CD8^+$ T cells. The simple mixture of LEQ and Pam induced minimum T cell immune response with a mean frequency of SIINFEKL specific $CD8^+$ T cells close to the background (0.77% SIINFEKL-specific T cells among $CD8^+$ T cells vs. 0.44% in non-immunized mice) post the second boost; the mixture emulsified in Montanide showed only modest improvement (0.60% SIINFEKL-specific T cells among $CD8^+$ T cells on day 35, Figure 2.18B, C). In contrast, PNE(LEQ-Pam) vaccine elicited a high frequency (6.00%)

of SIINFEKL-specific $CD8^+$ T cells that was 7.8- and 10-fold higher compared to the mixture of LEQ and Pam in solution and Montanide, respectively (day 35, Figure 2.18B, C). The majority (87.9%) of the elicited antigen-specific $CD8^+$ T cells by PNE(LEQ-Pam) exhibited effector memory phenotype ($CD44^{high}CD62L^{low}$) (Figure 2.18D). Notably, PNE vaccines remarkably expanded the antigen-specific TEM cells to a number 10.5- and 22.8- fold greater than that of the mixture of LEQ and Pam in solution and Montanide, respectively (day 35, Figure 2.18E). Importantly, mice immunized with PNEs also showed markedly increased frequency of Granzyme B-secreting $CD8^+$ T cells, which was 9.0- and 14.8-fold higher than that in mice immunized with the mixture of LEQ and Pam in solution and Montanide, respectively (Figure 2.18F), suggesting that PNE vaccination also enhanced the cytotoxicity of $CD8^+$ T cells. Furthermore, more than 35.1% of the $CD8^+$ T cells in PBMCs produced effector cytokines, such as interferon-γ-secreting (IFN-γ^+) (Figure 2.18G), indicating the increased effector functions.

As PNE(LEQ-Pam) displayed superior antigen (SII) specific $CD8^+$ T cell immune response and significantly higher effector memory T cell exhibition, effector cytokines secretion like Granzyme B and IFN-γ. We next investigated to know if the same effect will be elicited on neoantigen-based PNE. C57BL/6 mice were immunized subcutaneously with one prime (day 0) and 2 boosts (day 14, 28) vaccinations of PNE(ELE-Pam) (containing 15-nmol ELE and 5-nmol Pam), or the mixture of equivalent doses of ELE and Pam in the form of solution (Figure 2.19A). Peripheral blood mononuclear cells (PBMCs) were collected one week post the second boost immunization and stained with adpgk-tetramer to examine the frequency of adpgk-MHC-I tetramer$^+$$CD8^+$ T cells. PNE(ELE-Pam) vaccine-elicited 1.6- and 4.6-fold higher frequency of adpgk-specific $CD8^+$ T cells immune response compared to a mixture of equivalent doses of ELE and Pam in the form of solution and background, respectively (day 35, Figure 2.19B), suggesting that PNE vaccine platform is also versatile effective in *vivo*.

The markedly enhanced vaccination efficiency by PNE motivated us to evaluate its antitumor efficacy. The immunized mice were challenged subcutaneously with YUMM1.7-OVA cells (5×10^5), a murine melanoma cell line expressing OVA antigens. Mice immunized with PNE(LEQ-Pam) vaccine showed significantly delayed tumor growth (Figure 2.18H) and prolonged survival (Figure 2.18I). Notably, 2 out of 5 mice exhibited durable cures for at least 100 days post tumor inoculation. These two survivors maintained 1.90% and 1.35% antigen-specific $CD8^+$ T cells in the PBMCs, which were mostly central memory cells (Figure 2.20), providing durable protection. In addition, in a more challenging therapeutic setting, C57BL/6

mice were first inoculated with YUMM1.7-OVA tumor cells (5×10^5 cells), followed by multiple vaccinations with PNE or the mixture of equivalent doses of LEQ and Pam in the form of solution or emulsion in Montanide (Figure 2.21A). It is notable that mice treated with PNE vaccines still exhibited significantly enhanced capacity in inhibiting tumor growth and extending the survival of treated mice compared to the vaccine of mixed antigen and adjuvant in Montanide (Figure 2.21B, C).

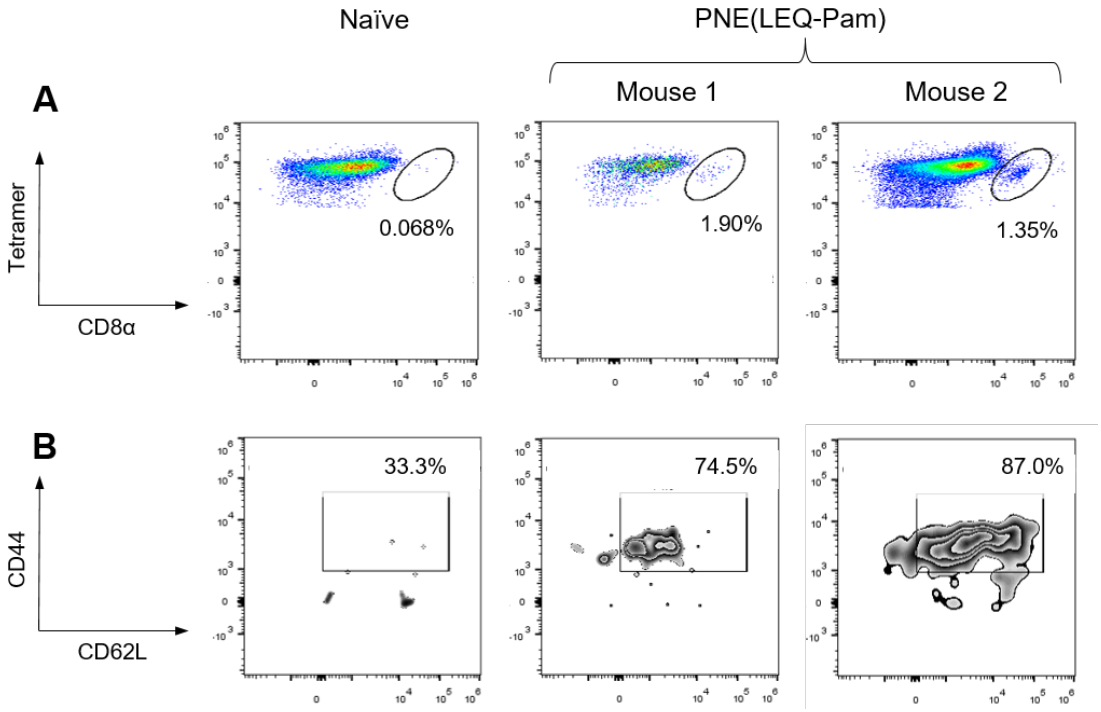

Figure 2.20. Flow cytometry plots show the frequencies of SIINFEKL-specific $CD8a^+$ T cells.

A) and their memory phenotype B) in PBMC from survival mice immunized by PNE(LEQ-Pam) vaccines (Mouse 1 and Mouse 2) or a naïve mice control. The PBMC was collected 90 days post tumor inoculation.

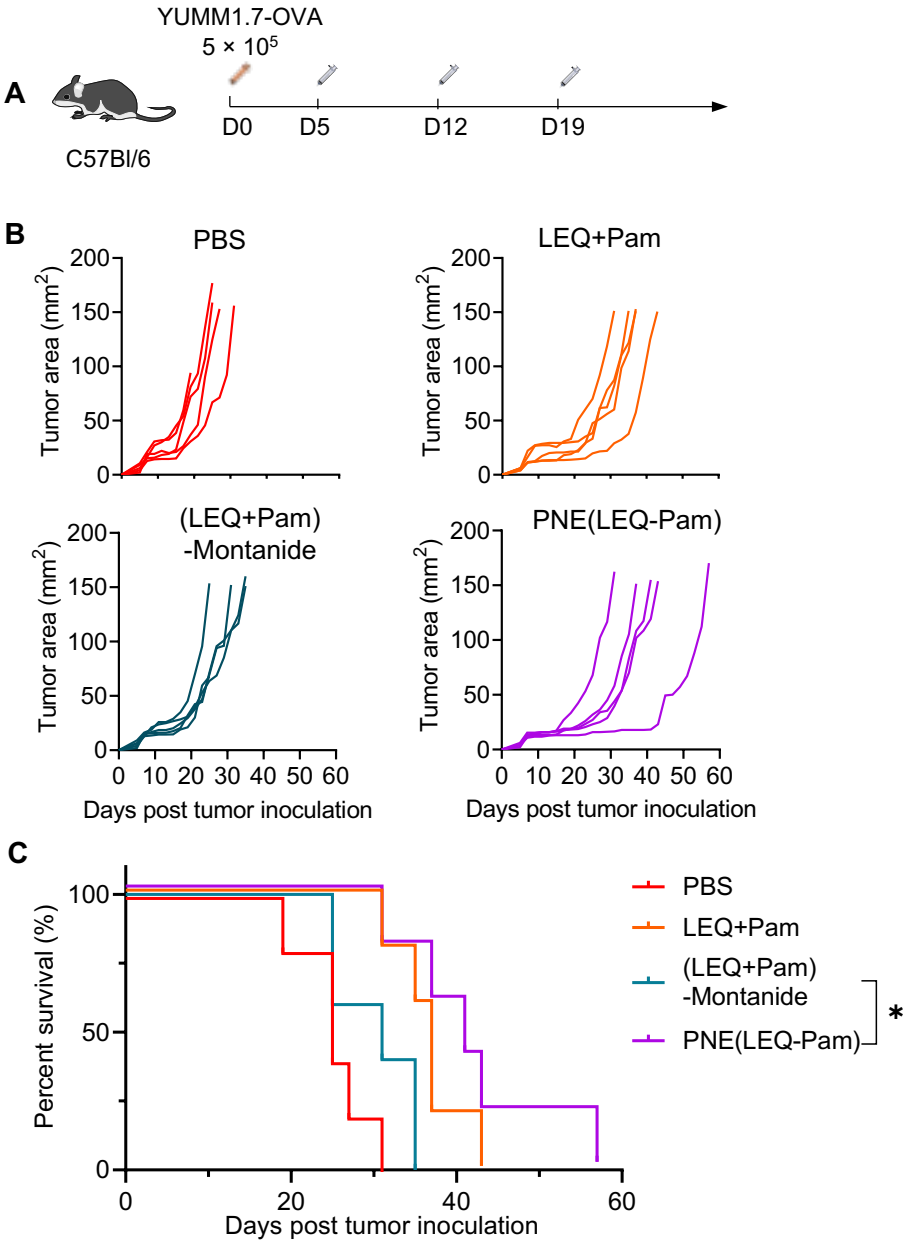

Figure 2.21. Anti-tumor efficacy of PNE(LEQ-Pam) vaccine in a therapeutic setting.

A) C57BL/6 mice were inoculated with YUMM1.7-OVA tumor cells (5×10^5) at the right flank and treated with indicated vaccine formulations on day 5, 12, 19. (n = 5 animals); B) Individual tumor growth curves of each treatment group; C) Survival rate of mice in each group. The data show Mean ± SEM. The statistical analysis between survival curves was performed by Log-rank test; * $p < 0.05$; ** $p < 0.01$; *** $p < 0.001$; **** $p < 0.0001$.

2.5 Conclusion

In summary, we have demonstrated a responsive PNE as a facile, effective, and versatile vaccine platform for the delivery of peptide neoantigens to enhance personalized cancer immunotherapy. PNE is a highly modular system permitting the co-polymerization of peptide antigens, and molecular adjuvants of diverse structures and properties, which is a highly desired property as individually identified neoantigens from patients could vastly differ in physiochemical properties. We envision that this new strategy can be readily extended to the co-delivery of multiple heterogeneous epitopes in the form of SLPs, proteins (e.g., whole tumor cell lysate), or replicon mRNAs/DNAs encoding the neoepitopes. Implementation of various responsive chemistry in the linker-monomer (monomer B) could potentially impart different responsiveness to the PNEs facilitating triggered release of antigens and/or adjuvants by intracellular stimuli including pH change, reactive oxygen species, protease, etc.

Direct assembly of peptide or protein antigens relied on non-covalent assembly[81–85] or disulfide crosslinking[86,87] without carriers is actively being pursued as reported in some elegant studies recently. Such “carrier-free” approaches, including ours, have the unique advantage of minimizing the potential risk of using additional carrier materials whose own immunogenicity and safety profile has to be determined before clinical applications.[63,64,88–90] The PNE approach described here based on a highly efficient covalent conjugation of amines in DMSO or aqueous solution doesn’t require the use of any denaturing conditions such as heating, and therefore showed high promise for the delivery of a wide range of individualized neoepitopes with good compatibility.

2.6 Materials, Instruments, and Methods

Materials

All the synthetic long peptides (SLPs) were purchased from GenScript (Piscataway, New Jersey, USA). $Pam_3CysSer$-$(Lys)_4$ (Pam) was purchased from InvivoGen (San Diego, California, USA). Bis-amine-CpG (5'-/5AmMC6/TCCATGACGTTCCTGACGTT/3AmMO/-3', amine-functionalization at 5'- and 3'-positions) was purchased from Integrated DNA Technologies (Coralville, Iowa, USA). Montanide™ ISA 51 VG was a gift from SEPPIC (Paris, France). Murine granulocyte-macrophage colony-stimulating factor (GM-CSF) was purchased from PeproTech (London, UK). NovexTM 10% - 20% tricine gel and Tricine SDS sample buffer (2X) were purchased from Invitrogen (California, United States). Lipopolysaccharide (LPS), anhydrous dimethylsulfoxide (DMSO), triethylamine (TEA), fluoresceinamine, and other chemicals were purchased from Sigma-Aldrich (St. Louis, Missouri, USA). Unless otherwise noted, all chemical and biological reagents were used as received.

Pierce™ quantitative fluorometric peptide assay, ProLong™ diamond antifade mountant, Alexa Fluor™ 647 N-hydroxysuccinimide (NHS) ester, Alexa Fluor™ 488 N-hydroxysuccinimide (NHS) ester, LysoTracker™ Red DND-99, Hoechst 33342, CellTrace™ carboxyfluorescein succinimidyl ester (CFSE) cell proliferation kit and Zombie Aqua™ Fixable Viability Kit were purchased from BioLegend (San Diego, California, USA). eBioscience™ Cell Stimulation Cocktail (plus protein transport inhibitors) was purchased from Invitrogen (Carlsbad, California, USA). Cytofix/Cytoperm™ fixation/permeabilization kit was purchased from BD Bioscience (San Jose, CA, USA). Mouse $CD8^+$ T cell isolation kit was purchased from Miltenyi Biotec (Bergisch Gladbach, Germany).

Antibodies for fluorescence-activated cell sorting (FACS) including anti-CD16/32 (Clone: 93), anti-CD3 (Clone: 17A2), anti-CD8α (Clone: 53-6.7), anti-CD11c (Clone: N418), anti-CD40 (Clone: 3/23), anti-CD44 (Clone: IM7), anti-CD62L (Clone: MEL-14), anti-CD80 (Clone: 16-10A1), anti-CD86 (Clone: GL-1), anti-Granzyme B (anti-GrzmB, Clone: GB11), anti-IFN-γ (Clone: XMG1.2), and anti-TNF-α (Clone: MP6-XT22) were purchased from BioLegend (San Diego, California, USA). iTAg Tetramer/PE-H-2 Kb OVA (SIINFEKL) was purchased from MBL (Woburn, Massachusetts, USA).

Instruments

Nuclear magnetic resonance (NMR) spectra were acquired on Bruker AVANCE NEO 400 MHz spectrometers (Billerica, Massachusetts, USA). Electrospray ionization mass spectra (ES-IMS) were acquired on an LTQ Orbitrap ELITE ETD (Thermo Fisher Scientific). Matrix-assisted laser desorption/ionization time-of-flight mass spectra (MALDI-TOF-MS) were acquired on an Autoflex Speed (Bruker, Billerica, Massachusetts, USA). Polycondensate neoepitope (PNE) was characterized by PL-gel permeation chromatography (GPC) 50+ Integrated GPC/SEC System (Agilent, Santa Clara, California, USA) and UltiMateTM 3000 ultra-high-performance liquid chromatography (UHPLC) system (Thermo Fisher Scientific) equipped with a Hypersil Gold^{TM} C18 selectivity LC column or a BioBasic™ SEC 300 LC column, and detectors of diode array detector (UV, DIONEX UltiMateTM 3000) and charged aerosol detector (CAD, DIONEX Corona ultra-RS). The fluorescent image of sodium dodecyl sulfate-polyacrylamide gel electrophoresis (SDS-PAGE) was taken by Bio-Rad ChemiDoc MP imaging system (Hercules, California, USA). The size of the particle was measured by dynamic light scattering (DLS) on Malvern NanoZS (Worcester, UK). The transmission electron microscopy (TEM) images of PNEs were acquired on the FEI Tecnai Osiris TEM instrument (FEI, Oregon, USA). The atomic force microscopy (AFM) images of free LEQ and Pam were acquired on a Park NX-10 analytical system (Suwon, South Korea) with non-contact amplitude modulation (PPPNCHR, Park system) in ambient conditions. The fluorescence intensity of samples was measured with a Varioskan® Lux microplate reader (Thermo Fisher Scientific). All the flow cytometry data were acquired using an Attune NxT flow cytometer (Thermo Fisher Scientific). Confocal fluorescent microscope images were acquired with an LSM 700 with 40X or 63X oil objectives (Zeiss, Oberkochen, Germany). Mouse tissue imaging was conducted with an in *vivo* imaging system (IVIS, PerkinElmer, Waltham, Massachusetts, USA).

Mice and cells

Experimental procedures in mouse studies were approved by the Swiss authorities (Canton of Vaud, animal protocol ID 3206) and performed in accordance with École Polytechnique Fédérale de Lausanne (EPFL) CPG guidelines. Six- to eight-week-old female Thy1.2^{+} C57BL/6

mice, TCR-transgenic OT-I mice (B6-Tg (TcraTcrb)1100Mjb/J) were purchased from The Jackson Laboratory (Bar Harbor, Maine, USA) or Charles River Laboratories (Lyon, France) and maintained in the animal facility. Ovalbumin (OVA)-expressing YUMM1.7 (YUMM1.7-OVA), a murine melanoma cell line, was a generous gift from Prof. Ping-Chih Ho (University of Lausanne, Lausanne, Switzerland) and cultured in DMEM complete medium supplemented by fetal bovine serum (FBS, 10%), Penicillin (100 UML^{-1}), Streptomycin (100 μgmL^{-1}). Immature bone marrow-derived dendritic cells (BMDCs) were isolated from C57BL/6 mice (Charles River Laboratory, Wilmington, Massachusetts, USA) and cultured in RPMI 1640 complete medium containing HI-FBS (10%), L-glutamine (2 mM), Penicillin (100 UmL^{-1}), Streptomycin (100 µgmL-1), and 2-mercaptoethanol (β-ME, 50 µM) with GM-CSF (20 $ngmL^{-1}$) for 6 days at 37 ºC with CO_2 (5%) before use. Naïve OT-I $CD8^+$ T cells were isolated from splenocytes of OT-I mice with a mouse $CD8^+$ T cell isolation kit.

Method

Synthesis of bi-functional Monomer B_{red} (Mon_{red})

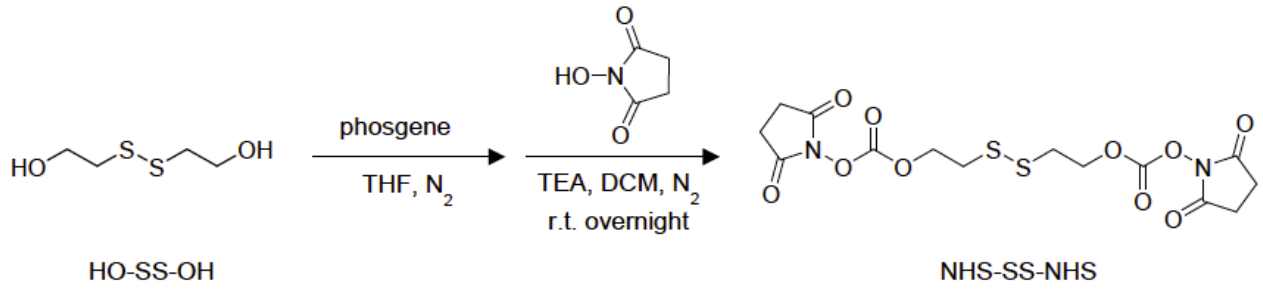

Figure 2.5. Synthesis of bi-functional Mon_{red}.

The synthesis of **Mon_{red}** was reported previously with minor modification.1 2-Hydroxyethyl disulfide (1.329 g, 8.616 mmol) was dissolved in anhydrous tetrahydrofuran (THF, 20 mL) in a 100-mL round-bottom flask, followed by the addition of phosgene solution (12.5 mL, 15% w/w, 18.95 mmol) in anhydrous THF (10 mL). The reaction mixture was stirred under room temperature (rt) for 2 hours under the protection of N_2 and then concentrated under vacuum. The remaining residue was dissolved again with anhydrous dichloromethane (DCM, 10 mL)

and mixed with N-hydroxysuccinimide (NHS, 2.182 g, 18.95 mmol) and anhydrous triethylamine (TEA, 1.918 g, 18.95 mmol) in DCM solution (45 mL). The reaction was stirred at rt overnight under the protection of N_2. The solvent was removed by a rotary evaporator. The crude product was purified with silica chromatography (DCM: Methanol=10:1) and recrystallized with icy petroleum. The acicular crystal (2.14 g, yield: 57%) was dried under vacuum and characterized by ^{1}H NMR and ESI-MS (Figure 2.6). (1H NMR (400 MHz, chloroform-d, 25 ºC, TMS): δ=4.61 (t, 3J (H, H) =4 Hz, 4H, CH2), 3.08 (t, 3J (H, H) =4 Hz, 4H, CH2), 2.88 (s, 8H, CH2). ESI (m/z): $[M+Na]^+$=459.0).

Preparation of polycondensate neoepitopes (PNEs)

Depending on the solubility of peptides and adjuvants, synthesis of PNEs can be done in anhydrous DMSO or aqueous solution. The detailed information of composition and conditions for the syntheses of each PNE has been summarized in Table 2-2.

PNE of SLP only [PNE(LEQ)]: $LEQLESIINFEKLK_5$ (LEQ, 50 μg, 16.6 nmol) in anhydrous DMSO (17.24 μL) was mixed with Mon_{red} (40 $mgmL^{-1}$ in anhydrous DMSO, 0.76 μL, 69.7 nmol). The mixture was shaken in an Eppendorf ThermoMixer at 25 °C for 30 min at 800 rpm followed by the addition of TEA (2 μL) and another 60-min incubation at 25 °C, 800 rpm. The resultant product was lyophilized overnight to remove DMSO and TEA and characterized with DLS, HPLC, and TEM.

PNE of SLP with adjuvant [PNE(LEQ-Pam)]: In an anhydrous DMSO solution (17.24 μL) of LEQ (50 μg, 16.6 nmol) and Pam_3CSK_4 (4.18 μg, 5.5 nmol), Mon_{red} (40 $mgmL^{-1}$ in anhydrous DMSO, 0.76 μL, 69.7 nmol) was added. The mixture was shaken at 25 °C for 30 min at 800 rpm by the addition of TEA (2 μL) and another 60-min incubation at 25 °C, 800 rpm. The resultant product was purified following the same procedure as described above and characterized with DLS, GPC, HPLC, TEM, and SDS-PAGE.

Preparation of non-degradable PNE (non-deg. PNE): Non-degradable PNE(LEQ-Pam) was prepared similarly as described above by replacing Mon_{red} with a non-degradable monomer B, bis(sulfosuccinimidyl)suberate (Mon_{BS3}, 112.75 nmol). The other procedures were the same as PNE(LEQ-Pam).

Synthesis of PNEs could be performed in an aqueous solution with a similar procedure. In a typical synthesis of PNE, the same amount of SLP and adjuvant were dissolved in phosphate-buffered saline (PBS, adjusted to pH = 8.5 with Na_2CO_3) and mixed with Mon_{red} (40 $mgmL^{-1}$ in anhydrous DMSO). The mixture was shaken at 25 °C, 600 rpm, for 30 min. The resultant product was purified by PBS (pH 7.4, 200 μL × 3) with Amicon® centrifugal filters (Merck Millipore, Burlington, Massachusetts, USA) with molecular weight cut-off (MWCO) of 3 kDa, to get rid of unreacted peptides or Mon_{red}.

Characterizations of PNEs

NMR: Free LEQ (200 μg) and PNE(LEQ) (200 μg) were ultrafiltered with D_2O (200 μL × 3) using Amicon® centrifugal filters (MWCO 3 kDa, 10000 rpm) to get rid of H_2O, DMSO, salts, and other possible impurities. The trace of water and protons from acid phosphate was further removed by repeating lyophilizing and dissolving with D_2O. The purified free LEQ and PNE(LEQ) were re-dissolved in D_2O (400 μL) respectively and measured by ^1H NMR spectrometer.

UHPLC: PNE(LEQ) and PNE(LEQ-Pam) were lyophilized to get rid of DMSO and TEA. LEQ, Pam, and PNE each were diluted in ultrapure water with a concentration of 0.5 $mgmL^{-1}$. For LEQ, a mobile phase gradient (A=acetonitrile, B=H_2O+0.1% trifluoroacetic acid (TFA), B at 90% for 0-1 min, 90-10% for 1-18 min, 10-90% for 18-19 min, and 90% for 19-20 min at flow rate of 0.4 $mLmin^{-1}$) was used on a Hypersil GoldTM C18 selectivity LC column at 40 ºC. For the detection of Pam, a mobile phase gradient (B at 5% for 0-2 min, 5-95% for 2-18 min, 95-5% for 18-19 min, and 5% for 19-20 min at a flow rate of 0.4 $mLmin^{-1}$) was used on the same C18 column. The loading efficiency of LEQ and Pam in PNE(LEQ-Pam) was calculated from the integral area of CAD curves. To verify the increased MW of PNE(LEQ) and PNE(LEQ-Pam) compared with free PNE, the lyophilized PNE(LEQ) and PNE(LEQ-Pam) were dissolved in PBS (pH = 7.4), a mobile phase of NaCl solution (200 mM, pH 7.4 at flow rate of 0.5 $mLmin^{-1}$) was used on BioBasic™ SEC 300 LC column.

GPC: LEQ and PNE(LEQ-Pam) in PBS (0.1 $mgmL^{-1}$, pH 7.4) were injected into GPC (100 μL each sample injection) and analyzed with a mobile phase of NaCl (100 mM) and TFA (1%) and flow rate of 1.0 $mLmin^{-1}$.

DLS: PNEs were diluted with PBS (0.05 $mgmL^{-1}$, pH 7.4) in Fisherbrand™ PS semi-micro cuvettes at rt for DLS measurement with Marven NanoZS. Data represented 3 independent samples for each PNE sample.

TEM: Freshly prepared PNEs were lyophilized overnight to get rid of DMSO and TEA. The dry powder was then redissolved with ultrapure water (0.5 $mgmL^{-1}$, calculated by the stoichiometry of LEQ) and loaded onto a copper grid. After washing with ultrapure water, the sample-loaded copper grid was negatively stained with uranyl acetate (1% w/v in ultrapure water). The TEM image was taken by the FEI Tecnail Osiris TEM instrument (200 kV) equipped with a 4k × 2.6k Gatan Orius CCD camera.

SDS-PAGE: Freshly prepared PNEs in PBS (0.5 $mgmL^{-1}$, 7.5 μL, pH = 7.4) were mixed fluoresceinamine in acetone (1 mM, 7.5 μL), and then mixed with Novex™ Tricine SDS sample buffer (2X). The samples were then loaded onto Novex™ 10-20% Tris-Glycine Gels and run in MES buffer at 110V for 60 min. The image of the gel was taken by a Bio-Rad microwell plate reader equipped with a gel imager (ex: 590 nm, em: 700 nm).

Release kinetics and characterization of LEQ from PNE(LEQ-Pam)

Freshly prepared PNE(LEQ-Pam) (50 μg) diluted in PBS (0.1 $mgmL^{-1}$, 490 μL, pH 7.4), was added with DL-dithiothreitol (DTT) (10 μL, 100 mM in PBS, pH 7.4). The mixture was aliquot and incubated at rt or 37 ºC. At set time points (0, 2, 4, 8, 12, and 24 hours), the aliquot (10 μL) was collected and analyzed by Pierce™ quantitative fluorometric peptide assay according to the kit protocol. The mixture was kept in the dark for 10 min, and the fluorescent intensity was quantified with a microplate reader (Ex 390 nm, Em 475 nm). The released LEQ was also characterized with MALDI-TOF-MS to measure the molecular weight (MW) and compare it with the original LEQ.

Fluorescent labeling of LEQ, Pam, and PNE(LEQ-Pam)

Solutions of LEQ, Pam, or the mixture of two were added with Alexa Fluor™ 647 NHS ester (10 $mgmL^{-1}$ in anhydrous DMSO) with equal stoichiometry and then shaken with an Eppendorf ThermoMixer at 25 °C (600 rpm, 10 min). The “labeled” mixture was used for the next step

without purification. Additional LEQ, Pam, or both (unlabeled) were then added to the labeled mixture, followed by similar procedures for preparation and purification of PNEs as described above. For in *vitro* studies, 10% of LEQ or Pam was fluorescently labeled; for in *vivo* studies, 50% was labeled.

In *vivo* lymph node targeting and dendritic cell internalization

Fluorescently labeled LEQ, Pam, or PNE(LEQ-Pam) in PBS solution (50 μL, pH 7.4) containing equivalent LEQ (4.51 nmol) and/or Pam (1.12 nmol) were subcutaneously injected into the tail base (25 μL for each side, both sides) of C57BL/6 mice (female, 7 weeks old, n=3 per group). PBS (50 μL, pH 7.4) was used as a negative control. The mixture of equivalent LEQ and Pam (25 μL) was pipetted vigorously with Montanide ISA 51 VG (25 μL) to generate a stable emulsion for injection. The mice were sacrificed 24 hours later, and inguinal lymph nodes (LNs) were harvested and imaged with IVIS to measure the total fluorescent intensity in LNs (Ex 640 nm, Em 680 nm, exposure time 0.5 s).

The LNs were then ground through a 70-μm cell strainer, and the collected cells were washed with FACS buffer (0.2% BSA in PBS, 200 μL × 2). The cells were blocked with anti-CD16/32 at 4 ºC for 15 min, and then stained with anti-CD11c (PE/Dazzle^{TM} 594) at 4 ºC for another 20 min followed by washing with FACS buffer (200 μL × 3). The stained cells were resuspended in a 4,6-diamidino-2-phenylindole (DAPI) solution (0.1 μgmL^{-1}, 200 μL) and analyzed with flow cytometry.

In *vitro* BMDC internalization

Immature BMDCs were prepared as described above. On Day 6, the BMDCs were plated in 24-well plates (5×10^5 cells per well) with RPMI 1640 medium (1 mL, FBS free, penicillin/streptomycin free) and incubated with fluorescently labeled PNE(LEQ-Pam) or other control formulations containing equivalent LEQ (2.25 nmol) and/or Pam (0.56 nmol) at 37 ºC with CO_2 (5%). After 6-hour incubation, BMDCs were harvested, washed with FACS buffer (200 μL × 2), and incubated with anti-CD16/32 at 4 ºC for 15 min. The BMDCs were then stained

with PE/Dazzle 594-anti-CD11c at 4 ºC for 20 min, washed with FACS buffer (200 μL × 2), and resuspended in a DAPI solution (0.1 μgmL^{-1}, 200 μL) for flow cytometry analyses.

In *vitro* BMDC activation

Immature BMDCs were prepared as described above. On Day 6, immature BMDCs were plated in 24-well plates (5×10^5 cells per well) with RPMI 1640 complete medium (1 mL) supplemented with GM-CSF (20 $ngmL^{-1}$) and incubated with PNE(LEQ-Pam) or other control formulations containing equivalent LEQ (2.25 nmol) and/or Pam (0.56 nmol) at 37 ºC with CO_2 (5%). After 48-hour incubation, BMDCs were harvested, washed with FACS buffer (200 μL × 2), and incubated with anti-CD16/32 at 4 ºC for 15 min. The cells were then stained with a mixture of antibodies of PE-anti-CD11c, PE-Cy7-anti-CD80, BV510-anti-CD86, PerCPCy5.5-anti-CD40 at 4 ºC for 20 min. The cells were then washed with FACS buffer (200 μL × 2) and resuspended in a DAPI solution (0.1 μgmL^{-1}, 200 μL) for flow cytometry analyses.

In *vitro* cross-priming of OT-I $CD8^+$ T cells

Immature BMDCs were prepared as described above. On Day 6, immature BMDCs were plated in 24-well plates (5×10^5 cells per well) with RPMI 1640 complete medium (1 mL) supplemented with GM-CSF (20 $ngmL^{-1}$). PNE(LEQ-Pam) and other control formulations containing equivalent LEQ (2.25 nmol) and/or Pam (0.56 nmol) were then added to pulse the BMDCs. SIINFEKL (SIIN, 2.25 nmol) with or without Pam (0.56 nmol) were also added as control samples. The BMDCs were cultured at 37 ºC with CO_2 (5%) for 24 hours. The pulsed BMDCs (2×10^4) were first washed with PBS (200 μL × 3) and then co-cultured with naïve OT-I $CD8^+$ T cells (1×10^5) labeled with CFSE (1 μM for 10 million cells in PBS, 5 min, 37 ºC) in complete RPMI 1640 medium (200 μL) at 37 ºC with CO_2 (5%). The RPMI complete medium was supplemented with FBS (10%), L-glutamine (2 mM), Penicillin (100 UmL^{-1}), Streptomycin (100 μgmL^{-1}), β-ME (50 μM), sodium pyruvate (1 mM), and HEPES (0.02 M). After a 72-hour co-incubation, the cells were harvested, washed with FACS buffer (200 μL × 2), and incubated with anti-CD16/32 at 4 ºC for 15 min. The cells were then stained with PE/Dazzle 594-anti-CD8α at 4 ºC for 20 min, washed with FACS buffer (200 μL × 2), and processed similarly for flow cytometry analyses.

Confocal fluorescent microscope imaging

PNE(LEQ-Pam) or the simple mixture containing equivalent LEQ (4.51 nmol) and Pam (1.12 nmol) in PBS solution (5 μL, pH 7.4) were incubated with immature BMDCs (1×10^6) in complete RPMI 1640 culture medium (1 mL) supplemented with GM-CSF (20 $ngmL^{-1}$). At set time points (6, 24, and 48 hours), the BMDCs were washed with PBS (1 mL × 2) and then stained with LysoTracker™ Red DND-99 (125 nM) for endolysosome staining and Hoechst 33342 (4 μM) for nuclei staining in phenol/serum-free RPMI 1640 medium at 37 ºC with CO_2 (5%) for 1.5 hours followed by PBS washing (1 mL × 2). BMDCs were then fixed with 4% paraformaldehyde (PFA, 100 μL) for 10 min, washed with PBS (1 mL × 2), and resuspended in ProLong™ diamond antifade mountant (10 μL). After centrifuging onto a poly-lysine coated glass slide, the BMDCs were imaged with an LSM 700 confocal microscope with a 40X or 63X oil objective.

In *vivo* immunization study

C57BL/6 mice (female, 7-week-old) were immunized subcutaneously at the tail base with LEQ (15 nmol) and Pam (5 nmol) in a PBS solution (50 μL) in the form of a simple mixture, an emulsion form lation in Montainide, or PNE(LEQ-Pam) following an experimental timeline that mice were primed on day 0 and boosted on day 14 and 28.

Tetramer staining: On day 7, 21, and 35, peripheral blood (50 μL) was collected from the tail veins of immunized mice to assess the antigen-specific $CD8^+$ T cells (tetramer staining) and cytokine secretion (intracellular cytokine staining), respectively. For tetramer staining, the whole blood (50 μL) was treated with ACK lysing buffer (1 mL × 2) at rt for 5 min to lysate the erythrocyte and then transferred to a U-bottom 96-well plate. After washing with FACS buffer (200 μL × 2), the cells were resuspended in tetramer staining buffer [50 μL, PBS containing BSA (1% w/v), EDTA (5 mM), and dasatinib (50 nM)] with iTAg Tetramer/PEH-2 Kb OVA (SIINFEKL) (1 μL) and anti-CD16/32, and incubated at rt for 40 min. Antibodies including FITC-anti-CD8α, PerCP-Cy5.5-anti-CD62L, and BV711-anti-CD44 in a solution of tetramer staining buffer (50 μL) were then added on top of each well, and the cells were incubated at 4 °C for another 10 min. The stained cells were washed with a DAPI solution (0.1 μgmL^{-1}, 150 μL × 2) and resuspended in tetramer staining buffer for flow cytometry analyses.

Intracellular cytokine staining: Blood sample (50 μL) was lysated and transferred to a 96-well plate following a similar procedure with that of tetramer staining. After washing with PBS (200 μL × 2), the cells were resuspended in complete RPMI 1640 medium (200 μL) containing eBioscience™ Cell Stimulation Cocktail (0.4 μL) and incubated at 37 ºC for 6 hours to restimulate the $CD8^+$ T cells. The cells were then spined down and washed with FACS buffer and resuspended with FACS buffer (20 μL) containing anti-CD16/32 (0.3 μL). After incubating at 4 ºC for 15 min, another portion of FACS buffer (20 μL) containing anit-CD3 and anti-CD8 was added on top of each well and incubated at 4°C for 20 min. After washing with PBS (200 μL × 2), the cells were stained with Zombie Aqua™ Fixable Viability Kit. The cells were fixed and permeabilized with the BD Fixation/Permeabilization Kit. After washing with BD Perm/Wash™ buffer (250 μL × 2), the cells were resuspended with BD Perm/Wash™ buffer (20 μL) containing anti-Granzyme B, anti-IFN-γ, and anti-TNF-α antibodies. After 30-min incubation at 4 ºC, the cells were washed with BD Perm/Wash™ buffer (250 μL ×2) and finally resuspended in the FACS buffer (200 μL) for flow cytometry analyses.

Tumor challenging: On day 37 (9 days post the final immunization), the immunized mice (as described above) were challenged subcutaneously with YUMM1.7-OVA cells (5×10^5) on the right flank. Tumor growth was monitored every other day from the fifth day post tumor inoculation. Tumor area (product of two measured orthogonal diameters) and body weight were measured every 2 days. Mice were euthanized when the body weight loss was > 15% of the pre-dosing weight, or the tumor area reached 150 mm^2 (as a pre-determined endpoint), or the animal had become moribund.

In *vivo* therapeutic study

Female C57BL/6 mice were subcutaneously inoculated with YUMM1.7-OVA cells (5×10^5) on the right flank. The vaccine treatment containing LEQ (15 nmol) and Pam (5 nmol) in a PBS solution (50 μL) in the forms of a simple mixture, an emulsion formulation in Montainide, or PNE(LEQ-Pam) were given on day 5, 12, and 19. Tumor growth was monitored every other day following a similar procedure as described above.

Statistical analysis.

Statistical analysis was performed using GraphPad Prism 8 (GraphPad Software, Inc., La Jolla, CA, USA). Unless otherwise noted, the data are presented as Mean ± SEM. Comparisons of two groups were performed by using a two-tailed unpaired Student's t-test. Comparisons of multiple groups at a single time point were performed by using one-way analysis of variance (ANOVA). Comparisons of survival curves were performed by using Log-rank analysis. P-value were presented as *P < 0.05; ** P < 0.01; *** P < 0.001; **** P < 0.0001.

Safety consideration

No unexpected or unusually high safety hazards were encountered.

This chapter is adapted from the article:

Lixia Wei, Yu Zhao, Xiaomeng Hu, and Li Tang, Redox-Responsive Polycondensate Neoepitope for Enhanced Personalized Cancer Vaccine, ACS Central Science 2020 6 (3), 404-412. DOI: 10.1021/acscentsci.9b01174

Author Contributions:

L.T. and L.W. conceived the idea and designed the experiments, L.W. performed the synthesis, L.W. and Y.Z. performed the characterization, L.W. performed Lymph node (LN) and DC targeting in vivo, BMDC maturation and antigen cross-presentation in vitro, Y.Z. and X.H. repeated the in vivo immunization and antitumor work according to the reviewer's comments, L.T and L.W. writed the manuscript, L.T., L.W., Y.Z., X.H. all edited the manuscript.

Chapter 3 Protein Engineering for Antiviral drug development

Infectious diseases before the twentieth century were responsible for the largest global burden of human population death and disability. Over the last few centuries, global pandemics of infectious diseases, such as smallpox, cholera, and influenza, periodically threatened the survival of entire populations until the development of better living conditions like sanitation and clean water supplies in the late 1800s.

Another big contribution to dramatically decreasing infectious disease mortality is the development of various antibiotics as well as safe, effective, and affordable vaccines in the mid-twentieth century. An ultimate goal for emerging infectious diseases is eradication. However, to date, there are only two diseases declared to be eradicated due to global immunization: smallpox in humans, which was responsible for 300 to 500 million deaths in the 20th century, and rinderpest in cattle and other ruminant animals. Wild Poliovirus has been eliminated from all countries except three (Afghanistan, Nigeria, and Pakistan); Yaws, Guinea worm, and Malaria infections elimination are also being investigated.[91,92]

Based on the huge success of applying prophylactic vaccines to decline these infectious diseases, researchers have also started developing vaccines for other infectious diseases like human immunodeficiency virus/acquired immune deficiency syndrome (HIV/AIDS), tuberculosis (TB), malaria, hepatitis C, and a variety of neglected tropical diseases (NTDs). However, research and development of a vaccine for an infectious pathogen usually take between 10 to 15 years. At the same time, new emerging pandemic viral infections remain a constant threat due to increasingly frequent close contact between the human population and animals. The most recent such infections include severe acute respiratory syndrome (SARS) 2003, swine flu (H1N1) 2009, Middle East Respiratory Syndrome (MERS) 2012, the largest Ebola outbreak 2013-2016 in the West African region where it had never caused an outbreak before, Zika 2016 with its associated neurological disorders,[93]and the novel severe acute respiratory syndrome coronavirus 2 (SARS-CoV-2) 2019 engulfed the whole world in less than 6 months and caused more than 413 million people infected and more than 5 million deaths (as of 15-Feb-2022, John

Hopkins Corona Dashboard center) together with severely disrupted world economy.[94] However, major pandemics of other pathogens are not predictable.

Although developing and applying vaccines for those infectious diseases is the final goal to eradicate the infection, understanding the emerging pathogen and developing a safe and effective vaccine takes a relatively long time (typical 10-15 years except around 1 year for COVID-19 mRNA vaccine). However, during the vaccine development time, people mortality, world economic disruption, countless pain and panic of broken families cannot be paused. Non-vaccine available infectious diseases like HIV/AIDS, tuberculosis, and malaria, as well as diarrheal diseases and lower respiratory infections, are still a heavy burden for both medical and economic costs. In particular, the failure to respond to the Ebola outbreak in a timely and coordinated fashion before it spiralled out of control—infecting over 28,000 people and causing over 11,000 deaths—was a wake-up call for the world.[95] SARS-CoV-2 is still the cause of a global pandemic today, with control and mitigation measures limited to social distancing, wearing masks, travel restrictions, and avoiding gatherings, which are all imperfect and constraining. This approach is not well suited for the immediate needs of an emerging pandemic infection; a typical example with Ebola and COVID-19 infection cases and vaccine development comparison (Figure 3.1) shows the dramatic timeline differences.[94]

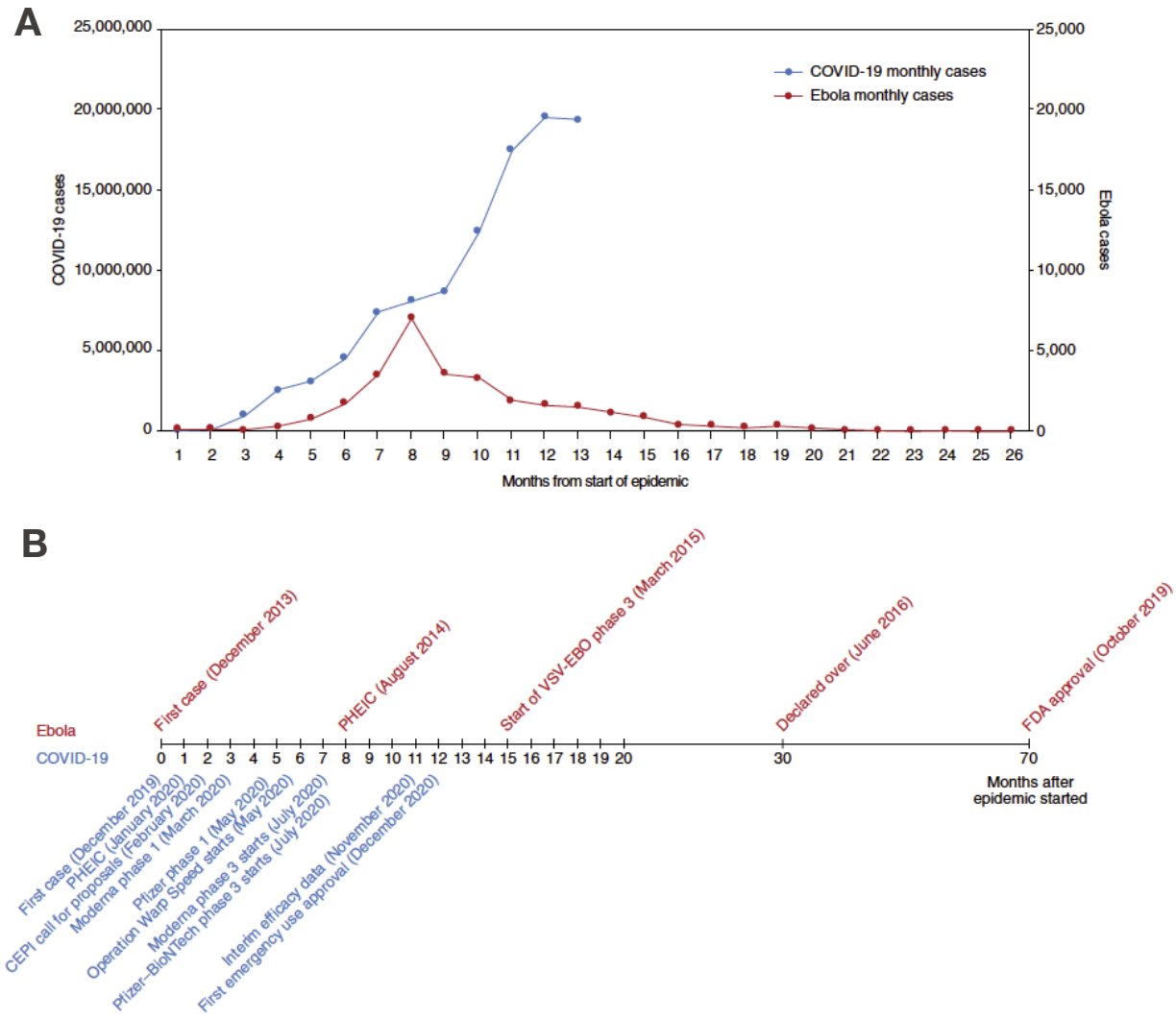

Figure 3.1. A comparison of the epidemic curves and vaccine development timelines between the 2014 West African Ebola outbreak and COVID-19.

A) The number of months from the onset of the epidemic is shown against the number of reported cases per day. Note that the COVID-19 (left) and Ebola (right) axes are scaled differently; B) Vaccine development timelines for COVID-19 versus Ebola in the context of particular events during the respective outbreaks. PHEIC, public health emergency of international concern.[94]

Infectious diseases that persist require continues effort to develop vaccines, but at the same time, antiviral drugs, especially broad-spectrum inhibition of various viruses, are desirable for decreasing or slowing down the infection cases, mortality, and buying time for final vaccine development. The benefit of antiviral drugs for certain non-vaccine available infectious diseases is very encouraging. For instance, HIV/AIDS declined 50 % between 2004 and 2015, thanks to an unprecedented expansion of life-saving antiretroviral therapy to over 18 million

people.[96] Similarly, fewer children and adults die from malaria, diarrheal diseases, and lower respiratory infections due to antiviral drugs treatment.

Drugs to fight infectious disease include antibiotics, antifungal and antiparasitic drugs, or antiviral drugs based on monoclonal antibodies.[97] Most antiviral drugs currently available are designed to target viral infections, including HIV/AIDS, herpes virus, hepatitis B and C, and influenza A and B. Researchers are always trying to extend the range of antiviral drugs to other families of pathogens. However, because viruses tend to use the host's cells to replicate, it is challenging to design safe and effective antiviral drugs with minimal interference with the host organism's cells while maintaining effective inhibition of the viruses. Moreover, viruses are constantly mutating, which increases the obstacles for effective antiviral drugs development.

Viruses usually consist of a genome with or without a few enzymes inside of a capsule structure made of proteins (capsid), sometimes also covered with a lipid layer (envelop). They cannot reproduce on their own but have to rely on a host cell to produce copies for further propagation and infection. Based on virus-specific infection life cycles, researchers have developed rational antiviral drug design strategies such as attacking viruses at every stage of their life cycles. Different types of viruses have different life cycles, but they still share a general pattern (Figure 3.2): 1. Attachment to a host cell; 2. Fusion with the cell membrane, enter and release of viral genes inside the cell; 3. Replication of viral components using host cell machinery; 4. Assemble viral components; 5. Release new assembled viral particles.

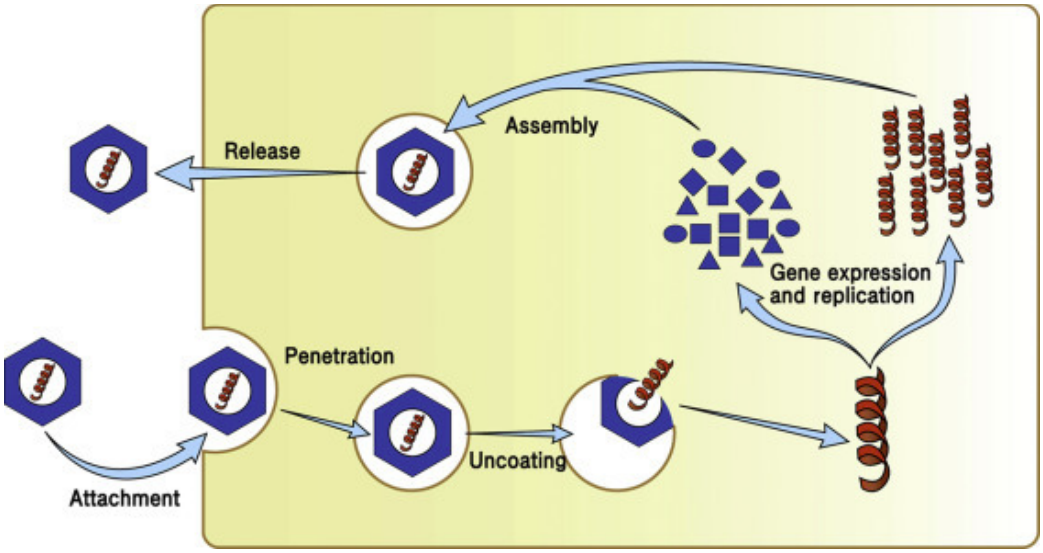

Figure 3.2. The life cycle of virus[98]

Based on this pattern of the viral infection cycle, one antiviral strategy is to block the ability of the virus from attaching to the host cell membrane and releasing its viral genes. By mimicking the virus-associated protein (VAP) to develop analogues of targeting protein, it can compete with binding to cellular receptors to reduce the virus attachment. These types of antiviral drugs include VAP anti-idiotype antibodies, natural ligands of the cellular receptor, and anti-receptor antibodies. Another strategy is to design a compound to mimic the cellular receptor and bind to the VAP, which includes receptor anti-idiotypic antibodies, extraneous and synthetic receptor mimics, and anti-VAP antibodies. One typical example of these "entry-blocking" antiviral drugs for HIV/AIDS treatment is fusion inhibitor- "Enfuvirtide",[99] virus glycoprotein gp120 attachment inhibitor-"Fostemsavir",[100] and CD4 T cell surface receptor CCR5 antagonist-"Maraviroc".[101] Another uncoating inhibitor preventing viral gene release such as "Amantadine" and "Rimantadine", which act on virus penetration and uncoating, for influenza treatment have also been developed.[102–105]

The primary type of antiviral drugs interferes with the synthesis and assembly of virus components after they invade a host cell. It includes reverse transcription inhibition by developing nucleotide or nucleoside analogues such as "Aciclovir" for herpesvirus infection,[106] "Zidovudine (AZT)", "Lamivudine" and "RNase H" for HIV/AIDS infection,[107–109] DNA integrase target, transcription inhibition for blocking attachment of transcription factors to viral DNA, "antisense" molecules -segments of DNA or RNA- aiming for blocking viral genomes operation like "Fomivirsen" for cytomegalovirus,[110] "Morpholino oligos" for caliciviruses, flaviviruses, dengue, HCV and coronaviruses.[111–115] Antiviral drugs can also target downstream translation such as ribozymes analogues that have been developed for hepatitis C and HIV,[116,117] which cut DNA and RNA at sites to disable viral genome, interfering with viral protein processing like protease inhibitor,[118] targeting the viral long dsRNA helix forming,[119] and virus assembly such as "Rifampicin".[120]

As the final stage of a virus infection cycle is to release the newly assembled virus particles, researchers developed two drugs named "Zanamivir" and "Oseltamivir" to block the surface molecule neuraminidase to prevent viral particle release for influenza infection treatment.[121,122]

Instead of attacking viruses directly, researchers are also trying to combat viruses by improving people's own immune systems. Some immune-stimulating molecules have been

used for antiviral purposes like INFa for treatment of hepatitis B and C.[123] Monoclonal antibodies purified from infected patients or synthesized have also been used for antiviral treatment.

Currently, available antiviral drugs approved by FDA are mostly small molecules such as "Acyclovir", "brivudine", "Famciclovir" for HSV; "Amantadine", "Rimantadine", "Zanamivir" for influenza; "Ribavirin" for hepatitis virus;[124] "Abacavir", "Lamivudine" for HIV/AIDS,[125] and "Molnupiravir" for SARS-CoV-2.[126] These molecules usually have high specificity, however, the shortcoming is easily causing drug resistance. The other approved antiviral drugs are focused on natural proteins like "Interferons" for hepatitis[124] and monoclonal antibodies for various viruses,[127] but they are usually very costly. In order to address the problem, researchers also actively develop macromolecular-based broad-spectrum antiviral agents against new emerging viruses like Zika, Ebola, SARS, and other pathogenic viruses because the conventional one-bug-one-drug strategy is insufficient to address this problem.[128]

Macromolecules are particularly attractive due to their multivalency and versatility, and they can be designed to display broad-spectrum antiviral activity and lower the risk of drug resistance for emerging and muted viruses. For instance, peptide- and polymer-based antivirals can easily achieve multivalency with diverse functionalities.[129,130] Kuroki *et al*.[131] reviewed antiviral peptides like cationic peptides displaying broad-spectrum antiviral function through competitively binding to heparan sulfate proteoglycans (HSPGs) on the host cell surface, viral fusion inhibitor mimicking peptides by disrupting membrane fusion between virions and host cells, and antiviral polymers including HSPGs mimicking sulfated polysaccharides and glycopolymers for binding to viruses from attachment, improved plasma half-life and biocompatibility sulfated/sulfonated non-glycosylated polymers, sialylated polymers mainly for influenza viruses, nucleic acid polymers for blocking the secretion of newly formed virions, amine-functionalized polymers, and guanidine-functionalized polymers.

Macromolecule antivirals such as polymer-drug conjugates improve the drug half-life in blood circulation and prevent it from unwanted interactions with proteins, cells, and non-target organs.[132] For example, "zidovudine" for HIV was conjugated to carrageenan and other polymers in order to improve stability, specific organ targeting, and lower drug resistance and toxicity.[133,134] Furthermore, nanoparticle-based macromolecule antivirals have also been actively investigated. Carbon dots (CDs), carbon nanotubes, silver nanoparticles, silica nanoparticles, gold nanoparticles, gold nanoclusters, graphene oxides, etc., were shown to have antiviral

or antibacterial effects.[135–143] Natural antiviral drugs derived from microbial products also exhibit great structural diversity, complexity, and broad-spectrum antiviral function.[144]

Despite the rapid progress in the biomedical techniques of antiviral drug development, there are still many challenges to discover new promising antiviral targets and drugs. Among the 30-year period from January 1987 to December 2017, 179 antivirals were approved by FDA.[145] Although there are so many available antiviral drugs, they only target a small number of viral pathogens.[145,146] In particular, most approved antivirals are small molecules specifically targeting certain virion parts. However, viruses, particularly RNA viruses, sustain a high frequency of mutations, which cause viruses to become resistant to currently available treatments.[118] Although mechanisms of antiviral resistance vary between different viruses; antiviral drug resistance is possible for a range of viruses. Current antiviral resistance has been reported for HIV, hepatitis B and C, herpes, and Influenza.[147] Except the drug resistance, another challenge for current available small molecule-based antivirals is their side-effects such as toxicity, half-life circulation, off-targeting tissue, thus there is a high demand for proper drug delivery systems.[148–150]

It usually takes years to develop and get a new antiviral drug approved for use because identifying the chemical compounds targeting the virus, testing its efficacy and safety both in the preclinical and clinical setting is a long and costly process. However, with the high frequency of virus mutation, new emerging and re-emerging viruses make the antiviral drug development even longer, which makes it unlikely to result in timely and effective therapies against these numerous pathogens causing sometimes rare but lethal infections.[151] Based on these observations, broad-spectrum antivirals that can act on multiple viruses are highly desirable. However, unlike bacterial, viruses have much less of their own proteins that can be targeted with drugs since they use host cellular machinery for replication. Thus, a broad-spectrum antiviral targeting a virion specifically but not affecting normal cell function is particularly difficult. “Ribavirin” is the only approved broad-spectrum antiviral for various RNA viruses. Despite these difficulties, targeting viruses’ conservative proteins outside of host cells to stop them from attachment or fusion is a good strategy for developing broad-spectrum antivirals. Natural proteins such as interferon-lambda (IFN-λ) immune modulator and broad-spectrum neutralizing antibodies show effective inhibition function against various viruses.[152–154] Alternative approaches like synthetic antiviral gold nanoparticles coated with HSPGs -a common cell surface receptor shared by various viruses for binding- mimicking linkers were reported with good

inhibition against various viruses such as HSV-2, HPV, RSV, and dengue.[143] Direct targeting of virus particles offer the potential to stop viruses before infection of host cells, which will greatly reduce virus infectivity levels, accelerate recovery while reducing transmission risks.[155]

Despite great efforts on the development of broad-spectrum antivirals, there is still one more critical question that has not been addressed yet. Most current available antivirals are aiming to interfere with the virus entry; hence they are virustatic substances. They can be broad-spectrum and non-toxic, but their inhibition effect highly depends on a reversible binding event. Once upon dilution of the substance, the inhibition binding to the virus will be disassociated, and the virus can infect the host cell again. Several examples were reported with this virustatic effect.[156–159] A compound with a virucidal mechanism of action interacts with viruses to irreversibly deactivate them. The ideal antivirals should be both medical virucidal to virus and non-toxic to host cells. However, the current available virucidal materials such as detergents, strong acids, even some newly developed nanoparticles and polymers all present high cellular toxicity.[160,161] With the increasing emergence of new viruses, there has been more interest in developing non-toxic virucidal antivirals. For instance, Cagno *et al.*[143] developed HSPGs mimicking linker-coated gold nanoparticles for successful broad-spectrum antiviral activities together with non-toxicity to host cells. Chakrabarty *et al.*[162] also screened drugs that can combine medical virucidal and virustatic activities for HIV treatment. These works allow potential prevention and treatment for future emerging viruses.

Here we demonstrate a protein-based novel and versatile approach for broad-spectrum virucidal material development. Through a one-step reaction by simply chemically conjugating a long flexible and hydrophobic ligand onto the surface of a protein core, we prepared a functionalized protein virucidal material with good safety and effectiveness against HSV-2, Influenza H1N1, and SARS-CoV-2 (Figure 3.3).

To prove this concept, we used bovine serum albumin (BSA), the most abundant serum protein, as the core. By varying ligand density, we tuned the inhibitory activity of the antiviral material: the antiviral inhibition EC_{50} increased from 0.052 μM (56% ligand density) to 23.6 μM (22% ligand density) to loss of all inhibition (11% ligand density). We also demonstrate the versatility of this approach to turn proteins, across a range of isoelectric points and molecular weights, into an effective antiviral material by applying the conjugation method to a variety of protein cores. By simply replacing the protein core from BSA to Avidin to Cytochrome C

while maintaining the same synthesis method, all products still show effective antiviral inhibition ($EC_{50\text{-}BSA}$ = 0.052 µM, $EC_{50\text{-}Avidin}$ = 0.208 µM, $EC_{50\text{-}Cyto\ C}$ = 0.592 µM).

Furthermore, by varying ligand hydrophobic length from 3 to 6 to 12 -CH_2-, final products' antiviral inhibition EC_{50} remains in a similar range but converts from virustatic (3 and 6 -CH_2-) to virucidal (12 -CH_2-). At last, modified protein BSA with ligand DMDA of 12 -CH_2- was prepared and used for antiviral inhibition test against three different types of viruses HSV-2, Influenza H1N1, and SARS-CoV-2. This product showed effective antiviral inhibition against all these three viruses with $EC_{50\text{-}HSV\text{-}2}$ = 0.149 µM, $EC_{50\text{-}H1N1}$ = 4.48 nM and $EC_{50\text{-}SARS\text{-}CoV\text{-}2}$ = 2.42 µM. Thus, this protein-based antiviral platform provided an easy-manufactured, versatile, non-toxic, broad-spectrum effective, and potentially translatable antiviral solution.

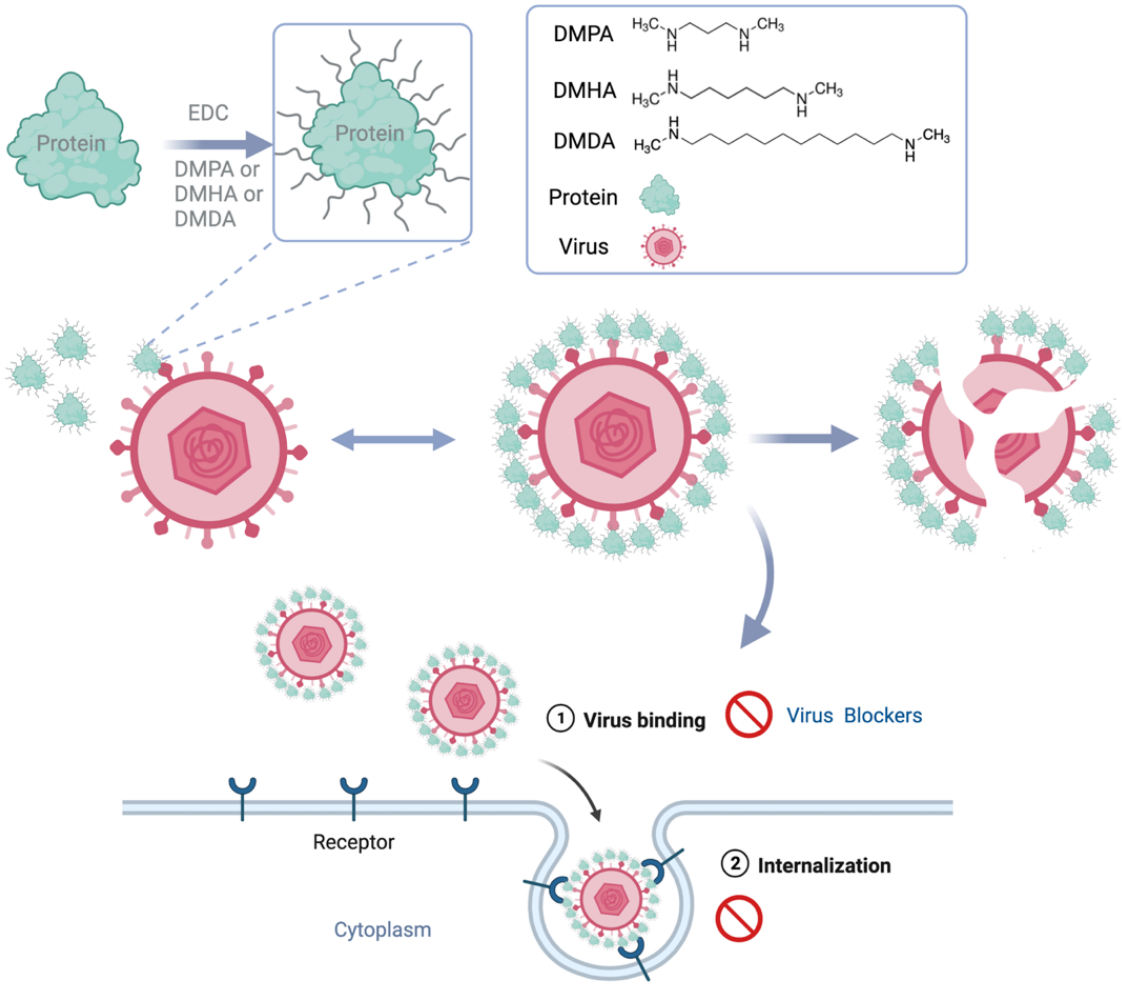

Figure 3.3. Schematic illustration of antiviral drug chemical synthesis, virustatic and virucidal inhibition.

3.1 Chemical synthesis and characterization of protein-based antivirals

To date, the reported protein-based antivirals are either interferons or monoclonal antibodies, the mechanism of viral inhibition is virustatic, and they are usually very costly. Here we developed a simple one-step protein functionalization method to produce non-toxic virucidal materials. Proteins are ideal scaffolds for biomaterial design as they are biocompatible and have diverse surface charges and a range of functional handles on which to conjugate active ligands. We hypothesized that modifying a protein core with ligands that irreversibly interact with virus capsid proteins could result in an antiviral material.

For the ligand, we investigated three diamine compounds of varying hydrophobicity: N, N′-Dimethyl-1,3-propane diamine (DMPA), N, N′-Dimethyl-1,6-hexane diamine (DMHA), N, N'-Dimethyldodecane-1,12-diamine (DMDA). To investigate whether we could exploit any generic protein as a core to uniformly modify with a virus targeting ligand, we selected three model proteins of varying isoelectric point and molecular weight: BSA (67 kDa, pI:4.7), Avidin (67 kDa, pI:10), and Cytochrome C (11.7 kDa, pI:9.6). The protein cores were functionalized with the diamine ligands using 1-Ethyl-3-(3-dimethylaminopropyl) carbodiimide (EDC) coupling chemistry in aqueous conditions at room temperature. The ligand to protein ratio was determined using the protein crystal structure to estimate the number of surface accessible carboxyl groups on which to conjugate the diamine linker. The chemical synthesis scheme is displayed in Figure 3.4A. Modified proteins were purified using amicon centrifugal filtration with molecular weight cutoff dictated by the protein core.

The unmodified and modified proteins were characterized using a range of techniques to investigate the size, surface charge, and degree of functionalization. Dynamic light scattering (DLS) (Figure 3.4B upper left) of functionalized protein sample BSA-DMPA showed around 2 nm increase in the hydrodynamic diameter post modification, while the surface zeta potential (Figure 3.4B upper middle) increased from -1.16 to +21.1 mV mainly due to the positive charge of the amine group of the ligand. Matrix-assisted laser desorption/ionization (MALDI) Mass Spectrum (Figure 3.4B upper right) clearly showed increased mass 5710 after modification, which indicates ~56 ligands conjugated on each protein. The modified and unmodified BSA, Avidin, Cytochrome C with various ligands were characterized by DLS, Zeta potential, MALDI

Mass Spectrometry, and summarized data are listed in Table 3-1. Conjugated ligand numbers were also calculated and listed in the right column in Table 3-1.

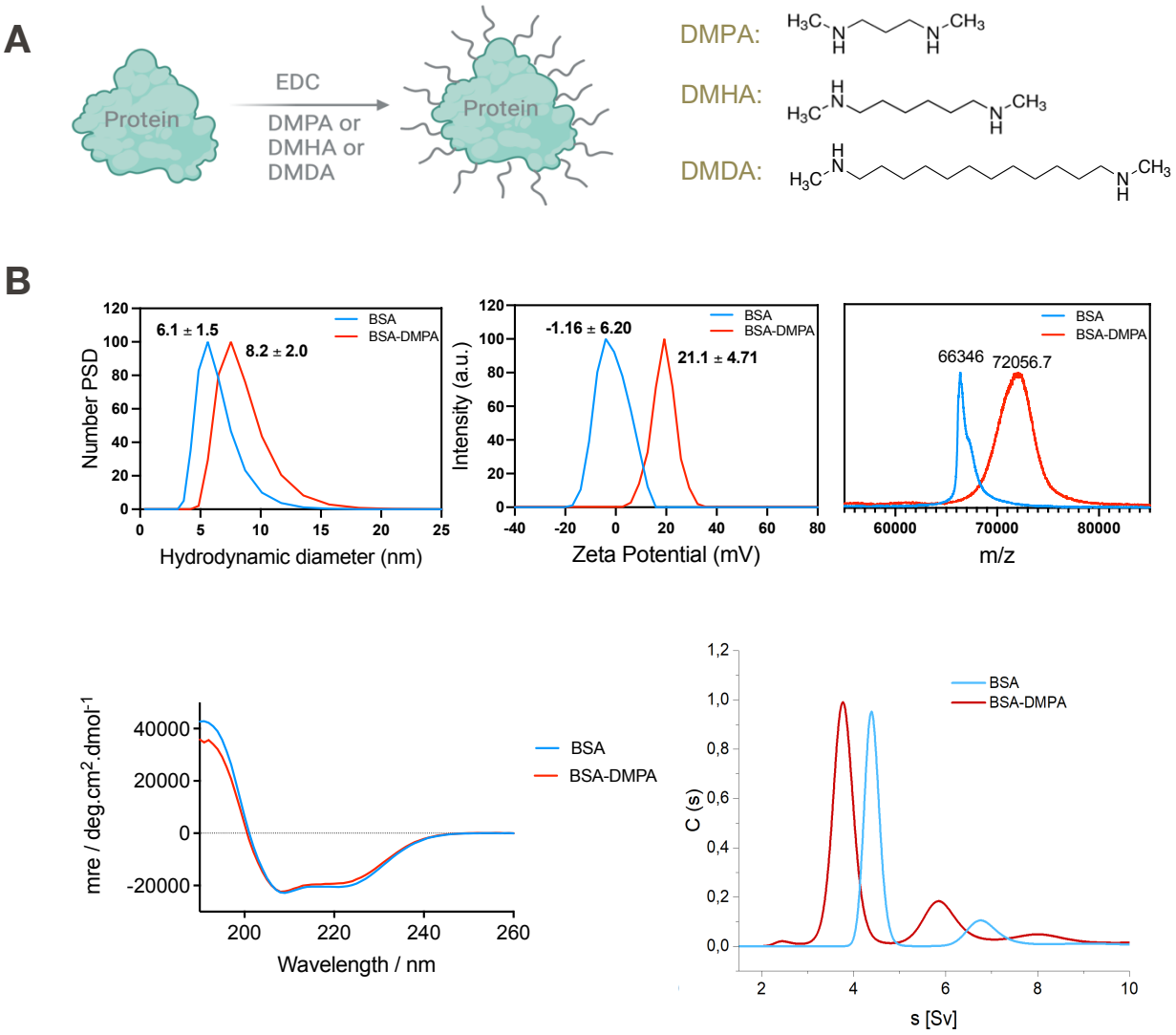

Figure 3.4. Synthesis and Characterizations of protein-based antivirals.

A) Synthetic schematic illustration of one-step chemical functionalization of protein surface with ligand DMPA, DMHA, and DMDA. B) Characterization of functionated protein representor BSA-DMPA with DLS (upper left), Zeta potential (upper middle), MALDI Mass spectrum (upper right), CD (lower left), and AUC (lower right).

Table 3-1. Physiochemical properties of native and functionalized proteins

Sample/ Characterization	DLS (nm)	Zeta potential (mV)	Mass Spectrum (MW)	Ligand number per protein
BSA	6.1 ± 1.5	-1.2 ± 6.2	66346	
BSA-DMPA	8.2 ± 2.0	21.1 ± 4.7	72056.7	56
BSA-DMPA (20%)	7.6 ± 2.0	4.7 ± 2.8	68593.3	22
BSA-DMPA (10%)	7.9 ± 2.0	-0.05 ± 6.0	67712.5	13
Avidin	5.1 ± 1.3	4.3 ± 9.2	63564	
Avidin-DMPA	5.6 ± 1.4	9.5 ± 8.5	66098	25
Cyto C	1.2 ± 0.3	2.0 ± 5.6	12179	
Cyto C-DMPA	2.2 ± 0.3	18.2 ± 12.9	13084	9
BSA-DMHA	7.4 ± 2.0	6.4 ± 14.6	71682	37
BSA-DMDA	7.7 ± 2.0	23.4 ± 6.0	71379	22

In order to investigate if the protein structure changed after ligand functionalization, we performed circular dichroism (CD) spectroscopy (Figure 3.4B lower left) of protein BSA and its functionalized form BSA-DMPA. We can see that both of the sample curves are basically overlapped together, which indicates after functionalization with the ligand, the α-helix and β-sheet content of the protein didn't significantly change compared to its original form. Since structure and function are intimately linked, the retention of protein structure post-modification is indicative of retention of protein function and thus promising for utilization of future functional protein cores. Furthermore, characterization by analytical ultracentrifugation (AUC) (Figure 3.4B lower right) of sample BSA and BSA-DMPA provides two types of important information: the first one is sample BSA-DMPA is clean and uniform, as we can see that native BSA protein displayed two peaks with different sedimentation due to its natural monomer and dimer. After conjugating with ligand DMPA, there are still only two peaks; the major one is the monomer, which indicates that ligands were covalently bonded with protein but did not cross-link two proteins together or cause unwanted aggregation. Second, AUC reveals that the ligand was conjugated on the surface of protein quite uniformly as the width of the peak didn't change much compared to native BSA. Additionally, the peak left-shifted compared to BSA indicates the BSA-DMPA sediments slower than BSA, which we suspect is because, after ligand conjugation, the whole protein particle density becomes smaller, resulting in slower sedimentation.

3.2 Ligand density influence on antiviral effect

Our goal is to develop an effective and non-toxic antiviral material through functionalizing protein surfaces with certain ligands. The first question to address is how many ligands are needed on the protein core in order to achieve an effective inhibition. Although the number of the ligands might vary according to different protein cores, we hypothesize that there may be an ideal number of ligands per protein surface area required to have a desired antiviral effect. Here, we use BSA as protein core and DMPA as a ligand to investigate the ligand density effect on antiviral inhibition. Since the EDC coupling reaction mechanism is first to let EDC molecules activate the carboxyl group, there are in total 99 carboxyl groups available on each BSA protein (determined by total amino acids Aspartic Acids and Glutamic Acids) by tuning input ligand ratios during the EDC carboxyl activation reaction, we managed to get three different ligand density samples: 56 ligands conjugated sample BSA-DMPA, 22 ligands conjugated sample BSA-DMPA 20% and 13 ligands conjugated sample BSA-DMPA 10%. The name of 20% and 10% is based on the input ligand ratio compared to sample BSA-DMPA maximum ligand density ratio achievable via EDC coupling.

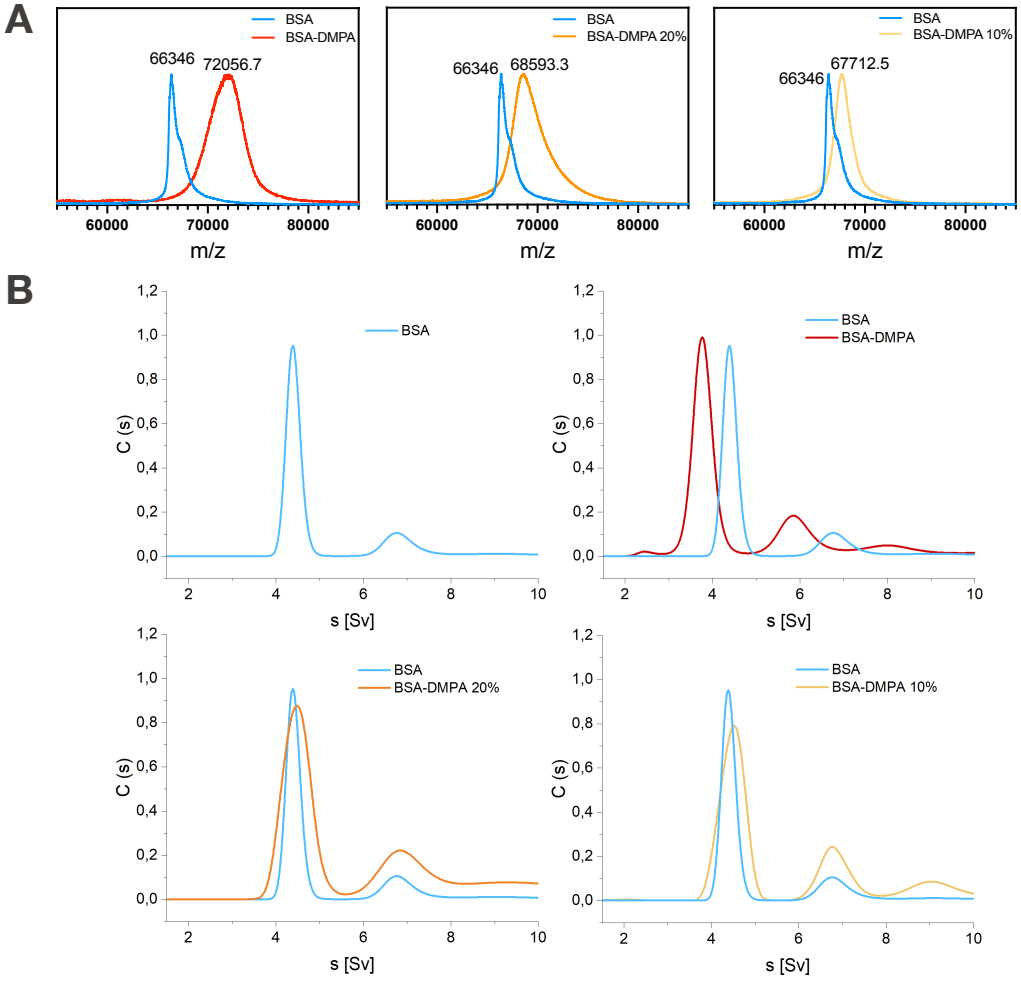

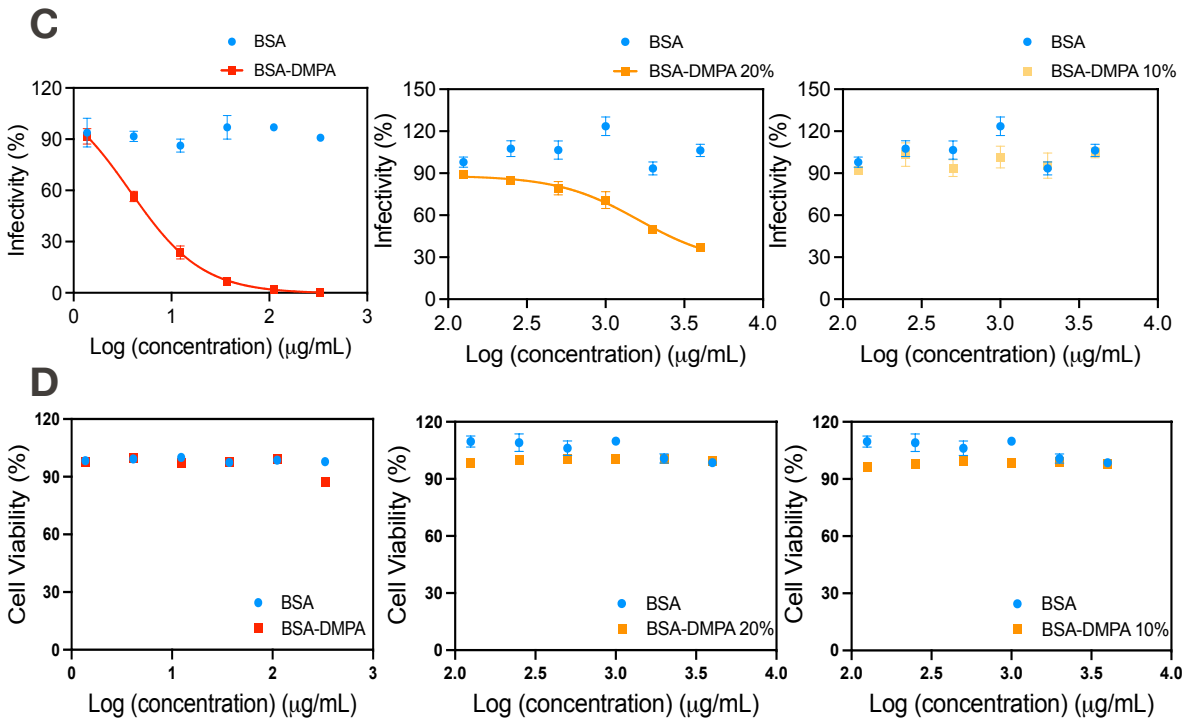

Figure 3.5. Ligand density influence on the effect of antiviral inhibition.

A) MALDI Mass Spectrum of different ligand density samples BSA-DMPA, BSA-DMPA 20%, and BSA-DMPA 10%. B) AUC characterization of native protein BSA and different ligand density samples BSA-DMPA, BSA-DMPA 20%, BSA-DMPA 10%. C) Dose-response antiviral inhibition assay of different ligand density samples to HSV-2. D) Cytotoxicity assay for different ligand density samples on Vero cells.

Ligand number calculated from MALDI Mass Spectrums (Figure 3.5A) shows that there are respectively 56, 22, and 13 for each sample BSA-DMPA, BSA-DMPA 20% and BSA-DMPA 10%. Besides, AUC characterization also shows different conjugated ligand numbers according to their sedimentation time. From AUC, an increasing number of ligands conjugated on the protein lowers the whole protein particle density, which results in slower sedimentation compared to proteins with fewer ligands conjugated. From Figure 3.5B, we can clearly see sample BSA-DMPA left-shifted (slower sedimentation) more than sample BSA-DMPA 20% and BSA-DMPA 10% when compared to native protein BSA, which indicates a higher

conjugated ligand number. The BSA-DMPA 20% sample is slightly more left-shifted than the 10% one, while the sedimentation of sample BSA-DMPA 10% is very close to native protein BSA.

After confirming the sample ligand density from both mass spectrum and AUC characterization, we further tested their antiviral inhibition effect against Herpes simplex virus -2 (HSV-2) in *vitro*. To test antiviral inhibition, we used a standard dose-response inhibition assay. In this assay, antiviral material with different concentrations is mixed with a fixed number of viruses and then infect Vero cells; virus-causing plagues are counted after staining. Each sample material was dissolved in Vero cell culture medium DMEM with 2% of Fetal Bovine Serum (FBS) inside and incubated with HSV-2 for 1 hour at cell culture incubator at 37 °C with 5% CO_2. After that, material-virus mixed solutions were added into Vero cells for infection. Virus plagues inside the cell were stained the next day and counted. A dose-response non-linear curve was fitted, and the EC_{50} value was calculated and displayed in Figure 3.5C. The blue dots represent native unmodified BSA protein, which did not show any antiviral inhibition. The BSA-DMPA with maximum ligand density (red curve in Figure 3.5C left) displayed effective inhibition of HSV-2 with EC_{50} concentration equals to 3.77 μg/mL (0.052 μM). However, for reducing ligand density, the anti-HSV-2 EC_{50} concentration dramatically increased, where BSA-DMPA 20% had an EC_{50} of 1.62 mg/mL (23.6 μM), and BSA-DMPA 10% didn't show any inhibition effect. Thus, we found that ligand density on the protein core is one of the key factors for effective antiviral inhibition. While the modified BSA displayed antiviral properties, we wanted to ensure that this antiviral effect was not associated with cytotoxicity. To measure cytotoxicity, we ran cell viability assays on each of the modified protein samples. Figure 3.5D showed over 95% cell viability over the range of modified protein concentrations tested in the antiviral dose-response assay, further demonstrating the non-toxic property of materials.

3.3 Versatility of protein-based antiviral platform

To investigate the versatility of the protein-based antiviral platform, we applied the same chemical modification approach described in section 3.1 to three model proteins with varying molecular weight and isoelectric points: BSA (67 KDa, pI: 4.7), Avidin (67 KDa, pI: 10), Cytochrome C (11.7 KDa, pI: 9.6) (Figure 3.6A). The same chemical synthesis and purification protocol were applied to these different proteins. Dose-response antiviral inhibition

assays against HSV-2 and cytotoxicity assays on Vero cells were performed under the same conditions (Figure 3.6B).

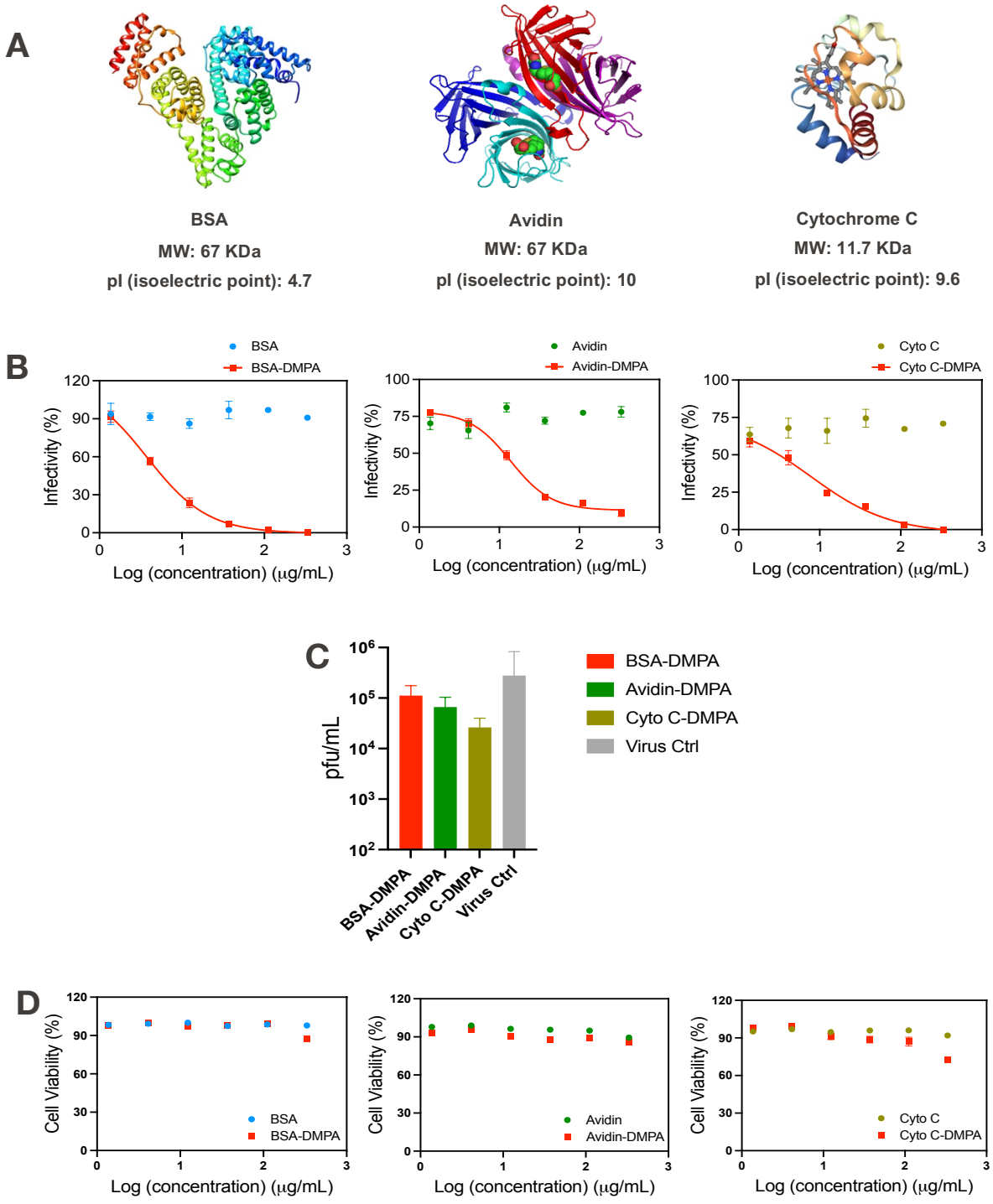

Figure 3.6. Versatility of protein-based antiviral platform.

A) Three protein candidates, BSA, Avidin, and cytochrome C, by varying molecular weight and isoelectric point. B) Dose-response antiviral inhibition of functionalized protein BSA-DMPA, Avidin-DMPA, and Cyto C-DMPA together with their native protein control against HSV-2. C) Virucidal assay of functionalized protein BSA-DMPA, Avidin-DMPA, and Cyto C-DMPA against HSV-2. D) Cytotoxicity assay on Vero cells of functionalized proteins with the same range of concentration in dose-response antiviral inhibition assay.

All three functionalized proteins showed effective inhibition with low EC_{50} values (EC_{50} < 1 μM): BSA-DMPA 3.77 μg/mL (0.052 μM), Avidin-DMPA 13.76 μg/mL (0.208 μM), Cyto C-DMPA 7.75 μg/mL (0.592 μM), which indicates the protein-based antivirals platform is versatile and can potentially be used for functional proteins in the future (e.g., enzymes, antibodies, cell receptors). Encouraged by the good antiviral inhibition effect of these materials, we further investigated to see if these samples were virucidal. 300 μg/mL final concentration of each functionalized protein sample was incubated with a titer of HSV-2 10^6 pfu in 2% FBS containing DMEM medium for 1 hour in cell culture incubator at 37 °C with 5% CO_2, then the material-virus mixture was added into Vero cells for infection, and we perform various serial dilutions from 1:3 to 1:2187000 times, the purpose of these massive dilutions is to see if the material still exhibits antiviral inhibition even when the sample is significantly diluted, indicates that it is an irreversible interaction with viruses. Virus infection formed plaque was counted after staining with crystal violet; the result is shown in Figure 3.6C. However, virus titer only decreased with a very minimal level (< 10-fold) compared to its virus alone control. It means although these three proteins functionalized with ligand DMPA can bind to virus surface effectively to prevent the virus from further infection, the binding between virus and material, however, is reversible. After multiple serial dilutions applied to virus-material mixtures, the de-association effect between virus and material becomes increasingly more dominant; thus, previously blocked viruses will become free and active again for the further infection.

The same concentration range for these functionalized proteins was also evaluated for cell viability on Vero cells (Figure 3.6D). Sample BSA-DMPA and Avidin-DMPA display over 95% cell viability in all tested concentration ranges, sample Cyto C-DMPA displays over 90% cell viability in concentration ~111 μg/mL and less, while at higher concentration (e.g., 333 μg/mL), Cyto C-DMPA reduces cell viability to ~75%, which we suspect might due to cell-apoptosis inducing effect of Cytochrome C when it's delivered into the cytosol of the cell.

3.4 Ligand hydrophobicity influence on the antiviral effect

We were encouraged by the protein antiviral results but wanted to optimize the protein modification further to make the material virucidal. For antiviral inhibition through non-specific binding, in order to disrupt the envelop membrane of the virus, ion-interaction between ligand and viral protein is important, and hydrophobic interaction with force interference might be necessary. We hypothesized that there might be a minimum ligand hydrophobicity required for the protein to interact irreversibly with the virus capsid proteins and thus exhibit virucidal inhibition. To explore this hypothesis, we used BSA as a model protein core and selected three different aliphatic ligand chain lengths DMPA (3 -CH_2-), DMHA (6 -CH_2-), and DMDA (12 -CH_2-) for modification to investigate the hydrophobic force influence on virucidal effect. Building off the previous results showing the importance of ligand density, we aimed to maximize the ligand density for each ligand length on the BSA core. By applying the same chemical synthesis protocol to the BSA protein core, we can easily get products BSA-DMPA with conjugated ligand number 56, BSA-DMHA with conjugated ligand number 37, and BSA-DMDA with conjugated ligand number 22 (Table 3-1). The decreased conjugated ligand number is mainly due to the physical hindrance of different length ligands during the reaction, but we believe it can be further improved by optimizing the chemical synthesis reaction condition.

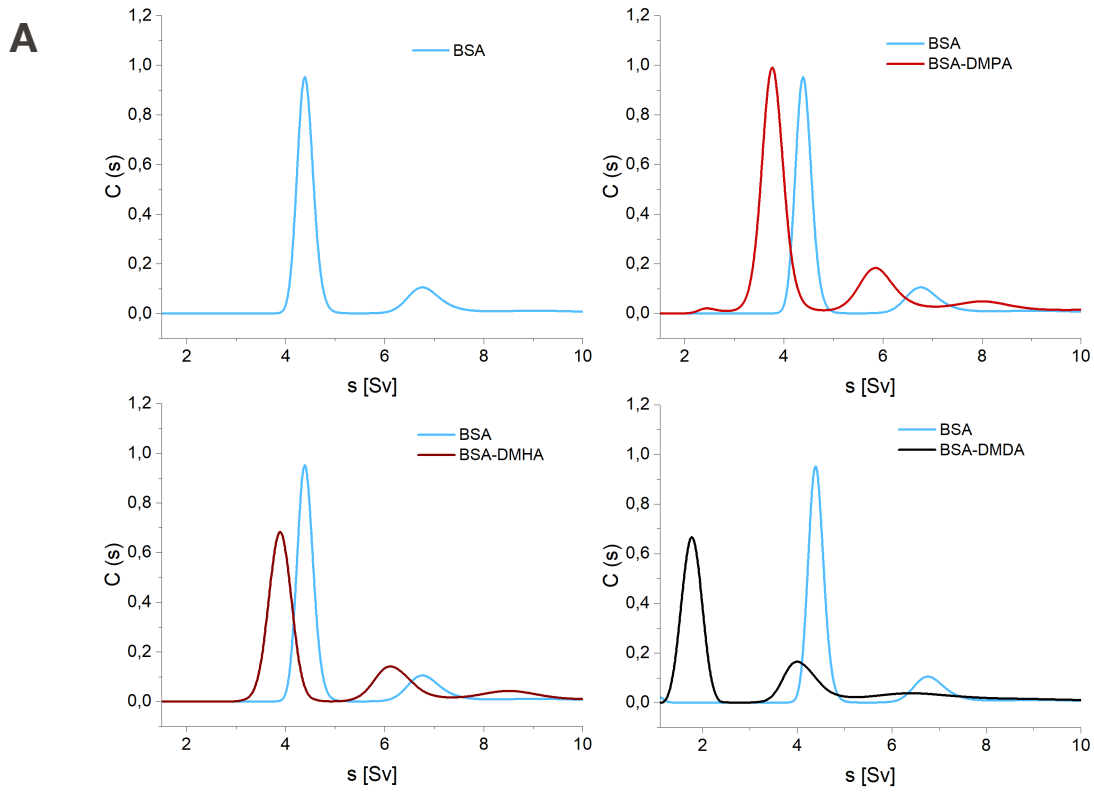

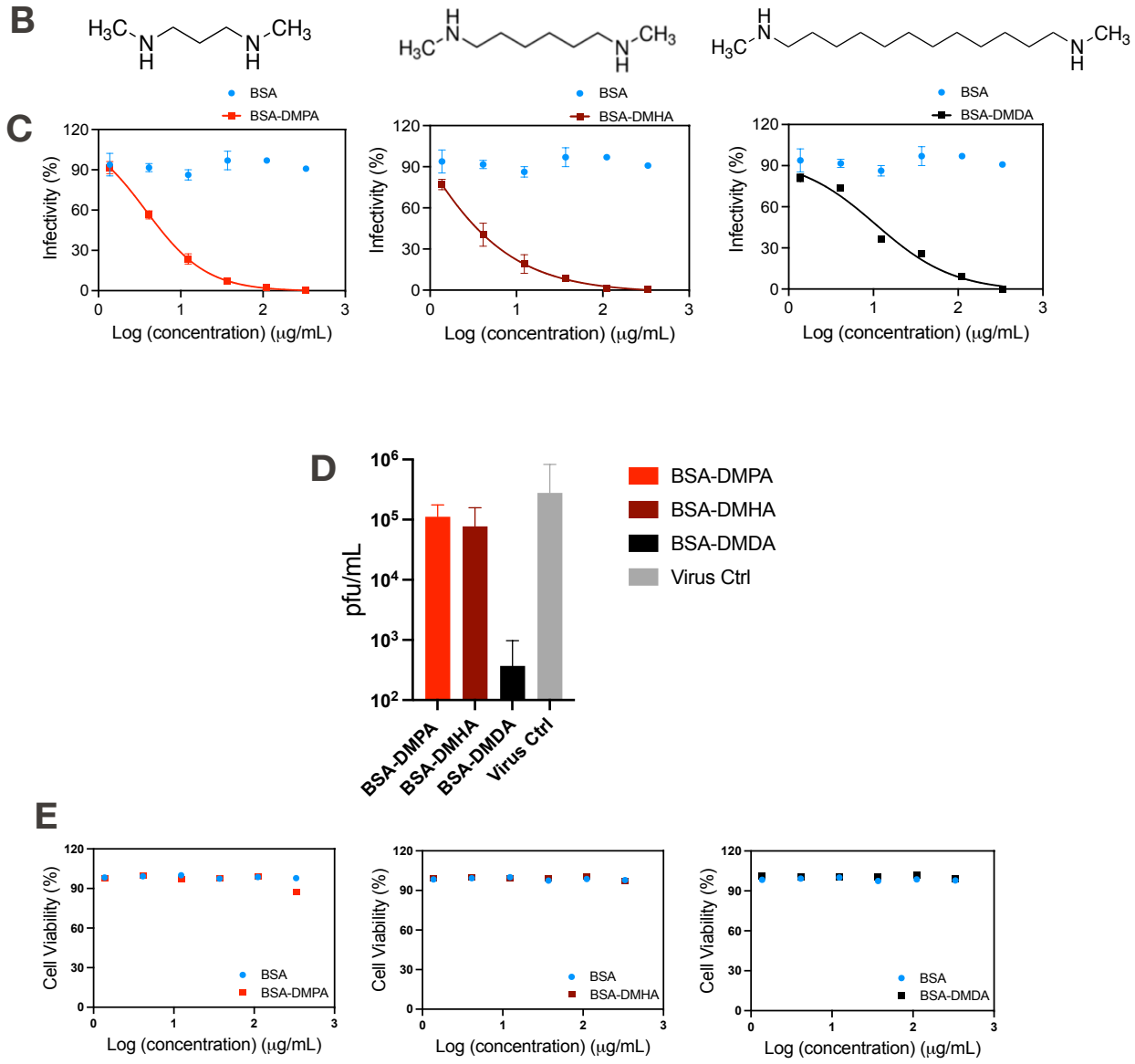

Figure 3.7. Ligand hydrophobicity on antiviral inhibition and virucidal effect.

A) AUC characterization of different lengths of ligand conjugated sample BSA-DMPA, BSA-DMHA, and BSA-DMDA. B) Different length ligand structures: left DMPA, middle DMHA, right DMDA. C) Dose-response antiviral inhibition effect against HSV-2 of different length ligand conjugated BSA protein sample. D) Virucidal effect against HSV-2 of different length ligand conjugated BSA protein sample BSA-DMPA, BSA-DMHA, and BSA-DMDA. E) Cytotoxicity effect of sample BSA-DMPA, BSA-DMHA, and BSA-DMDA in the same concentration range of dose-response antiviral inhibition on Vero cells.

Different length ligand conjugated samples BSA-DMPA, BSA-DMHA, and BSA-DMDA after purification were characterized by AUC (Figure 3.7A). All three samples showed two unique peaks (monomer and dimer), same as native unmodified BSA protein, which indicates all these samples were sufficiently purified. The major peak is monomer also means ligand conjugation didn't cross-link two proteins together or cause undesired aggregation. Furthermore, the sedimentation curves for all BSA samples after conjugating with different ligand lengths are left-shifted, which indicates that these samples sediment slower than native protein mainly because the conjugated ligand makes the whole protein particle much less dense, which is especially apparent in BSA-DMDA sample with the longest ligand.

After careful characterization (Table 3-1), we next performed a dose-response antiviral inhibition assay of these three samples against HSV-2. The protocol of dose-response antiviral assay is the same as above, and results are shown in Figure 3.7C. Sample BSA-DMPA showed anti-HSV-2 EC_{50} equals to 3.77 μg/mL (0.052 μM), and the longer ligand DMHA conjugated sample BSA-DMHA showed an even lower EC_{50} value of 0.43 μg/mL (0.006 μM). Since DMHA has 6 -CH_2-, double the length of DMPA, and conjugated ligand number is 37, less than DMPA's 56 on each protein, it indicates the length of the ligand (hydrophobicity) might play a key role in virus inhibition. Sample BSA-DMDA with 12 -CH_2- has only 22 ligands conjugated due to steric effects in the modification and displayed antiviral inhibition EC_{50} of 10.66 μg/mL (0.149 μM). Its EC_{50} value is slightly higher than BSA-DMPA and BSA-DMHA, likely due to the lower ligand density compared to the other two samples. However, when we compare the EC_{50} of two samples with similar ligand density BSA-DMPA 20% and BSA-DMDA together, the effect of ligand length is very clear. As these two samples have the exact same number of 22 ligands conjugated on each BSA protein, the antiviral EC_{50} value of BSA-DMDA (10.66 μg/mL) is more than 150 times lower than BSA-DMPA 20% (1620 μg/mL), which indicates the importance of ligand length (Hydrophobicity).

To further understand the influence of ligand length (hydrophobicity) on the virucidal effect, we performed a virucidal assay of these three samples, BSA-DMPA, BSA-DMHA, and BSA-DMDA, against HSV-2. The virucidal assay protocol is the same as above. After incubation, infection, and serial dilution, virus plagues were counted compared to virus alone control. Result (Figure 3.7D) shows both sample BSA-DMPA, and BSA-DMHA only displayed minimal virucidal effects; less than 10-fold of the virus titer is decreased compared to virus control. However, even with the lowest ligand density, BSA-DMDA exhibited very effective viricidal

function, where HSV-2 virus titer was decreased around 1000-fold compared to virus control. It further demonstrates the importance of hydrophobic force as one of the key factors to irreversibly inhibit viruses.

Cytotoxicity assay of these three different lengths of ligand conjugated BSA protein samples was performed on Vero cells in the same concentration range as a dose-response antiviral assay. From concentration 1.37 μg/mL to 333 μg/mL (viricidal assay sample concentration is 300 μg/mL), all samples maintain Vero cell viability over 95%, which means these samples are safe for cells even when inducing virus-specific inhibition or irreversible deactivation effect.

3.5 Protein-based antivirals broad-spectrum effect

Encouraged by modified proteins' effective antiviral inhibition and BSA-DMDA's viricidal effect against HSV-2, we next investigated modified protein's broad-spectrum antiviral effect against other viruses such as Influenza H1N1 and SARS-CoV-2. We used modified protein BSA-DMDA as antiviral material and performed a dose-response antiviral inhibition assay against HSV-2, Influenza H1N1, and SARS-CoV-2. The protocols of the dose-response antiviral assay against different viruses are slightly different, which is displayed in the method part in detail. Results are shown in Figure 3.8.

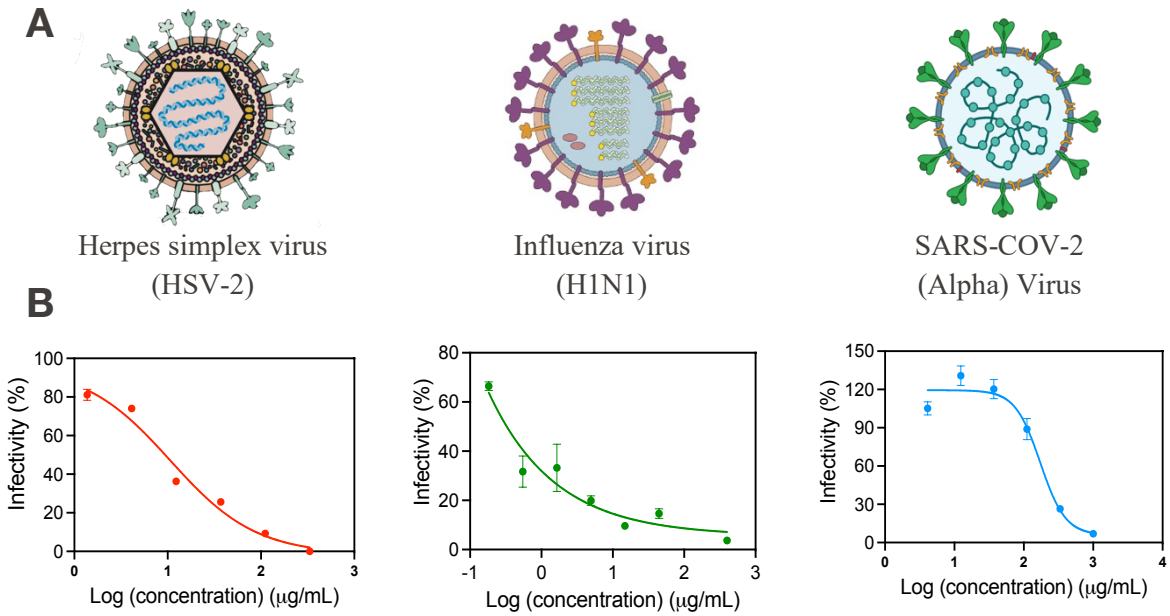

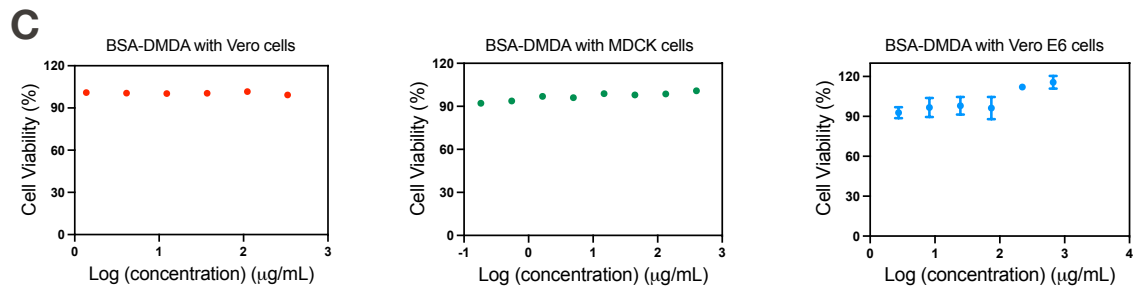

Figure 3.8. Broad-spectrum antiviral inhibition effect of modified protein BSA-DMDA against HSV-2, Influenza H1N1, and SARS-CoV-2.

A) Schematic structures of virus HSV-2, Influenza H1N1, and SARS-CoV-2. B) Dose-response antiviral inhibition effect of BSA-DMDA against virus HSV-2, Influenza H1N1, and SARS-CoV-2. C) Cytotoxicity effect of material BSA-DMDA in the same concentration range of dose-response antiviral inhibition against HSV-2 on Vero cells, against Influenza H1N1 on MDCK cells, and against SARS-CoV-2 on Vero E6 cells.

Modified protein BSA-DMDA showed anti-HSV-2 inhibition with EC_{50} equals to 10.66 μg/mL (0.149 μM), anti-Influenza H1N1 inhibition with EC_{50} equals to 0.32 μg/mL (4.48 nM), and anti-SARS-CoV-2 inhibition with EC_{50} equals to 172.7 μg/mL (2.42 μM) (Figure 3.8B). Cytotoxicity assay of material BSA-DMDA on different cell lines according to different viruses' infection were performed and results were displayed in Figure 3.8C. In the same testing concentration range as dose-response antiviral assay, modified protein BSA-DMDA displayed all over 95% cell viability on Vero cells, MDCK cells, and Vero E6 cells, which indicates the safety of this modified protein on hosting cells while keeping effective antiviral inhibitions.

We believe the non-specific broad-spectrum antiviral inhibition effect is mainly due to the ionic interaction and hydrophobic interaction between virus capsid membrane and ligands on modified protein. Positively charged modified protein first was attracted by negatively charged virus capsid membrane to the virus surface through ionic interaction, then long hydrophobic ligands on the surface of the protein applied to interfere force with spike protein or capsid membrane through hydrophobic interaction to inhibit or further deactivate viruses irreversibly.

3.6 Conclusion

In summary, we have demonstrated protein-based antivirals as a non-toxic, facile, broad-spectrum effective, and versatile platform for the potentially translatable antiviral solution. By simple one-step chemical functionalization under room temperature, modified proteins with high reproducibility showed not only effective antiviral inhibition but also a good virucidal effect. Two important key factors, ligand density, and hydrophobic force, significantly influenced antiviral inhibition and virucidal effect. Broad-spectrum antiviral inhibition against HSV-2, Influenza H1N1, and SARS-CoV-2 was well observed. Besides, this novel versatile platform uses natural protein as a core base, it is biocompatible, and the protein itself can be inert or functional, i.e., enzymes or therapeutical antibodies, which will add additional value for synergistic combinational therapy.

While we used model non-functional protein cores in this initial demonstration, further studies will investigate functional, active, and potentially targeting cores, including antiviral monoclonal antibodies. Additionally, non-specific interaction with high concentration of proteins in 100% plasma of this protein-based antivirals on viral inhibition effect will be further studied. Other ligands with a range of physicochemical properties (e.g., charge and hydrophobicity) will be further investigated; the aim is to open the door to virus-targeted virucidal materials.

3.7 Materials, Instruments, and Methods

Materials

Protein BSA and Cytochrome C were purchased from Sigma Aldrich (Missouri, United States). Protein Avidin is from Santa Cruz Biotechnology (Texas, United States). Chemicals 1-Ethyl-3-(3-dimethylaminopropyl) carbodiimide hydrochloride (EDC), N, N′-Dimethyl-1,3- propane diamine (DMPA), N, N′-Dimethyl-1,6-hexane diamine (DMHA), N, N'-Dimethyldodecane-1,12-diamine (DMDA), Avicel, 4% PFA solution, Tween 20, and 3,3'-diaminobenzidine (DAB) tablet were purchased from Sigma Aldrich (Missouri, United States). Methylcellulose was purchased from Fluka (St. Gallen, Switzerland), Crystal violet is from Acros (Geel, Belgium). Primary antibody (Influenza A antibody) was purchased from Light Diagnostics ((Missouri, United States). Secondary antibody (Anti-mouse IgG, HRP-linked antibody) were purchased from Cell Signaling Technology (Massachusetts, United States). Cell culture-related materials such as medium DMEM, fetal bovine serum (FBS), Penicillin-Streptomycin (10,000 U/mL), Trypsin-EDTA (0.25%), PBS pH 7.4 (1X) were purchased from Life Technology (California, United States). MTS cytotoxicity assay kit was purchased from Promega (Wisconsin, United States). Unless otherwise noted, all chemical and biological reagents were used as received. All solvents purchased were reagent grade.

Cell line

Vero cells (African green monkey fibroblastoid kidney cells) were purchased from ATCC (CCL-81) and cultured in DMEM, high glucose, GlutaMAX Supplement, pyruvate supplemented by fetal bovine serum (FBS, 10%), Penicillin (100 UmL^{-1}), Streptomycin (100 μgmL^{-1}). Cells were cultured in a humidified atmosphere with 5% of CO_2 at 37 °C.

MDCK (Madin-Darby Canine Kidney Cells) cell line, was purchased from ATCC (American Type Culture Collection, Rockville, MD). The cells were cultured in Dulbecco's modified Eagle's medium with glucose supplement (DMEM+ GlutaMAX™) containing 10% FBS and

Penicillin (100 UmL^{-1}), Streptomycin (100 μgmL^{-1}). MDCK cell lines was grown in humidified atmosphere with CO_2 (5%) at 37 °C.

Vero E6 (clone C1008) were purchased from ATCC (CRL-1586) and cultured in DMEM, high glucose, GlutaMAX Supplement, pyruvate supplemented by fetal bovine serum (FBS, 10%), Penicillin (100 UmL^{-1}), Streptomycin (100 μgmL^{-1}). Cells were cultured in a humidified atmosphere with 5% of CO_2 at 37 °C.

Virus Strains

Herpes Simplex Virus type 2 (HSV-2) was clinically isolated and provided by Prof. M. Pistello (University of Pisa, Italy). HSV-2 strains were propagated and titrated by plaque assay on Vero cells. Influenza H1N1 (Netherland/2009) was a kind gift from Prof M. Schmolke (University of Geneva). Influenza H1N1 strains were propagated and titrated by plaque assay on MDCK cells. SARS-CoV-2 (Switzerland/GE9586/2020) was isolated from a clinical specimen in University Hospital in Geneva in Vero E6 and passaged twice before the experiments.

Instruments

Matrix-assisted laser desorption/ionization time-of-flight mass spectra (MALDI-TOF-MS) were acquired on an Autoflex Speed (Bruker, Billerica, Massachusetts, USA). Functionalized protein nanoparticle size and surface zeta potential were characterized by dynamic light scattering (DLS) and Zeta Potential on Malvern NanoZS (Worcester, UK). MTS absorbance was measured with a microplate reader Tecan infinite 200Pro (Männedorf, Switzerland). Protein structure integrity was measured with circular dichroism spectrometer (CD) Chirascan V100 from Applied Photophysics (Leatherhead, UK). Analytical Ultracentrifugation (AUC) Beckman Optima XL-A, An-60 Ti rotor (California, United States)

Methods

Preparation of functionalized proteins

Three solutions were prepared separately first. Solution 1: proteins BSA or Avidin or Cytochrome C was dissolved in MES pH = 4.7 buffer (30 mg into 7.5 mL buffer with concentration 4 mg/mL) Solution 2: ligand such as DMPA or DMHA or DMDA were weighted 600 mg, and dissolved in 1-2 mL miliq water, adjust pH till to around 7.0 by adding 1M HCl, top-up the final volume into 15 mL with miliq water, final ligand concentration is 40 mg/mL. Solution 3: prepare EDC 300 mg dissolving in 7.5 mL MES pH = 4.7 buffer, the final concentration of EDC solution is 40 mg/mL. In this reaction, the mass ratio of protein, ligand, and EDC is fixed into Protein : Ligand : EDC = 1 : 20 : 10. Mix solution 1, 2, 3 together with magnetic stirring around 600 rpm overnight under room temperature. Purification of the final products was carried out by using an Amicon filter tube with molecular cutoff 30 KDa for BSA and Avidin protein and 10 KDa for Cytochrome C protein, miliq water was top-up to around 10 mL for washing at least 5 times with centrifugation under 5000 rpm speed for 5 mins.

Sample BSA-DMPA 20% and BSA-DMPA 10% nanoparticle synthesis keep the same amount of protein (Solution 1 the same), only decrease the input ligand density into above 20% (solution 2: ligand 8 mg/mL, 15 mL, pH adjusted into 7.0) and 10% (solution 2: ligand 4 mg/mL, 15 mL, pH adjusted into 7.0). EDC dose also decreased accordingly into above 20% (solution 3: EDC 8 mg/mL, 7.5 mL) and 10% (solution 3: EDC 4 mg/mL, 7.5 mL). Basically, sample BSA-DMPA 20% use fixed mass ratio of Protein : Ligand : EDC = 1 : 4 : 2, and sample BSA-DMPA 10% use fixed mass ratio of Protein : Ligand : EDC = 1 : 2 : 1.

Characterization of functionalized protein nanoparticles

DLS: All protein product solutions were in miliq water with a concentration of 1 mg/mL. Eppendorf disposable cuvette with absorbance range 220 - 1600 nm was used. 100 μL volume was put in the cuvette and measured by instrument Malvern NanoZS with condition manually scan for 10 runs under room temperature.

Zeta Potential: All protein product solutions were in miliq water with 1 mM KCl in concentration 1 mg/mL. Malvern disposable folded capillary cells DTS1070 were used for the measurement in instrument Malvern NanoZS.

Mass Spectrum: MALDI-TOF analyses were performed on an Autoflex Speed time-of-flight mass spectrometer (Bruker Daltonics, Bremen, Germany) equipped with a Bruker smartbeamTM-II laser (355 nm wavelength) and operated in the linear positive mode. Ion source 1 was set to 19.6 kV, ion source 2 was set to 17.5kV, Pulsed Ion Extraction was set to 28 kDa, and the mass range for detection was set from 30 to 100 kDa. Spectra were acquired using flexControl version 3.4. The three-layer method was used to spot the samples. Briefly, 1 µL of sinapinic acid (SA, Merck) matrix solution at 20 mg/mL in acetone was deposited on each spot of an MTP 384 ground steel BC target plate (Bruker, DE) and allowed to dry again at room temperature, forming a very thin first layer of matrix. The sample was centrifuged at 10000 × g for 2 minutes, and 1 µL of the supernatant was spotted on the target and allowed to dry at room temperature. After drying, 1 µL of SA matrix solution at 10 mg/mL in acetonitrile 50%, water 47.5%, and trifluoracetic acid 0.1% was applied to each spot and allowed to dry again at room temperature. Each spectrum was collected as a minimum of 2000 shots. For each measurement, the spectra were manually processed using flexAnalysis 3.4 Compass 1.4 (Bruker Daltonics, DE). For calibration, 0.5 L of Bruker Protein Standard II was deposited using the same method as the supernatant.

Circular dichroism for secondary structure characterization:

CD spectroscopy was used to analyze the effect of the cationization process on protein secondary structure. BSA has a primarily alpha-helical structure, where the CD spectrum has negative bands at 222 nm and 208 nm and a positive band at 196 nm. The secondary structure of BSA does not change significantly upon cationization, exhibiting a minimal increase in beta-sheet content and a concomitant decrease in alpha-helical content. CD experiments were performed on an Applied Photophysics Chirascan V100 Spectropolarimeter with quartz cells (l = 0.1 cm). Spectra were obtained from aqueous solutions (0.1 – 0.2 mg ml 1 in 50 mM phosphate buffer), and data were collected with 1 nm steps between 260 – 180 nm and 2 second integration time per step. A minimum of three spectra was recorded for static scans at 25 °C.

AUC: AUC was performed using a Beckman Optima XL-A, An-60 Ti rotor. All sample solutions were prepared freshly in PBS buffer to obtain final solutions that had 0.5~1.0 OD (optical

density) absorbance at 280 nm in AUC cells (double sector titanium centerpieces with quartz windows; the optical path length is 1.2 cm). All measurements were made at 20 ℃, 50,000 rpm. (with a radial step size of 0.003 cm) with sufficient duration to ensure complete sedimentation. Data ranges from 50-100 scans were chosen to represent the whole transporting process.

Dose-response Inhibition Assay again HSV-2

The effect of ligand functionalized proteins on HSV-2 infection was evaluated by a dose-response plaque reduction assay. Vero cells were plated in a 24-well plate around 24 hours in advance with a cell seeding density of 10^5 cells/well. Protein nanoparticle materials were prepared into 1 mg/mL concentration in miliq water. Six of 1.5 mL Eppendorf tubes were prepared for each protein nanoparticle sample with 500 uL DMEM containing 2% FBS filled inside. Take 250 μL of 1 mg/mL sample and add into the first tube, mix well with 500 μL DMEM medium, then take another 250 μL out from the first tube and transfer into the next one, 1 : 3 serial dilutions were performed like this until reaching the last tube. In the last tube after mixing, 250 μL volume was taken out and disposed of in order to keep every tube volume constant before incubation with viruses. HSV-2 virus titer of 40000 pfu/mL was first diluted 5 times with DMEM medium with 2% FBS into 8000 pfu/mL, then took 10 μL adding into each tube contain a different concentration of materials, mix well and incubated at 37 °C for 1 hour. Vero cells culture medium was aspirated and added virus-material mixture after incubation for each well 200 μL, and put it for incubation at 37 °C for 1 hour. Following virus adsorption, the virus inoculum was removed, and cells were washed with a medium, then overlaid with 500 μL medium containing 1.2 % methylcellulose, after incubation at 37 °C in the cell culture incubator overnight, methylcellulose containing medium was removed, and cells were fixed and stained with 300 μL 0.1 % of crystal violet in 20% ethanol for 15 mins, following by washing with PBS 7.4 (1X) twice and drying the well. Viral plaques were counted. The concentration producing 50% reduction in plaque formation (EC_{50}) was determined using Prism software dose-response EC_{50} non-linear fitting by comparing drug-treated and untreated wells.

Dose-response Inhibition Assay again Influenza H1N1

MDCK cells were pre-plated 24 h in advance in 96-well plates. Serial dilutions of BSA-DMDA were prepared in DMEM with 2% FBS and 1% P/S and incubated with the influenza virus (Influenza A/Netherlands/2009 (H1N1), MOI=0.1) at 37 °C for one hour, and then the mixtures were added to cells. Following the virus adsorption (1 h at 37 °C), the virus inoculum was removed, the cells were washed, and the fresh medium was added. After 24 h of incubation at 37°C, the infection was analyzed with an immunocytochemical (ICC) assay. The cells were fixed and permeabilized with methanol. Then the Flu A monoclonal antibody (1:100 dilution) was added and incubated for 1 hour at 37°C. The cells were washed with wash buffer (PBS + Tween 0.05%) three times; then anti-mouse lgG, HRP-linked antibody (1:500 dilution) was added. After 1 hour, the cells were washed, and the DAB solution was added. Infected cells were counted, and percentages of infection were calculated by comparing the number of infected cells in treated and untreated conditions.

Dose-response Inhibition Assay again SARS-CoV-2

This assay was performed by our collaborator Valeria Cagno Group (UNIL, Switzerland)

The effect of ligand functionalized protein BSA-DMDA against SARS-CoV-2 infection was evaluated by a dose-response plaque reduction assay. Vero E6 cells were plated in a 24-well plate around 24 hours in advance with a cell seeding density of 10^5 cells/well. Modified protein materials were prepared into 3 mg/mL concentration in miliq water. Six of 1.5 mL Eppendorf tubes were prepared for each protein nanoparticle sample with 500 uL DMEM containing 2% FBS filled inside. Take 250 μL of 3 mg/mL sample and add into the first tube, mix well with 500 μL DMEM medium, then take another 250 μL out from the first tube and transfer into the next one, 1 : 3 serial dilutions were performed like this until reaching the last tube. In the last tube after mixing, 250 μL volume was taken out and disposed of in order to keep every tube volume constant before incubation with viruses. SARS-CoV-2 virus titer of 40000 pfu/mL was first diluted 5 times with DMEM medium with 2% FBS into 8000 pfu/mL, then took 10 μL adding into each tube contain a different concentration of materials, mix well and incubated at 37 °C for 1 hour. Vero E6 cells culture medium was aspirated and added virus-material mixture after incubation for each well 200 μL, and put it for incubation at 37 °C for 1 hour. Following virus adsorption, the virus inoculum was removed, and cells were washed with a medium, then overlaid with 500 μL of 0.4% Avicel with DMEM 2% FBS. After incubation at 37 °C in the cell culture incubator for 48 hours, the medium was removed, and cells were fixed with 4%

formaldehyde and stained with 300 μL 0.1 % of crystal violet in 20% ethanol for 15 mins, followed by washing with PBS 7.4 (1X) twice and drying the well. Viral plaques were counted. The concentration producing 50% reduction in plaque formation (EC_{50}) was determined using Prism software dose-response EC_{50} non-linear fitting by comparing drug-treated and untreated wells.

Evaluation of virucidal activity against HSV-2

Vero cells were plated around 24 hours in advance with a seeding density of $2*10^4$/well in a 96-well plate. HSV-2 virus with titer 10^6 pfu/mL was used in this assay. Functionalized protein nanoparticles were prepared with concentration 300 μg/mL in 100 μL DMEM medium containing 2% FBS. 20 μL of titer 10^6 pfu/mL HSV-2 viruses were added into 100 μL materials, mix well and incubate at 37 °C for 1 hour. 96-well plate cell medium was first replaced with DMEM 2% FBS of 100 μL each well. Three 1.5 mL Eppendorf tubes were prepared with 450 μL DMEM 2% FBS filled inside, take 50 μL of the virus-material mixture after incubation and added into the first tube, mix well, then take another 50 μL from the first tube and transfer into the second one to make 1 : 10 serial dilutions like this was performed till the last tube. Three dilutions were prepared 1 : 10, 1 : 100, and 1 : 1000. Then take 50 μL of 1 : 10 dilution virus-material mixture added into first-row number 1 and 2 wells, another 50 μL of 1 : 100 dilution into first-row number 3 and 4, 50 μL of 1 : 1000 dilution into number 5 and 6, after that, using multichannel pipette taking 50 μL from the first row and adding into the second one, mix well, then 50 μL from second to third one until the seventh one for 1 : 3 serial dilutions and in the last row, adding virus-material mixture before any dilution 50 μL into first well, then 1 : 3 serial dilution till well number 6. After all these serial dilutions, incubate them at 37 °C for 1 hour. Following virus adsorption, the virus inoculum was removed, and cells were washed with medium, then overlaid with 100 μL medium containing 1.2 % methylcellulose, after incubation at 37 °C in the cell culture incubator overnight, methylcellulose containing medium were removed, and cells were fixed and stained with 50 μL 0.1 % of crystal violet in 20% ethanol for 15 mins, following by washing with PBS 7.4 (1X) twice and dry the well. Viral plaques were counted. Virus titers were calculated at dilutions at which the materials were not effective.

Cytotoxicity Assay

Functionalized proteins cell cytotoxicity was evaluated on Vero cells, MDCK cells, and Vero E6 cells with an MTS kit. All three types of cells were plated around 24 hours in advance in a 96-well plate with seeding density $2*10^4$/well in DMEM medium containing 2% FBS. Materials were serial diluted with DMEM medium containing 2% FBS according to dose-response antiviral assay dilution factor, each diluted sample final volume was kept into 200 μL. Replace the original cell culture medium with material containing medium 200 μL each well and incubate at 37 °C in the cell culture incubator for 24 hours. After that, the material containing medium was removed, and cells were washed by PBS 7.4 (1X) twice, then adding MTS reagents 10 μL + 90 μL DMEM serum-free medium into each well incubate them at 37 °C for 4 hours. After incubation, absorbance at 490 nm was measured with microplate reader Tecan. Cell viability ratio was calculated compared to non-material treated cells.

Statistical analysis.

Statistical analysis was performed using GraphPad Prism 9 (GraphPad Software, Inc., La Jolla, CA, USA). Unless otherwise noted, the data are presented as Mean ± SEM. Comparisons of two groups were performed by using a two-tailed unpaired Student's t-test. Comparisons of multiple groups at a single time point were performed by using one-way analysis of variance (ANOVA). P values were presented as *P < 0.05; ** P < 0.01; *** P < 0.001; **** P < 0.0001.

Safety consideration

All the HSV-2 virus-related and Influenza H1N1 virus-related assays were performed in the biological safety level (BSL)-2 lab. All the SARS-CoV-2 virus-related assays were performed in the biological safety level (BSL)-3 lab. Personal protective equipment (PPE) is worn, all procedures that can cause infection from aerosols or splashes are performed within a biological safety cabinet (BSC). An autoclave or an alternative method of decontamination is available for proper disposal. No unexpected or unusually high safety hazards were encountered.

Chapter 4 Lipoprotein-Cholesterol-based nanoparticles for Cancer Diagnosis

Cancer is termed as a group of diseases that can start in almost any organ or tissue of the body involving abnormal cell growth with the potential to invade or spread to adjoining parts of the body. Other terms used are malignant tumors and neoplasms. Cancer is the second leading cause of death worldwide, with more than 100 types of cancers and nearly 10 million deaths reported due to it in 2020.[163] It becomes a tremendous burden on society medical costs, not to mention there is huge pain impact on patients and their families.

Cancer survival is mainly due to a combination of diagnosis stage and access to prompt and effective care. Early cancer diagnosis and screening are essential for efficient control and response to treatment; it also can greatly increase the survival rate, decrease morbidity and medical cost of treatment. Cancer biomarker is a substance that can be found in tumor tissues, tumor cells, body fluids such as blood, urine, mucus, etc.; it includes a wide range of molecules like genomes circulating tumor DNA (ctDNA), mRNA, miRNA, proteins like tumor cell receptors, enzymes, metabolites, etc..[164] Cancer biomarkers are usually used for early cancer diagnosis and tracking, as they are either produced by tumor or by body system in response to the tumor. They are indicators for the evaluation of pathogenic processes and normal biological processes.[165] Precise cancer biomarker detection is critical for accurate clinical assessments, evaluation disease stages, and selection of optimal therapeutic interventions.[166–170]

At least five types of cancer biomarkers in clinical oncology have been summarized based on the medical intervene purpose: 1) Risk biomarkers indicating the likelihood of developing cancer; 2) Diagnosis biomarkers for distinguishing cancer or not; 3) Prognostic biomarkers evaluation of cancer stages; 4) Predictive biomarkers to monitor the effectiveness of treatment; 5) Target biomarkers for identifying the molecular targets of novel therapies.[171,172] Cancer biomarkers can be measured by various ways such as genetics, proteomics, or cellular molecular substances in higher than normal amounts in body fluids like blood, urine, and solid tumor tissues in a cancer patient. It usually requires researchers a thorough understanding of

the molecular mechanism, signal pathway, and cellular processes underlying cancer development based on only a few proteins and genes.

Cancer biomarker discovery can be accessed as big as cells, especially in the late stages of cancer, cancer cells appear in the bloodstream. Besides, cancer is also being classified as one type of metabolic disease; thus, glucose consumption compared to normal biological processes tends to become an important biomarker for cancer diagnosis, prognosis, and prediction of medical treatment.[173] Mitochondrial DNA (mtDNA) mutations can also provide valuable information about cancer presence as a molecular biomarker.[174–176] Furthermore, altered protein status can be taken as cancer biomarkers for cancer diagnostic, prognostic and therapeutic treatment monitor. For instance, uncontrolled cell proliferation activated by mammalian target of rapamycin (mTOR), through assessing the phosphorylated form of the ribosomal protein S6 and proliferation marker Ki-67, information about cancer stages can be achieved.[177,178] Tyrosine kinases as a class of enzymes to control cell growth, differentiation, and death are another type of indicator of tumor production and progression. Tyrosine kinase receptors like EGFR and HER2 have been identified as important targets of cancer treatment.[179] Downregulated cell death contributed by aberrance of telomerase. As telomerase is present in almost 90% of human cancers, it ensures telomere maintenance to protect cells from degradation and death, and it's responsible for the irreversible growth of cancer cells.[180] Other protein-based cancer biomarkers include viral proteins or antibodies against viral proteins for viral-induced cancers such as hepatocellular carcinoma (HCC) caused by hepatitis B virus (HBV) and cervical cancer caused by human papillomavirus (HPV),[181,182] tumors associated antigen (TAA) proteins released by cancer cells and their autoantibodies that target TAAs as the development of these antibodies is a result of cancer immunosurveillance.[183] All these protein cancer biomarkers potentially act as early reporters in tumorigenesis of aberrant cellular processes.

Another big group of cancer biomarkers is altered gene expressions. Genetic gene alterations such as oncogenes or tumor suppressors,[184] epigenetic modifications through DNA methylation are being used for the detection of both occurrence and prognosis of cancers.[185] Somatic mutations like structural and numerical aberrations in chromosomes also promise cancer biomarkers as the genetic events associated with tumor malignant transformation are being captured.[186–188] A typical example is the p53 gene; as one of the tumor suppressor genes, it delays cell cycle progression of proliferation, prevents unrolled multiplication of abnormal cells. Due to its central role in the control of cell growth and apoptosis and its frequent mutation in

tumors, p53 becomes a not only important but also unique target biomarker for the prediction of various types of cancer and their treatment.[189,190]

As cancer biomarkers are important indicators for prediction, diagnosis, and also providing clinical treatment strategy, researchers spent a lot of time and effort on detecting it. Some cancer blood protein biomarkers are approved by the American Society of Clinical Oncology, but the number and their clinical use are still very limited.[191] The goal of cancer biomarkers is to develop precise, efficient, and affordable detection and monitoring strategies for cancer. In the last few decades, certain progress has been made; various promising detection methods have been developed in this field. Intracellular biomarkers like genetic or epigenetic molecules can be detected by polymerase chain reaction (PCR),[192–194] cancer cell surface receptors biomarker can use techniques such as enzyme-linked immunosorbent assay (ELISA),[195] electrophoreses,[196] colorimetric assays,[197] surface plasmon resonance (SPR),[198,199] surface enhanced Raman spectroscopy (SERS),[200] proteomic mass spectrum, etc.[171,201] Although some of the methods are robust and low cost, lack of accuracy and sensitivity is still a big problem. In addition, no cancer biomarker currently available can be taken as a "perfect" biomarker for prediction, diagnosis, and monitoring simultaneously; thus, new cancer biomarkers matching clinical relevance and application are still in high demand but at the same time challenging.

Correspondingly, multiple detection techniques based on optical microchips,[202] biosensors[203] and fluid sampling of biomarkers named "liquid biopsy"[204] were developed. They are convenient, cost-effective and non-invasive, and can detect a variety of components such as in blood, urine lipids, genomes, proteins, and macromolecules. Although these fluid-based cancer biomarker detections seem promising, their reliability is still a big challenge. Besides, assay sensitivity like binding efficiency between the probe and target molecule, anti-interference ability towards the nonspecific binding, and specificity of different types of cancers also needs to be improved, and the technique needs to be standardized.

Proteins are known as vital biomolecules for many aspects of life in living organisms. Protein substances produced by cancer cells or other organisms in response to cancer can be used for cancer diagnosis. Most protein biomarkers are in the biggest body fluid blood. Analysis of protein cancer biomarkers in blood, especially those with very low abundance, involves several big challenges. As proteins cannot be amplified like nucleic acids, the low abundant quantity of certain protein cancer biomarker detection requires high sensitivity and accuracy of the

technique. Besides, proteins are usually very sensitive and "picky" for the detection environment, such as temperature, pH, and ionic strength, which makes it more difficult in low concentrations. Furthermore, the biggest challenge is the direct tracking of traces of protein cancer biomarkers in crude biological samples like blood is hindered by the high background of other non-cancer-related proteins in high abundance. Thus, sensitivity and accuracy are the basic requirements for techniques development to analyze protein cancer biomarkers. On the other hand, with the rapid development of nanotechnology, nanostructures or hybrid nano/bio-structures were applied in order to amplify the cancer biomarker detection signals and to generate cost-effective with high accuracy detection strategy.[205]

Commonly used techniques for protein cancer biomarkers detection like ELISA traditionally use colorimetric or fluorescent readout signals; it converts enzyme-substrate interaction into a colored signal for quantifying its absorbance. Recently advanced ELISA referred to as "plasmonic ELISA," utilizing gold nanoparticles has been developed to allow patients to directly read protein antigen signals by naked eye.[206] Another enzyme-cascade-amplification system was also developed to enhance the performance of ELISA.[207] Another label-free detection method for protein biomarkers is using an electrochemical detection strategy; although it's cheap, easy to scale up, the challenge for this technique is the lack of sensitivity and specificity. A variety of electrochemical-based biosensors have been developed, and among them, electrochemical impedance spectroscopy (EIS) showed promising application due to its label-free, mediator-free advantages, but non-specific adsorption limits its application for measuring complex samples like blood.[207] L. Feng *et al*.[208] developed a strategy by using tween 20 to avoid non-specific binding and using a chemical named meso-tetra (4-carboxyphenyl)porphyrin (TCPP) functionalized graphene as electrode and hexapeptide P_0 (RWIMYF) as a probe for detection of cyclin A_2 -an indicator of many types of cancers such as liver, breast, lung, and lymphoma, etc.- providing a simple electrochemical technique for cancer biomarker detection. Other similar techniques like electrochemiluminescence (ECL) combined electrochemistry and chemiluminescence it has been widely used for biomolecules detection in clinical diagnosis due to their low background, high sensitivity, and convenience.

A big deal in the biosensor world is field effect transistors (FET) development. This technique allows not only label-free measurement but also supports non-destructive sampling and real-time detection.[209] Although these technique-based biosensors have a lot of advantages, the lack of specificity hampering them from detecting cancer biomarkers directly from physical

fluids, the challenge of the complexity of the media still remains. Luckily another technique, microfluidic-based point-of-care platforms were developed to address this disadvantage. It can be easily integrated with electronic micro-fabrications, which makes it possible to detect a wide range of proteins in small volume with quantitative, cost-effective, and high-throughput measurements.[210–213] Sensors by using optical techniques like light absorption or light scattering, fluorescent, and SPR strategies have been used for cancer biomarker diagnosis; the biggest advantage is the signal is straightforward, sometimes can be detected by naked eyes. Besides, they are usually rapid, and no need for washing steps. Typical examples are DNA-barcoding for cellular protein biomarker measurement,[214] multi-color Förster resonance energy transfer (FRET) biosensors for multiple tumor biomarkers detection even in a small volume of human serum samples.[215] In SPR detection, researchers also developed protein microarrays on plasmonic gold substrates to enable multiple protein analyses with a low detection limit. Lee *et al*. combined nano-plasmonic tumor exosomes with transmission SPR for label-free and high throughput quantifications.[216,217]

Mass spectrometry (MS) is a key technique for metabolic cancer biomarker studies in clinical, as it has high sensitivity, wide dynamic detection range, high resolution, and can analyze extremely complex biofluids. It's a reliable and reproducible quantitative analysis technique. For example, capillary electrophoresis-mass spectrometry (CE-MS) for a large number of samples in a single run; or liquid chromatography-mass spectrometry (LC-MS) especially tandem mass tag (TMT), -an isobaric chemical tag-, labeled LC-MS plays an important role in comparative proteomics in complex samples like blood.[218] A pipeline of biomarker discovery based on the aid of proteomics is shown in Figure 3.1.[171] As a single cancer biomarker, even an "ideal" one is tended to have high sensitivity for detection, but relatively low specificity for various cancer types, which will raise the risk of false-positive signals. It will then bring unnecessary and costly diagnostic procedures and psychological stress to potential non-cancer people. In order to decrease these false cancer signals phenomenon, one possible strategy is to evaluate a panel of cancer biomarkers that have already been established as important and necessary.

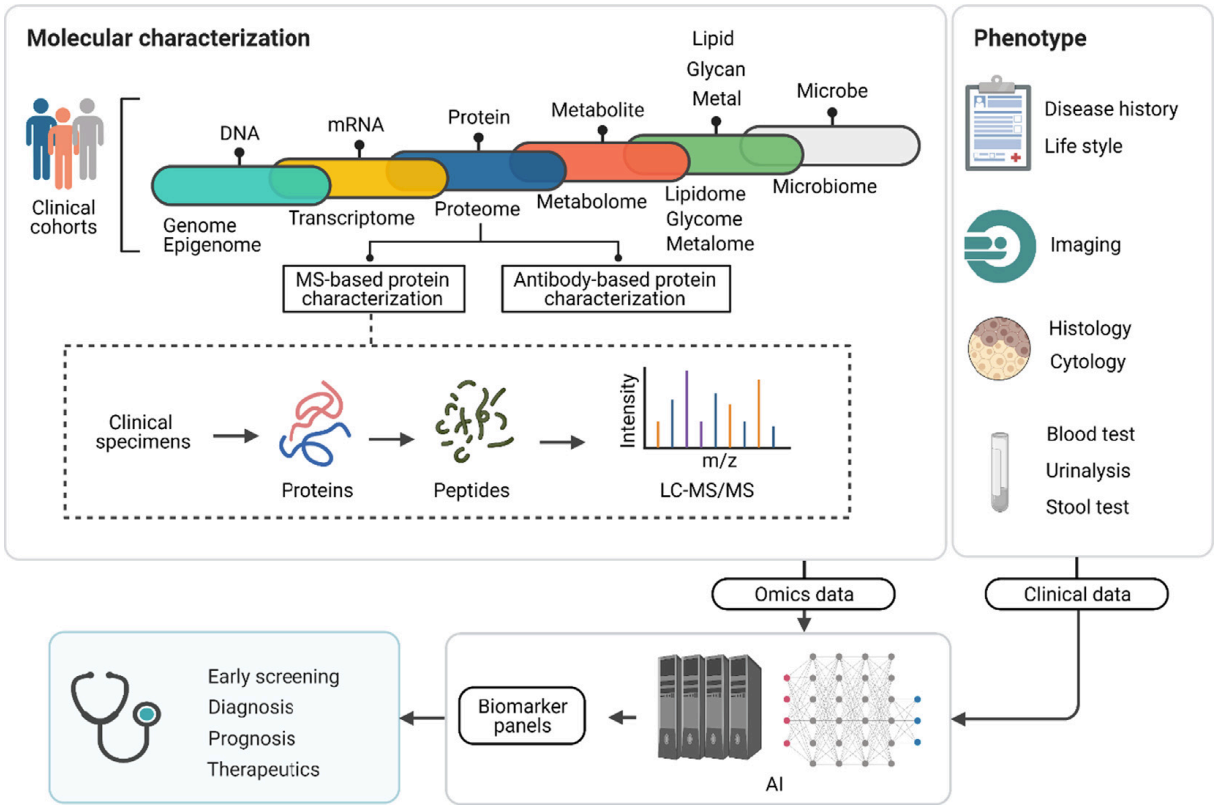

Figure 4.1. The pipeline of next-generation biomarker discovery aided with proteomics.[171]

As blood is the largest body fluid, blood-borne cancer biomarkers detection is in high expectation with reliability, high sensitivity, reproducibility, and accuracy techniques for early cancer diagnosis and prognosis. Blood can be taken by the routine clinical lab with a minimally invasive method, but tumor tissue releasing biomarkers into the bloodstream is usually in very low abundance. This natural phenomenon makes them difficult to be detected while other non-cancer-related proteins appear in much higher concentrations. Although a lot of efforts were made to improve proteomics-based cancer biomarker detection, a lot of challenges are still remaining. As directly analyzing component proteins in plasma and serum is extremely large dynamic protein concentration range, which might bring higher technical variation, not to mention that there is still big pathological heterogeneity from patient to patient. A proteomics-based biomarker is predominantly focused on identifying and profiling de-regulated proteins in the diseased patient sample compared to a healthy patient sample. However, when a diseased patient is symptomatic, the proportion of serum or plasma proteins may be up-regulated non-specifically, thus making the value of the markers compared to a healthy person sample not accurate. But if the tumor development before reaching to acute phase, the consistent protein

change over time is still representative and can add confidence to the cancer biomarker evaluation.

On the other hand, Isobaric tags introduced a different concept for protein/peptide quantification. With isobaric labeling of proteins in samples before analysis, a small mass difference will be introduced to identify the same peptides from two or more samples; thus, by tracing the measured peptide level, the protein levels are inferred from the evaluation of peptide ratios. The biggest isobaric labeling advantage is the ability to perform high-throughput quantification due to sample mixing; it dramatically decreases the sample analysis time and the variations between each experiment. Because when each sample is run separately, an ion selected for fragmentation on each LC-MS/MS run may not keep the same, thus these missing observations will potentially affect identification and quantification.[219] Besides, isobaric labeling exhibits a wide range in quantifying both high and low abundance proteins and proteins with different properties such as molecular weight, pI ranges, different categories, etc.[220] The labeling procedure is simple, efficient, and can apply to various samples, including cells, tissues, and even direct biofluids. Overall, the TMT labeling method improves overall signal-to-noise ratios, making MS data better quality even for a low abundance of proteins.

Another important method to increase the low abundant cancer biomarker protein signal is to accumulate these proteins. Nanomaterials have attracted a lot of interest due to their unique physicochemical properties. In the last decade, various investigations on spontaneous interaction between nanoparticles and plasma proteins were performed to understand the forming protein "corona" on the out shell of the nanoparticles.[221] And some researchers utilize this phenomenon for cancer biomarker detection.[222–224] Nanostructures here are used mainly to adsorb and accumulate flowing proteins in serum or plasma in order to amplify the protein detection signals. Although this strategy has its unique advantage, non-specific adsorption of the proteins, including serum albumin, cannot be avoided. Besides, it's invasive for further application to the clinical collection of blood samples.

Lipoproteins are substances made of proteins and fats that carry cholesterol through the bloodstream. It is a biochemical assembly with the primary function of transporting hydrophobic lipid molecules in blood plasma or other extracellular fluids. Extraction and characterization of serum lipoproteins can date to the 1950s, when ultracentrifugation was applied to separate nanoparticles in biofluids.[225–229] There are four different serum lipoprotein particles:

chylomicrons are the origin particles with a diameter range of 100-1000 nm, they are usually not detectable in the plasma because they quickly transfer into very-low-density lipoprotein (VLDL) with a diameter range of 30-90 nm then to low-density lipoprotein (LDL) with diameter range 20-25 nm, and high-density lipoprotein (HDL) with diameter range 10-20 nm. Compositional analysis of human serum lipoproteins was reported during the 1960s and 1970s about their density, proteins, phospholipids, triglycerides, cholesterol ester, and free cholesterol percentage in different types of serum lipoproteins.[230,231]

Extraction methods of serum lipoproteins were reported by using dextran sulfate-Mg^{2+} precipitation,[232–234] heparin-Mn^{2+} precipitation,[235–237] phosphotungstate-Mg^{2+} precipitation,[238,239] and polyethylene glycol (PEG)-6000 precipitation.[240–242] Characterization of these serum lipoproteins were shown by NMR spectroscopy,[243–245] X-ray small-angle scattering,[246,247] and Analytical Ultracentrifugation with Electron Microscopy.[227–229]

On the medical wise part, serum lipoproteins are known to be related to cardiovascular diseases.[248–252] LDL carries 3000 to 6000 fat molecules (phospholipids, cholesterol, triglycerides, etc.) around the body; it is referred to as "bad" lipoprotein because it correlates with atherosclerosis progression. On the contrary, HDL collects fat molecules from the body's cells or tissues and takes them back to the liver; it is referred to as "good" lipoprotein because it contributes to atherosclerosis regression. Chen *et al*. utilized this phenomenon to design HDL mimicking nanoparticles for atherosclerosis therapy.[253] Except for the correlation with atherosclerosis, serum lipoproteins were also reported having a correlation with hypertension,[254–256] diabetes mellitus,[257–260] overweight and obese,[261–263] Alzheimer's disease,[264,265] sepsis,[266–268] metabolic disorder,[269–272] and cancer.[273–277] There is ample evidence that many types of cancer cells indeed have unusually great LDL requirements because they require large amounts of cholesterol to make a new membrane. Cancer cells always utilize apoprotein B of LDL to bind to specific cell surface receptors, then allowing them uptake LDL by endocytosis and taken to lysosomes, where the cholesteryl esters are hydrolyzed, making free cholesterol available to the cell. Based on this phenomenon, researchers nowadays designed lipoprotein mimicking nanoparticles for improving cancer therapeutic targeting and cancer cell diagnostic imaging.[278–281]

Here in this work, we demonstrated a non-invasive serum lipoprotein-cholesterol nanoparticle-based cancer diagnosis system. Our hypothesis is based on since cancer is eventually a metabolic disorder disease and cancer cells/tissues have a high demand of uptake of LDL-

cholesterol for their own cell building blocks; thus, these LDL-lipoprotein-cholesterol nanoparticles might carry some cancer-related information or fingerprints. In recent years, using extracellular vesicles (EVs) derived from blood as a biomarker has gained widespread popularity.[282] However, EV is a minority population compared to other colloidal particles of the systemic circulation, namely the lipoproteins, which are known contaminants in EV isolation and carry biomarker molecules themselves. There are so many reported articles using EVs for cancer biomarker detection but with high background of lipoprotein-cholesterol, which we hypothesize might contribute to the signal of cancer due to their abundance. Another point we have noticed is that while researchers collect protein "corona" on the artificially injected nanoparticles in the blood for cancer biomarker detection, there is also a high possibility that the signal partly contributed from lipoprotein-cholesterol nanoparticles.

Based on the hypothesis above, we developed a high yield LDL-like lipoprotein-cholesterol extraction method by simply combining 50% w/v PEG10K precipitation, centrifugation, and purified through fast protein liquid chromatography (FPLC) size exclusion column (SEC) column directly from patients' serum after blood clotting. After protein digestion, TMT-labeling LC-MS/MS was performed to profile the protein contents for further analysis (Figure 4.2). In this preliminary test and as a proof of concept, 5 human patients with melanoma cancer (2 females age between 30 to 50 and 3 males age between 25 to 60) in clinical were collected blood 5 mL, their serum was extracted afterward. The control sample blood is from a commercial source, which is pooled of all healthy donors. After applying our lab-developed protocol to extract lipoprotein-cholesterol nanoparticles both from diseased serum and commercial healthy serum, proteomic analysis of all samples was carefully performed. Each sample protein was labeled isobaric tag on amino acid lysine, in total 10 samples (5 from cancer patients and 5 from different sources of healthy donors) were then mixed together and injected into LC-MS/MS for further proteomic analysis. Preliminary results showed within a false discovery rate less than 0.05, differentially expressed proteins either upregulated or downregulated proteins number is around 10 times compared to directly detect from serum itself (cancer diseased vs. healthy samples), which makes this detection system more sensitive and increase the accuracy of a cancer diagnosis.

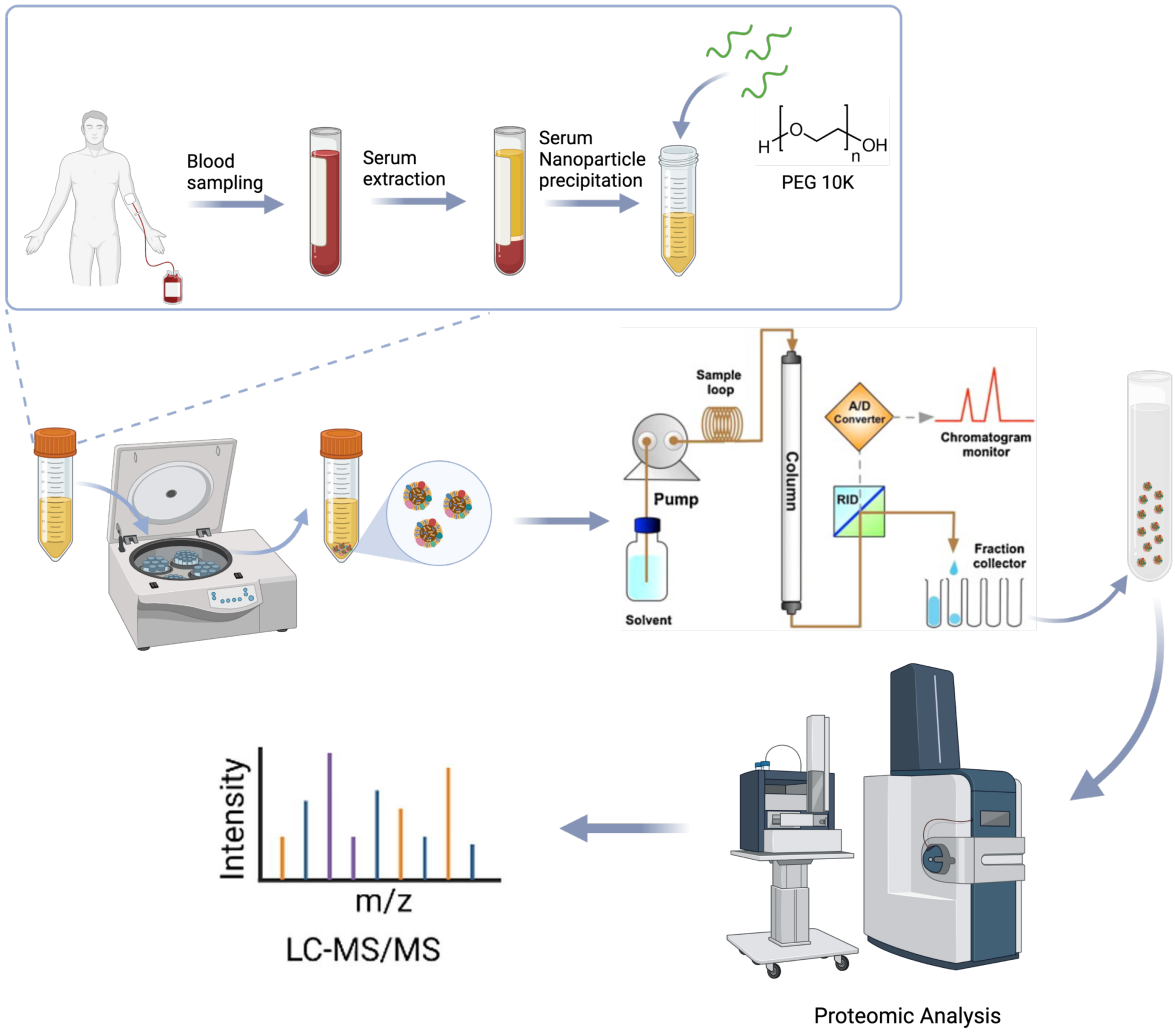

Figure 4.2. Schematic illustration of the lipoprotein-cholesterol nanoparticle extraction process and proteomic analysis

4.1 Lipoprotein-cholesterol nanoparticle extraction and characterization

As a preliminary test, five melanoma cancer patients' blood samples and five blood samples from pooled healthy donors were collected and clotted to get serum samples. Serum samples were first diluted with PBS 7.4 1X of 5 times and centrifuged with high speed to remove big aggregates. After that, 50% w/v PEG 10K was added into serum solution and left at 4 degrees for lipoprotein-cholesterol nanoparticles precipitating. Collected lipoprotein-cholesterol nanoparticles were injected into the fast protein liquid chromatography (FPLC) SEC column for further purification. Before using lipoprotein-cholesterol nanoparticles for proteomic analysis, lipoprotein-cholesterol nanoparticles were carefully characterized (Figure 4.3).

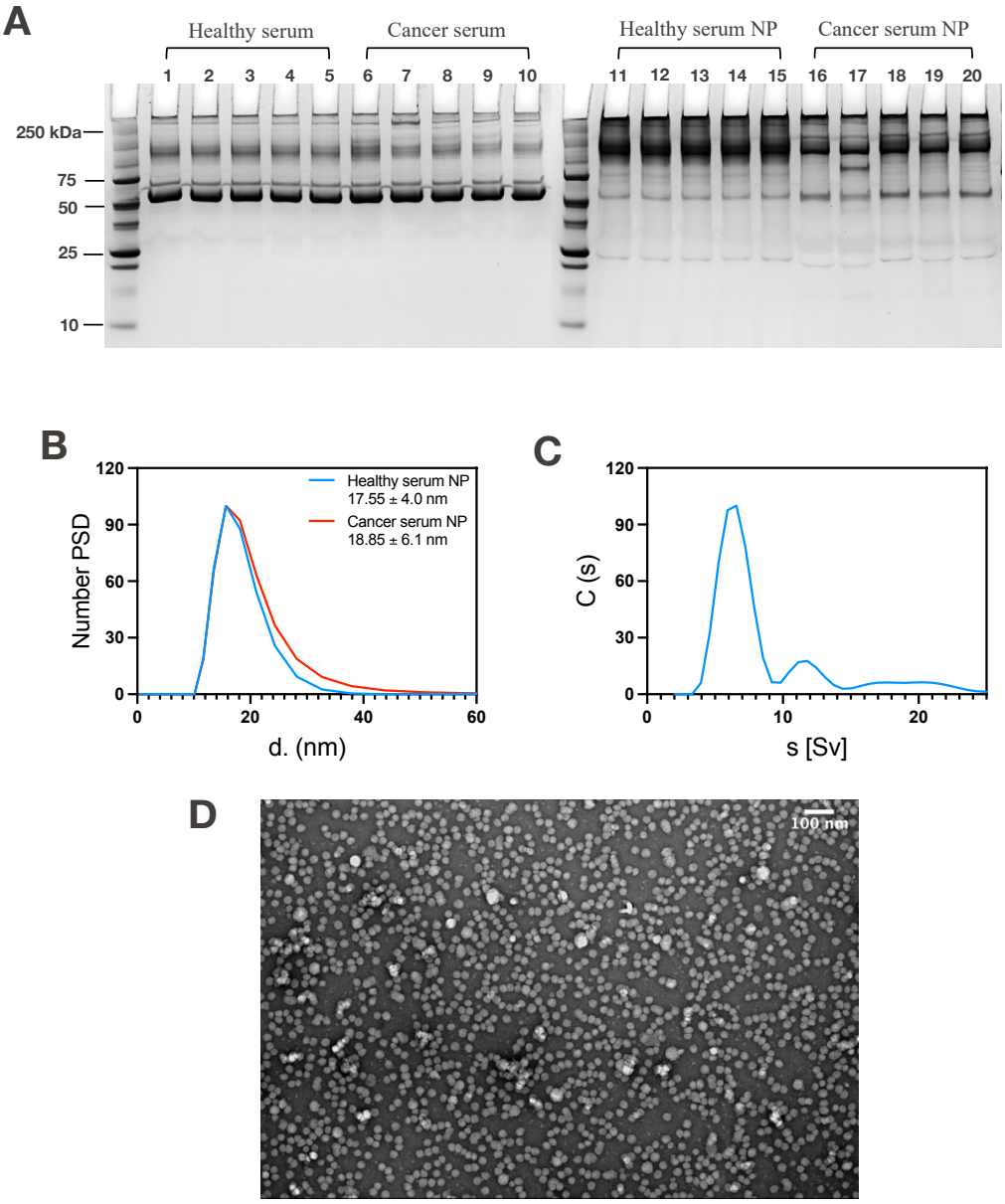

Figure 4.3. Characterization of extracted lipoprotein-cholesterol nanoparticles.

A) SDS-PAGE Gel of five healthy serum vs. five cancer serum (left) and five healthy lipoprotein-cholesterol nanoparticle samples vs. five cancer lipoprotein-cholesterol nanoparticle samples (right). B) DLS characterization of both healthy lipoprotein-cholesterol nanoparticles and cancer lipoprotein-cholesterol nanoparticles. C) AUC characterization of lipoprotein-cholesterol nanoparticles from healthy donors. D) Representative TEM image of lipoprotein-cholesterol nanoparticle from healthy donors, scale car: 100 nm.

From the SDS-PAGE gel (Figure 4.3A), serum from five melanoma cancer patients and serum from five pooled healthy donors showed similar protein migration pattern; the most abundant protein is the one between 50 kDa and 75 kDa, which as we suspect, is human serum albumin (HSA) with molecular weight around 67 kDa. While the lipoprotein-cholesterol

nanoparticles extracted both from healthy donors and cancer patients' serum showed different migration patterns compared to serum itself, the most abundant serum protein HSA was depleted dramatically. And except most proteins on the nanoparticles were stuck in the well, there are two major protein bands, one is at around 100 to 150 kDa, and the other one clearly showed at around 25 kDa, while at the same position, all serum samples didn't display this protein band at all. Thus, by extracting lipoprotein-cholesterol nanoparticles, we can not only deplete the most abundant inert protein HSA but also accumulate small molecular weight proteins, which will potentially increase the chance to detect cancer biomarkers.

Dynamic light scattering characterization of both healthy and cancer lipoprotein-cholesterol nanoparticles (Figure 4.3B) showed similar nanoparticle sizes around 17-19 nm. Furthermore, the AUC characterization of healthy lipoprotein-cholesterol nanoparticles (Figure 4.3C) displayed in total three peaks according to their different sedimentation time, the major one is the monomer nanoparticles, and the other two minor peaks might be due to the protein particles aggregate or extracellular vesicles. Because of the limited amount of cancer lipoprotein-cholesterol nanoparticles samples, we didn't perform the AUC characterization, but we expect it supposes to display a similar pattern as healthy lipoprotein-cholesterol nanoparticles. Figure 4.3D showed the visualization of the lipoprotein-cholesterol nanoparticle by a negative stained TEM image. From the image, we can see that these lipoprotein-cholesterol nanoparticles are pretty homogeneous with the size around 20 nm, which is consistent with the measurement of DLS, and the majority of the nanoparticles are monomers, which is also proved in the AUC characterization.

4.2 Proteomic analysis sample preparation--TMT labeling

Serum and lipoprotein-cholesterol nanoparticle proteins were digested by filter aided sample preparation (FASP) with minor modifications. After reducing with TCEP, proteins were digested with mass spectrometry grade trypsin and LysC. Isolated peptides were eluted sequentially with 4% TFA, desalted, and further dried. For TMT labeling, dried peptides were labeled using TMT 10-plex^{TM} Label Reagent following the manufacturer's instructions. Labeled peptides were mixed in 1 : 1 ratio, and 10 samples from each group (serum with serum and nanoparticles with nanoparticles) after labeling were combined separately and vortexed to thoroughly mix. The combined sample was fractionated in 12 fractions by isoelectric focusing, and

every fraction was analyzed by LC-MS/MS (Figure4.4). Detailed sample labeling with TMT in this work was shown in Table 4-1.

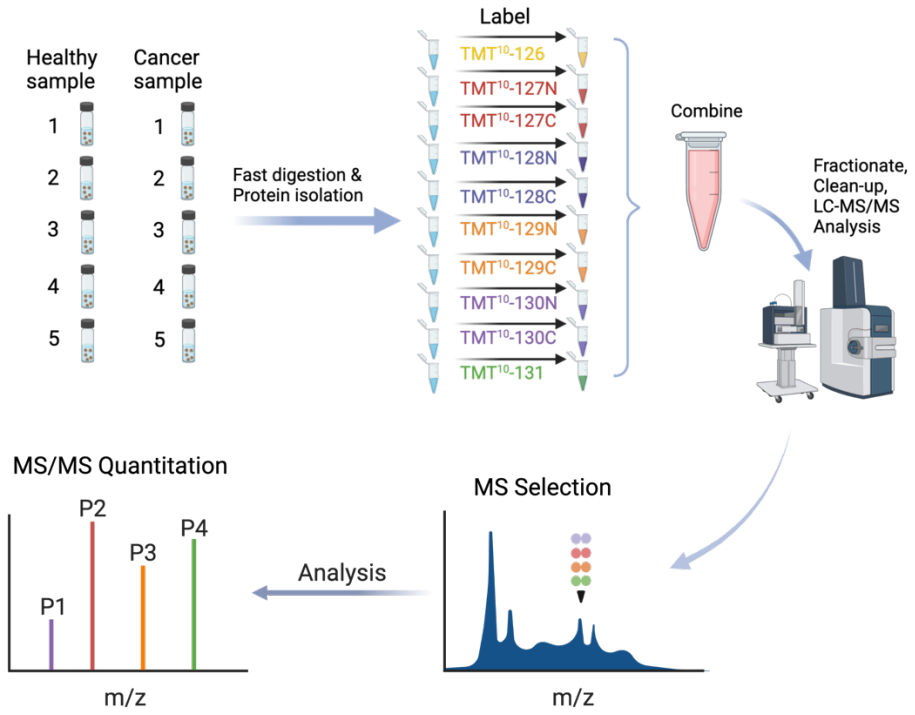

Figure 4.4. Schematic illustration of sample protein digestion and TMT labelling before proteomic analysis.

Table 4-1. Serum and lipoprotein-cholesterol nanoparticles labelled with TMT.

	TMT	Label	Serum	Serum nanoparticle
1	TMT10plex-Lys126C	126	Healthy 1	Healthy NP 1
2	TMT10plex-Lys127C	127C	Healthy 2	Healthy NP 2
3	TMT10plex-Lys127N	127N	Diseased 1	Diseased NP 1
4	TMT10plex-Lys128C	128C	Healthy 3	Healthy NP 3
5	TMT10plex-Lys128N	128N	Diseased 2	Diseased NP 2
6	TMT10plex-Lys129C	129C	Healthy 4	Healthy NP 4
7	TMT10plex-Lys129N	129N	Diseased 3	Diseased NP 3
8	TMT10plex-Lys130C	130C	Healthy 5	Healthy NP 5
9	TMT10plex-Lys130N	130N	Diseased 4	Diseased NP 4
10	TMT10plex-Lys131N	131	Diseased 5	Diseased NP 5

4.3 Quality control of serum and serum lipoprotein-cholesterol nanoparticles from healthy donors and cancer patients

Clinical characteristics of these 5 melanoma cancer patients include 2 females aged 39 and 44 and 3 males aged 28, 29, and 59. In the discovery proteomic analysis, raw data were processed using four search engines: SEQUEST, Mascot, MS Amanda, MS Fragger against the Uniprot Human database in the environment of Proteome Discoverer (PD) v.2.4. Only peptide-spectrum match (PSM) events with high confidence across the individual fractions and different search engines were considered and plotted. In serum samples from healthy donors and cancer patients, 636 proteins in common were identified, and in lipoprotein-cholesterol nanoparticle samples from healthy donors and cancer patients, 615 proteins in common were identified (Figure 4.5).

In order to reduce systematic biases and achieve a good downstream quantitative analysis, we performed a two-step normalization: sample loading normalization and trimmed M-Mean (TMM) normalization. The sample loading normalization step scales each TMT channel so that its sum of reporter ion signals equals the average grand total across samples. TMM normalization assumes that the samples mostly have a lot of common proteins that are not differentially expressed. High and low abundance proteins are removed, and larger and smaller fold-changes are also trimmed. Then, the remaining proteins should be similar in expression. TMM computes single global scaling factors that move those presumed unchanged proteins to more similar values. The TMM routine does include the equivalent of a sample loading normalization step.

After two-steps normalizations, principal component analysis (PCA) was performed to check the sample variations. It is a statistical procedure that uses an orthogonal transformation to convert a set of observations of possibly correlated variables - here, the intensities of the proteins - into a set of values of linearly uncorrelated variables called principal components. This transformation is defined in such a way that the first principal component has the largest possible variance (that is, accounts for as much of the variability in the data possible), and each succeeding component, in turn, has the highest variance possible under the constraint that it is orthogonal to the preceding components (= with the constraint that the correlation between the

succeeding component and the previous ones is 0). PCA is sensitive to the relative scaling of the original variables. Serum and lipoprotein-cholesterol nanoparticle samples PCA are shown in Figure 4.6.

In the serum sample, the principal component 1 -the intensity of the detected proteins- variation is 32.6%, from the healthy serum samples and cancer serum samples cannot be differentiated only by principal component 1, and principal component 2 -variation contribution 18%- needs to be introduced to see the variation in general between healthy and cancer serum. By contrast, in the lipoprotein-cholesterol nanoparticle samples, the principal component 1 of the protein intensity showed 53.4% variation contribution, and we can clearly see the differences between healthy lipoprotein-cholesterol nanoparticles and cancer lipoprotein-cholesterol nanoparticles. Principal component 2 variation within samples of cancer lipoprotein-cholesterol nanoparticles is mainly due to gender, age, or cancer stage differences, but this needs further confirmation with a large number of patients' samples.

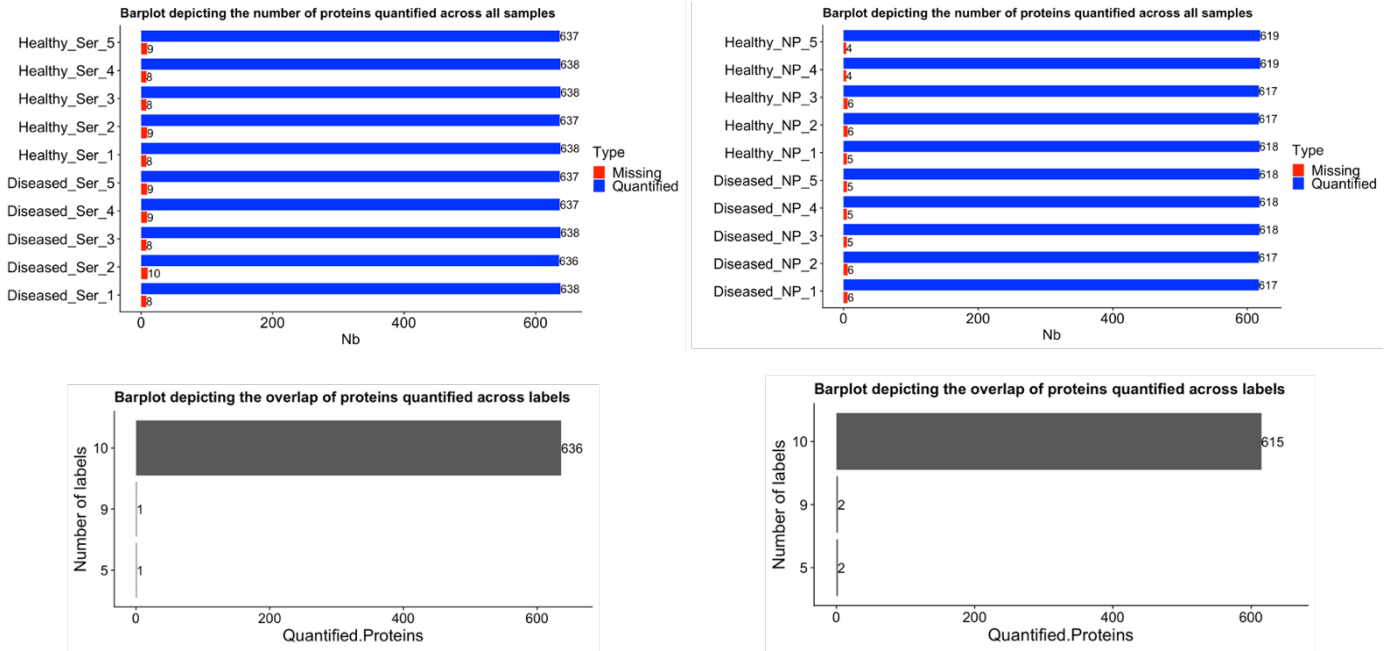

Figure 4.5. LC-MS/MS detected PSM proteins with high confidence in all four search engines of both samples from serum and lipoprotein-cholesterol nanoparticles.

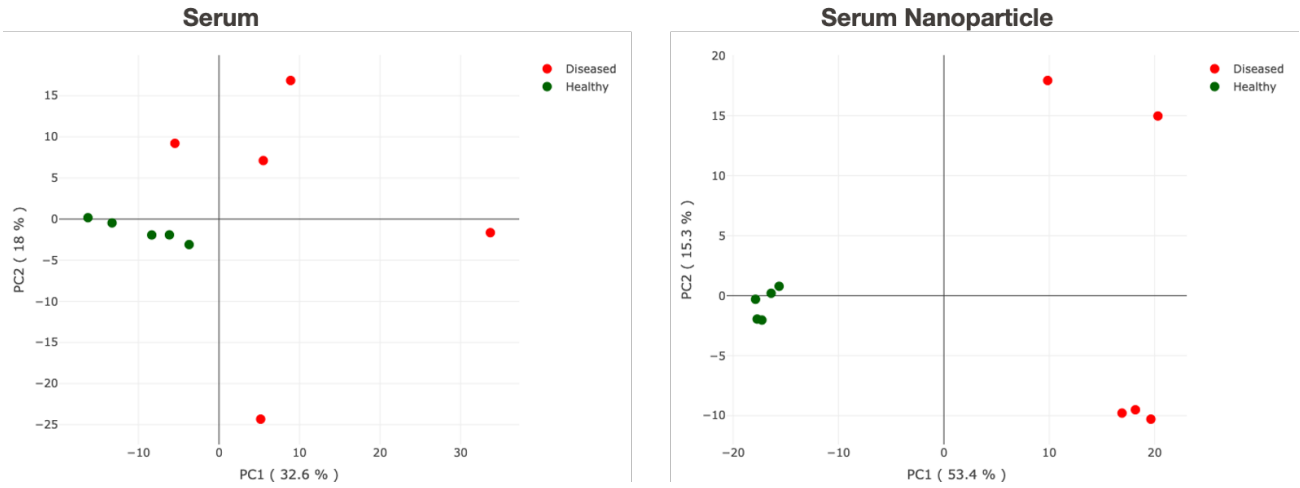

Figure 4.6. Principal components scatter plots display samples from serum and lipoprotein-cholesterol nanoparticles variations

4.4 Protein biomarker quantification from serum and lipoprotein-cholesterol nanoparticles

Among the 636 identified proteins in serum and 615 identified proteins in lipoprotein-cholesterol nanoparticles, significantly differentially expressed proteins (DEPs) were screened for fold change ≥ 2 or ≤ 0.5, and $P < 0.05$. There are 169 differentially expressed proteins in lipoprotein-cholesterol nanoparticle samples while comparing cancer diseased vs. healthy ones. In serum samples, we found only 18 differentially expressed proteins while comparing cancer diseased vs. healthy ones. Of these DEPs, the expression level of 83 proteins (49.1%) upregulated and 86 proteins (50.9%) downregulated in lipoprotein-cholesterol nanoparticles (cancer diseased vs. healthy), while in serum samples, the expression level of 10 proteins (55.6%) upregulated and 8 proteins (44.4%) downregulated. Differential protein expression analysis was performed using R Bioconductor package limma, followed by Benjamini-Hochberg multiple-testing correction method. The volcano plot combines a measure of statistical significance from a statistical test (in this case, adjusted p-value from LIMMA) with the magnitude of the fold-change, enabling quick visual identification of proteins displaying changes that are also statistically significant. It describes the distribution of all the identified proteins in serum and in lipoprotein-cholesterol nanoparticles based on the y-axis of the statistical significance $-\log_{10}$ (P) values and the x-axis of $\log_2$ (mean ratio fold-change) (Figure 4.7AB). Proteins that are

differentially abundant in one of the samples were shown either left or right of the x-axis origin. The cluster analysis for DEPs expression clearly displayed the differential expression pattern of serum samples from lipoprotein-cholesterol nanoparticle samples.

From Figure 4.7A, 596 proteins are not significantly different compared cancer diseased to healthy serum, only 21 proteins are upregulated, and 19 proteins are downregulated with false discovery rate (FDR) ≤ 0.05 (FDR is metric for global confidence assessment of large-scale proteomics dataset). Furthermore, if considering the fold-change comparison cancer diseased to healthy serum > 2 or <0.5, there are only 10 proteins (1.57% of total quantified proteins in serum) are upregulated, and 8 proteins (1.26% of total quantified proteins in serum) are downregulated (Table 4-2). From the right panel of Figure 4.7A, 10 most plasma abundant proteins identified are all proteins with FDR > 0.05, which indicates the confidence assessment is low. Although one possible cancer-related protein, FN1 is with FDR ≤ 0.05, the fold-change is less than 2.

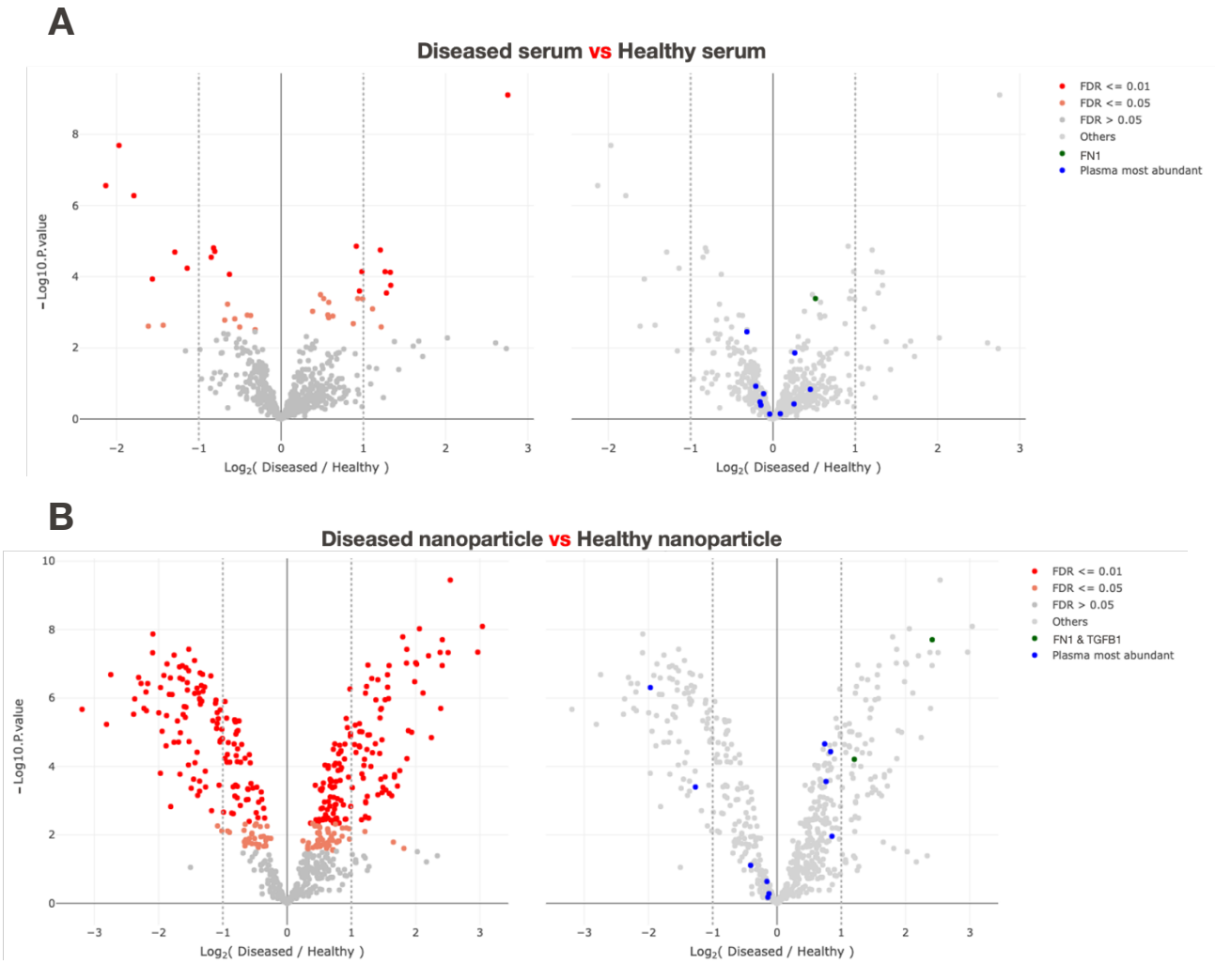

C

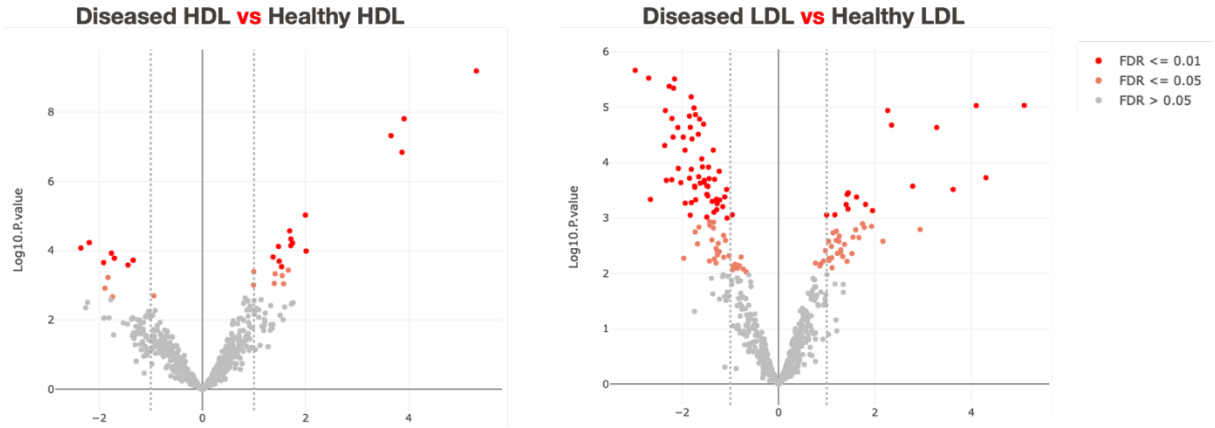

Figure 4.7. Volcano plot of sample from healthy and cancer diseased serum, lipoprotein-cholesterol nanoparticle, HDL, and LDL.

The volcano plot was drawn using two factors, and the x-axis represents the Log_2 (mean ratio fold-change) between two groups healthy samples and cancer diseased samples, the y-axis represents the p-value ($-Log_{10}$) obtained from the LIMMA test to show the significant difference between two groups cancer diseased vs. healthy samples. The orange dots in the figure are quantified proteins with FDR ≤ 0.05, and red dots are quantified proteins with FDR ≤ 0.01, and grey dots are quantified proteins with FDR > 0.05. The right panel of the x-axis from origin 0 represents proteins that are upregulated, and the left panel of the x-axis from origin 0 represents proteins that are downregulated. A) Volcano plot of sample from serum (cancer diseased vs. healthy serum); B) Volcano plot of sample from lipoprotein-cholesterol nanoparticles (cancer diseased vs. healthy nanoparticles); C) Volcano plot of sample extracted from commercial kit to get HDL and LDL (cancer diseased vs. healthy ones, respectively).

Table 4-2. Protein regulation of different samples from cancer diseased vs. healthy ones.

Protein regulation	Sample pairwise comparisons	Protein number (FDR ≤ 0.05)	Fold-change > 2 or < 0.5
Down	Diseased serum vs Healthy serum	19	8 (1.26%)
Up	Diseased serum vs Healthy serum	21	10 (1.57%)
Not Significant	Diseased serum vs Healthy serum	596	
Down	Diseased lipoprotein-cholesterol NP vs Healthy	161	86 (14%)
Up	Diseased lipoprotein-cholesterol NP vs Healthy	200	83 (13.5%)
Not Significant	Diseased lipoprotein-cholesterol NP vs Healthy	254	
Down	Diseased HDL vs Healthy HDL	11	10 (1.4%)
Up	Diseased HDL vs Healthy HDL	21	21 (3%)
Not Significant	Diseased HDL vs Healthy HDL	678	
Down	Diseased LDL vs Healthy LDL	93	81 (11.5%)
Up	Diseased LDL vs Healthy LDL	48	44 (6.3%)
Not Significant	Diseased LDL vs Healthy LDL	560	

Volcano plot of lipoprotein-cholesterol nanoparticle samples from cancer diseased patients' pair-compare with lipoprotein-cholesterol nanoparticle samples from healthy donors were displayed in Figure 4.7B. In total, 200 proteins were upregulated, and 161 proteins were downregulated with FDR ≤ 0.05, among them there are 83 proteins (13.5% of total quantified proteins in lipoprotein-cholesterol nanoparticle samples) upregulated and 86 proteins (14% of total quantified proteins in lipoprotein-cholesterol nanoparticle samples) downregulated (Table 4-2). In the right panel of Figure 4.7B, 10 plasma most abundant proteins and two possible cancer-related proteins FN1 and TGFB1 distribution were shown according to their fold-change and significant difference comparing cancer diseased with the healthy ones. There are 6 plasma most abundant proteins and 2 possible cancer-related proteins, FN1 and TGFB1, which have a significant difference, and among them, there are 2 plasma most abundant proteins and two possible cancer-related proteins with fold-change over 2.

In order to prove these lipoprotein-cholesterol nanoparticles were extracted from serum, not forming during the extraction with PEG. We used BSA instead of serum to perform the extraction and purification. SDS-PAGE was run to check the protein nanoparticle migration pattern (Figure 4.8). The same amount of protein containing fetal bovine serum (FBS) and BSA solution was used side by side to perform the extraction. FBS-PEG-1 and BSA-PEG-1 are samples from first-round precipitants after adding PEG 10K, and FBS-PEG-2 and BSA-PEG-2 are samples from second-round precipitants after adding PEG 10K. FBS NPs are samples further purified by the FPLC SEC column after the second round of precipitation. From the SDS-PAGE image, from the second round of precipitation, the sample extracted from FBS showed a clear protein band stuck in the PAGE well which could not migrate down in the gel due to large particle size; after FPLC purification, the nanoparticle protein band on the PAGE well is clearer. However, samples extracted from BSA solution, all proteins were migrated down just like native BSA protein; there is no nanoparticle forming during the PEG aided extraction process.

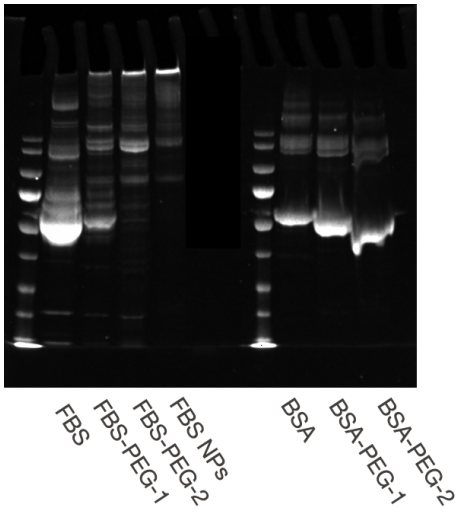

Figure 4.8. SDS-PAGE image of nanoparticles extracted from FBS and BSA with the same PEG precipitation method.

In order to evaluate our lab developed PEG10K extraction method efficiency, we compared it with a commercial kit to extract HDL and LDL and evaluate them by proteomic analysis. The same source of healthy donors and 5 melanoma cancer patients' serum were used for extraction of HDL and LDL by this commercial kit method, and proteomic analysis was also performed in the same setting as lipoprotein-cholesterol nanoparticles extracted with our lab-developed extraction method. From the result in figure 4.7C, there are in total 710 quantified proteins in HDL and 701 proteins quantified in LDL. Among HDL quantified proteins, only 21 proteins were upregulated, and 11 proteins were downregulated while comparing cancer diseased vs. healthy ones with FDR ≤ 0.05, and with fold-change > 2 or < 0.5, there are 21 proteins (3% of total quantified proteins in HDL) upregulated and 10 proteins (1.4% of total quantified proteins in HDL) downregulated. Among LDL quantified proteins, there are 48 proteins upregulated and 93 proteins downregulated while comparing cancer diseased vs. healthy ones with FDR ≤ 0.05, and with fold-change > 2 or < 0.5, there are only 44 (6.3 % of total quantified proteins in LDL) upregulated and 81 proteins (11.5% of total quantified proteins in LDL) downregulated. On the extraction yield wise, with a low quantity of serum (1 mL) and following the instruction of the extraction kit, the yield of LDL is very low; on average less than 20 ug LDL/mL serum can be obtained, and different individual serum obtained LDL is very heterogeneous. While using our lab-developed extraction method, from 1 mL each cancer individual serum, we could achieve on average 700 ug lipoprotein-cholesterol nanoparticles/mL serum, around 35 times higher than the commercial kit extraction. And from the proteomic analysis,

the number of differentiated proteins from lipoprotein-cholesterol nanoparticle samples is 361/615, while in LDL samples, the differentiated proteins are 142/701, which indicates the advantages in sensitivity and better accuracy.

4.5 Protein profiling--candidate protein biomarkers in melanoma cancer patient

The above results reveal differences in cancer patients and healthy people in their protein states, which prompted us to further investigate if the above variations in the abundance of plasma proteins can be used as protein biomarker fingerprints for cancer diagnostics. In order to identify these proteins, which were differentially abundant between melanoma cancer patients and healthy people, 5 individual replicates both on cancer patients and healthy donors were applied for lipoprotein-cholesterol nanoparticle extraction and proteomic analysis. Statistical analysis of raw LC-MS/MS data about the relative protein expression (fold-change), the statistical difference (LIMMA, *p-value*), and reliability of the measurement was calculated. Progenesis statistical analysis reveals there are 361 individual proteins differentially expressed over a total quantified 615 proteins in common in both melanoma cancer diseased and healthy lipoprotein-cholesterol nanoparticles; among them, there are 200 proteins upregulated and 161 proteins downregulated in cancer compared to healthy samples with FDR ≤ 0.05. While in the serum samples, there are only 40 individual proteins differentially expressed over total quantified 636 proteins in common in both melanoma cancer diseased and healthy ones, among them there are 21 proteins upregulated and 19 proteins downregulated in cancer compared to healthy samples with FDR ≤ 0.05. The Differentially expressed protein fold-change heat map was displayed in Figure 4.9. Furthermore, both top 30 upregulated and 30 downregulated proteins in lipoprotein-cholesterol nanoparticle samples were listed and sorted according to their fold-change comparing cancer diseased vs. healthy ones in Table 4-3 and Table 4-4. Overall, in this preliminary proteomic analysis of lipoprotein-cholesterol nanoparticles, the issue of serum albumin masking is eliminated, and the significant difference of differentially abundant proteins is increased.

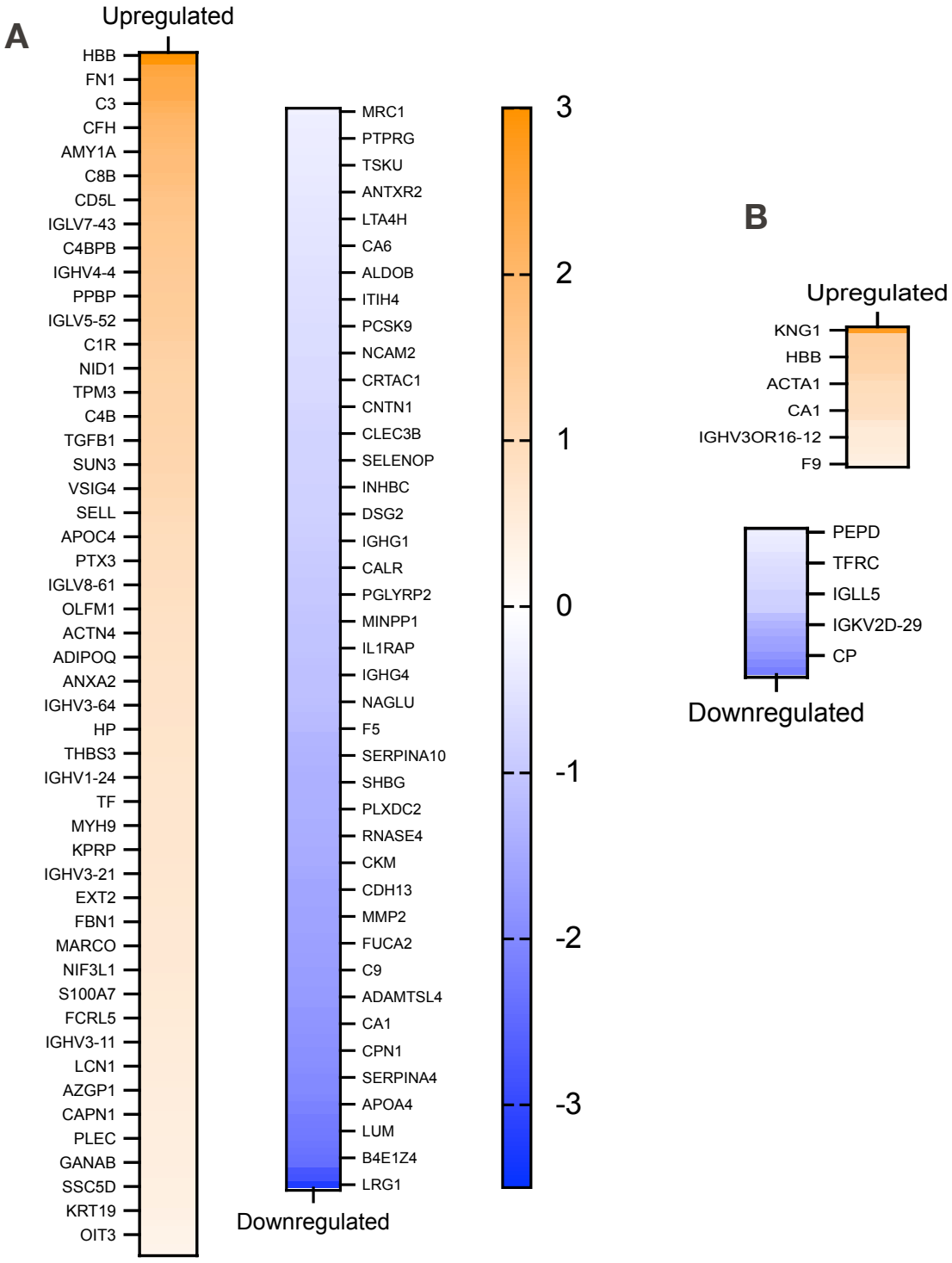

Figure 4.9. Heat map of differentially expressed individual proteins in lipoprotein-cholesterol nanoparticles and serum while comparing cancer diseased vs. healthy samples.

A) Differentially expressed proteins from lipoprotein-cholesterol nanoparticles; B) Differentially expressed proteins from serum samples. Every four proteins have one label, and the label name is each protein gene, scale bar: Log_2 (FC).

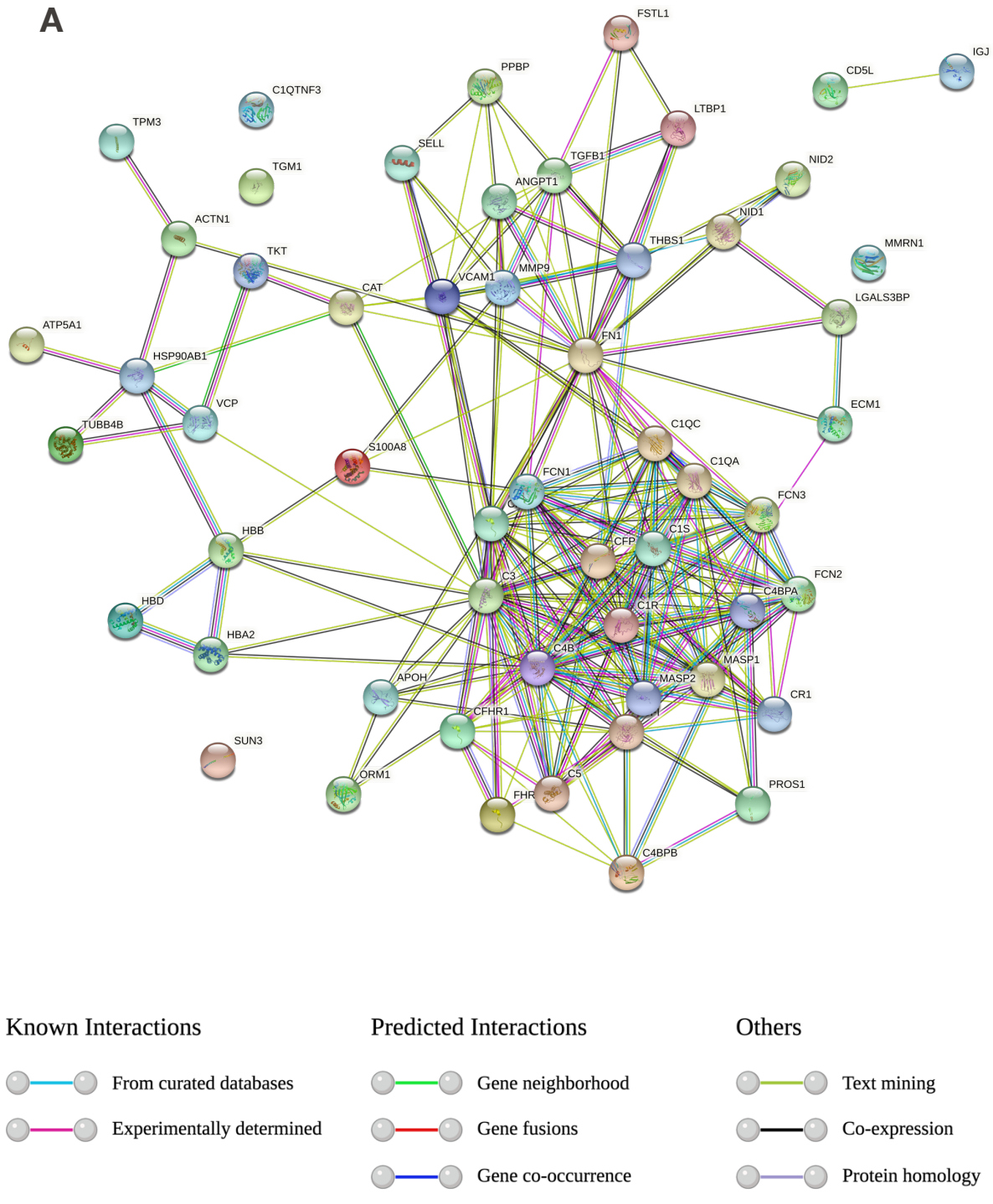

Known Interactions

From curated databases

Experimentally determined

Predicted Interactions

Gene neighborhood

Gene fusions

Gene co-occurrence

Others

Text mining

Co-expression

Protein homology

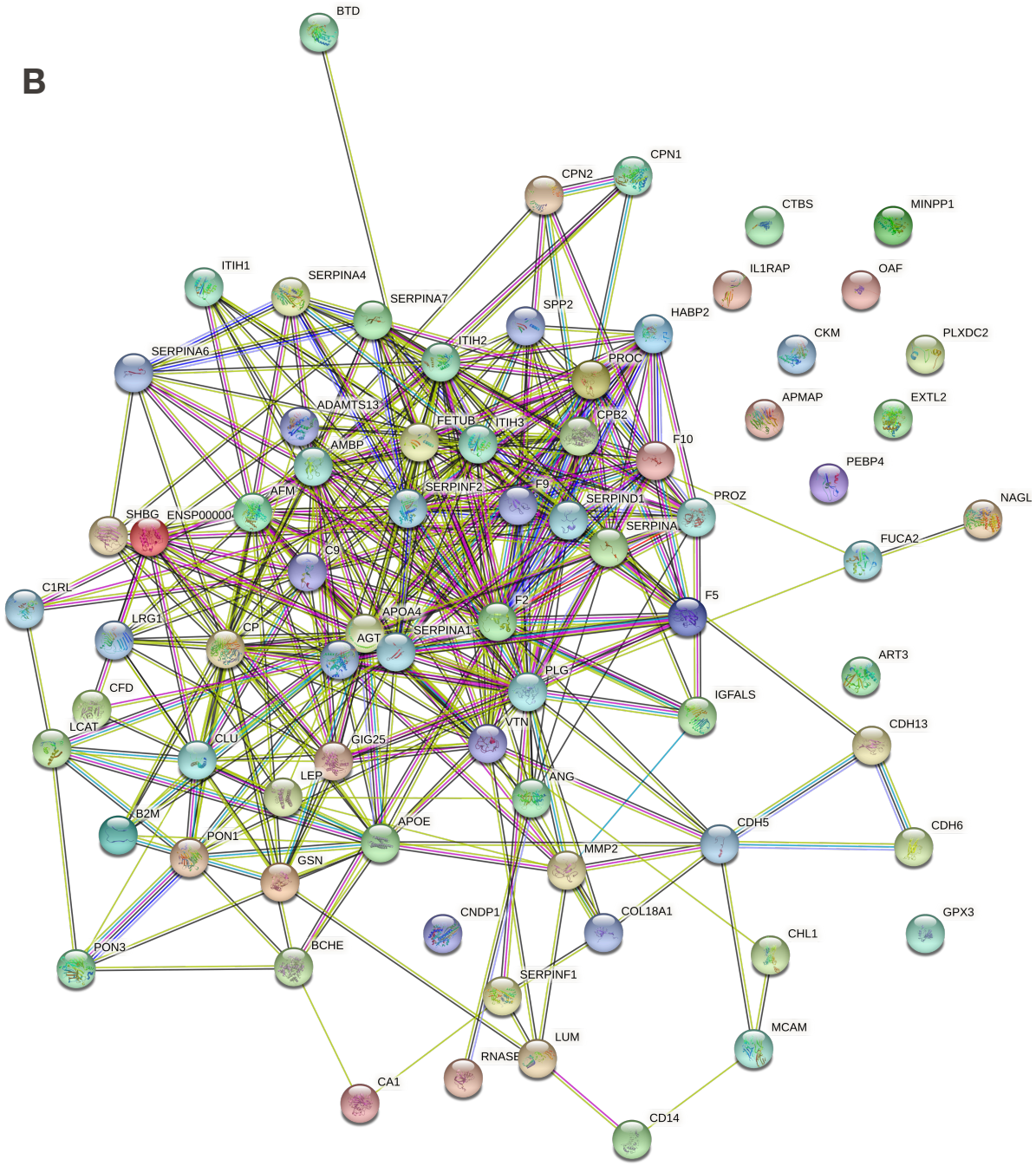

Figure 4.10. Protein-protein interactions (PPIs) network of de-regulated proteins from lipoprotein-cholesterol nanoparticles (cancer diseased vs. healthy samples).

A) PPIs network of up-regulated proteins from lipoprotein-cholesterol nanoparticles (cancer diseased vs. healthy samples). B) PPIs network of down-regulated proteins from lipoprotein-cholesterol nanoparticles (cancer diseased vs. healthy samples). De-regulated proteins were quantified from FDR ≤ 0.01 with fold-change >2 or <0.5.

Table 4-3. Top 30 protein candidate biomarkers with upregulated abundance comparing cancer diseased vs healthy lipoprotein-cholesterol nanoparticle

Protein Upregulated in Human melonoma cancer patient						
Protein Names	Gene Names	Biological process	Cellular components	Fold change	LIMMA p value	FDR
Hemoglobin subunit beta	HBB	biogenesis; metabolic process	cytosol; extracellular	8.22	8.06E-09	FDR <= 0.01
Complement factor I	CFI	defense response; metabolic process	extracellular; membrane	7.81	4.57E-08	FDR <= 0.01
Ficolin-1	FCN1	defense response; metabolic process	extracellular; membrane	5.81	3.57E-10	FDR <= 0.01
Hemoglobin subunit alpha	HBA1	biogenesis; metabolic process	cytosol; extracellular	5.68	4.70E-08	FDR <= 0.01
Fibronectin	FN1			5.33	1.97E-08	FDR <= 0.01
Complement C3	C3	defense response; metabolic process	extracellular; membrane	5.33	1.12E-07	FDR <= 0.01
Properdin	CFP	defense response; metabolic process	extracellular; organelle lumen	5.24	2.01E-06	FDR <= 0.01
Latent-transforming growth factor beta-binding protein 1	LTBP1	metabolic process	cell surface; extracellular	5.20	4.65E-08	FDR <= 0.01
Complement C3 (Fragment)	C3	metabolic process		4.74	1.43E-05	FDR <= 0.01
Hemoglobin subunit delta	HBD	coagulation; transport	cytosol	4.59	5.81E-08	FDR <= 0.01
Ficolin-2	FCN2	defense response; metabolic process	extracellular	4.33	7.14E-07	FDR <= 0.01
Complement C1q subcomponent subunit A	C1QA	defense response; metabolic process	extracellular; membrane	4.17	9.41E-09	FDR <= 0.01
Complement factor H	CFH	defense response; metabolic process	extracellular	4.04	1.02E-07	FDR <= 0.01
Complement factor H	CFH	defense response; metabolic process	extracellular	4.00	9.31E-08	FDR <= 0.01
Ficolin-3	FCN3	defense response; metabolic process	extracellular	3.96	3.32E-07	FDR <= 0.01
Amyloid-beta A4 protein (Fragment)	APP	regulation of biological process		3.83	9.98E-06	FDR <= 0.01
Alpha-amylase 1A	AMY1A			3.70	8.98E-06	FDR <= 0.01
Thrombospondin-1	THBS1	cellular component movement; defense response	cell surface; cytoplasm	3.64	5.89E-05	FDR <= 0.01
Complement C1q subcomponent subunit C	C1QC	defense response; metabolic process	extracellular; membrane	3.64	3.77E-08	FDR <= 0.01
Mannan-binding lectin serine protease 1	MASP1	defense response; metabolic process	cytosol; extracellular	3.62	9.53E-08	FDR <= 0.01
Complement component 8 subunit beta	C8B	response to stimulus		3.52	0.02475551	FDR <= 0.05
Complement C5	C5	cellular component movement; defense response	extracellular	3.48	1.63E-08	FDR <= 0.01
Matrix metalloproteinase-9	MMP9	cell differentiation; cell organization and biogenesis	extracellular	3.37	0.00013242	FDR <= 0.01
Extracellular matrix protein 1	ECM1	defense response	extracellular; organelle lumen	3.29	0.0003723	FDR <= 0.01
CD5 antigen-like	CD5L	cell death; defense response	cytoplasm; extracellular	3.18	0.00017325	FDR <= 0.01
Immunoglobulin heavy constant mu	IGHM	cellular component movement; defense response	cell surface; extracellular	3.18	0.0002036	FDR <= 0.01
Alpha-1-acid glycoprotein	ogchi	regulation of biological process; transport	extracellular	3.15	0.01623408	FDR <= 0.05
Angiopoietin-1	ANGPT1	cell differentiation; cellular component movement	extracellular; membrane	3.09	0.00071498	FDR <= 0.01
Immunoglobulin lambda variable 7-43	IGLV7-43	cellular component movement; metabolic process	extracellular; membrane	3.01	0.00061387	FDR <= 0.01
Catalase	CAT	cell differentiation; cell organization and biogenesis	cytosol; endoplasmic reticulum	3.00	1.12E-07	FDR <= 0.01

Table 4-4. Top 30 protein candidate biomarkers with downregulated abundance comparing cancer diseased vs healthy lipoprotein-cholesterol nanoparticle

Protein Downregulated in Human melonoma cancer patient

Protein Names	Gene Names	Biological process	Cellular components	Fold change	LIMMA p value	FDR
Leucine-rich alpha-2-glycoprotein	LRG1	cell differentiation	extracellular; membrane	0.11	2.13E-06	FDR <= 0.01
Ceruloplasmin	CP	cellular homeostasis; metabolic process		0.14	5.88E-06	FDR <= 0.01
Fetuin-B	FETUB	regulation of biological process	extracellular	0.15	2.07E-07	FDR <= 0.01
Alpha-1-antichymotrypsin	SERPINA3	defense response; regulation of biological process	extracellular; nucleus	0.19	2.97E-06	FDR <= 0.01
C3/C5 convertase		metabolic process		0.19	1.06E-06	FDR <= 0.01
Pigment epithelium-derived factor	SERPINF1	cell proliferation; cellular homeostasis	extracellular	0.20	2.50E-07	FDR <= 0.01
Isoform 2 of Alpha-1B-glycoprotein	A1BG	transport	extracellular; organelle lumen	0.21	3.76E-07	FDR <= 0.01
Cadherin-6	CDH6	cell organization and biogenesis	membrane	0.21	2.00E-06	FDR <= 0.01
Lumican	LUM	cell organization and biogenesis; metabolic process	extracellular; organelle lumen	0.22	6.65E-07	FDR <= 0.01
Heparin cofactor 2	SERPIND1	coagulation; metabolic process	extracellular; organelle lumen	0.22	2.35E-06	FDR <= 0.01
Biotinidase	BTD	metabolic process	extracellular; organelle lumen	0.22	3.77E-07	FDR <= 0.01
Di-N-acetylchitobiase	CTBS	metabolic process	vacuole	0.23	4.76E-08	FDR <= 0.01
Apolipoprotein A-IV	APOA4			0.24	1.35E-08	FDR <= 0.01
Prothrombin	F2	cellular component movement; cellular homeostasis	extracellular; membrane	0.25	2.70E-06	FDR <= 0.01
Immunoglobulin heavy constant epsilon	IGHE	cell organization and biogenesis; defense response	extracellular; membrane	0.25	0.0001575	FDR <= 0.01
Alpha-1-antitrypsin	SERPINA1	defense response; metabolic process	endoplasmic reticulum	0.26	4.93E-07	FDR <= 0.01
Kallistatin	SERPINA4	regulation of biological process;transport	extracellular; organelle lumen	0.26	9.33E-06	FDR <= 0.01
Collagen alpha-1(XVIII) chain	COL18A1	cell organization and biogenesis; metabolic process	extracellular; organelle lumen	0.26	2.19E-07	FDR <= 0.01
Isoform 2 of Gelsolin	GSN	cell death; cell organization and biogenesis	cytoplasm; cytoskeleton	0.27	2.49E-05	FDR <= 0.01
Carboxypeptidase N subunit 2	CPN2	metabolic process; regulation of biological process	extracellular	0.27	3.26E-06	FDR <= 0.01
Carboxypeptidase N catalytic chain	CPN1	metabolic process; regulation of biological process	extracellular; Golgi	0.27	1.01E-07	FDR <= 0.01
Insulin-like growth factor-binding protein complex acid labile subunit	IGFALS	metabolic process; regulation of biological process	extracellular	0.28	7.82E-07	FDR <= 0.01
Vitamin K-dependent protein Z	PROZ	metabolic process	extracellular; organelle lumen	0.28	2.58E-07	FDR <= 0.01
Inter-alpha-trypsin inhibitor heavy chain H1 (Fragment)	ITIH1	metabolic process; regulation of biological process		0.28	0.00148771	FDR <= 0.01
Carbonic anhydrase (Fragment)	CA1	metabolic process	cytoplasm	0.29	7.90E-07	FDR <= 0.01
Carboxypeptidase B2	CPB2	cellular homeostasis; coagulation	extracellular	0.30	1.96E-05	FDR <= 0.01
Ecto-ADP-ribosyltransferase 3	ART3	metabolic process	extracellular; membrane	0.30	5.55E-08	FDR <= 0.01
Vitronectin	VTN	cell differentiation; cell organization and biogenesis	cytoplasm; endoplasmic reticulum	0.31	4.68E-06	FDR <= 0.01
ADAMTS-like protein 4	ADAMTSL4			0.31	1.93E-05	FDR <= 0.01
Complement C1r subcomponent-like protein	C1RL	defense response; metabolic process	extracellular	0.31	1.23E-07	FDR <= 0.01

Protein-protein interactions (PPIs) are essential to almost every process step in a cell. The networks between PPIs are mathematical representations of the physical contacts between proteins. They are usually specific, they occur between defined regions in the proteins, and they have a particular biological meaning. Understanding PPIs is crucial for understanding cell physiology in normal and diseased states. The knowledge of PPIs can be used to assign putative roles to uncharacterized proteins, add fine-grained details of the steps within a signaling pathway, understand the relationships between proteins that form multi-molecular complexes such as proteasome, and help on the target drug development. In Figure 4.10, we presented PPIs network of de-regulated proteins from lipoprotein-cholesterol nanoparticles (cancer diseased vs. healthy samples), which were quantified from FDR ≤ 0.01 with fold-change >2 or <0.5. We can see from the network, most of the de-regulated proteins are closely connected to each other in terms of biological process. Among the up-regulated proteins, there are two known cancer related proteins in the center of the network. Transforming growth factor beta 1 (TGFß1) is related to carcinogenesis, in the early stage it suppresses the tumor growth, but in the late stage, it can promote tumor growth and metastasis. The other one fibronectin 1 (FN1) is usually used as a cancer prognosis biomarker. It's a central organizer of ECM, it mediates the crosstalk between the tumor microenvironment and cancer cell, and it assists tumor growth, progression, and invasion.

Furthermore, in Table 4-3 and 4-4, except differentially expressed protein fold-change with LIMMA *p*-value and FDR confidence, each protein's biological process, and protein cellular positions were also listed. There are three major biological processes of these proteins: cell differentiation, metabolic process, and defense response. As we already know that cancer is a disease with irregular cell differentiation, and emerging evidence indicates nearly all kinds of cancer, no matter cellular or tissue origin, there is a high relationship with impaired cellular energy metabolism. Besides, although the process of cancer immunosurveillance of a clinically relevant tumor is very reluctant, the tumor generating cells are usually those very immune-evasive or highly mutagenic neoplastic cells; thus, certain defense response-related proteins in cancer patients were upregulated as well. Furthermore, cellular components indicate specific locations of these detected proteins; they are from the extracellular, cell membrane, organelle lumen, nucleus, or cytoplasm, which show the complexity but at the same time reveal the possible carried information from cancer cells or tissues.

4.6 Conclusion

In summary, we have shown good preliminary data supporting the idea to use lipoprotein-cholesterol nanoparticles as fingerprints for cancer detection. By simply using PEG10K to precipitate lipoprotein-cholesterol nanoparticles in the serum, we can successfully eliminate the most abundant inert protein serum albumin and accumulate low abundance proteins, which are usually masked by serum albumins. TMT labeling technique was applied to decrease the variance between each experiment due to different ionization efficiency, allowing high-throughput quantification. In this preliminary data of proteomic analysis, within false discovery rate FDR ≤ 0.05, differentially expressed proteins either upregulated or downregulated proteins number is around 10 times compared to directly detect from serum itself (cancer diseased vs. healthy samples), which indicates this detection system is more sensitive and increase the accuracy of a cancer diagnosis. The differentially expressed proteins also show close connections to each other in the different biological processes, including cell differentiation, metabolic process, and defense response in different cellular components. As a conclusion, this lipoprotein-cholesterol nanoparticle-based cancer diagnosis method might provide a novel, more sensitive, and accurate system, potentially applicable for future clinical use.

4.7 Materials, Instruments, and Methods

Materials

Melanoma Cancer patients' serum are from our collaborator Prof. Daniel Speiser (UNIL). In total 5 samples, each sample contains 1 mL serum (two from female age 39 and 44, three from male age 28, 29, and 59, the cancer stage is late stage).

Protein BSA and pooled serum from healthy donors were purchased from Sigma Aldrich (Missouri, United States). Chemical polyethylene glycol (PEG) 10000 was purchased from Sigma Aldrich (Missouri, United States). PBS pH 7.4 (1X) was purchased from Life Technology (California, United States). NuPAGE^{TM} 4 to 12% Bis-Tris gel was purchased from Thermo Fisher (Massachusetts, United States). Unless otherwise noted, all chemical and biological reagents were used as received. All solvents purchased were reagent grade.

Instruments

Fast protein liquid chromatography (FPLC) was acquired from ÄKTA go (Cytiva, Massachusetts, United States). Lipoprotein-cholesterol nanoparticle size was characterized by dynamic light scattering (DLS) on Malvern Nano ZS (Worcester, UK) and analytical ultracentrifugation (AUC) (Beckman Coulter, California, United States). Lipoprotein-cholesterol nanoparticle morphology visualization was measured by negative staining transmission electron microscopy (TEM) of Tecnai Osiris (FEI, Oregon, United States). SDS-PAGE electrophoresis running equipment was purchased from Fisher Scientific (New Hampshire, United States). Mass Spectrometry was performed with Dionex Ultimate 3000 RSLC nano UPLC system online connected with an Exploris 480 Orbitrap Mass Spectrometer (Thermo Fisher Scientific, New Hampshire, United States).

Methods

Extraction of lipoprotein-cholesterol nanoparticles

1 mL serum sample was first to dilute 10 times into 10 mL with PBS 7.4 1X, and then centrifuge under 12000 rpm for 30 mins in order to remove big aggregates in the serum. After centrifugation, serum was first filtered with 0.22 μm membrane and then adding 1/5 volume of serum (2 mL) 50% (W/V) PEG 10K, mix well, and leave it at 4 degrees for 1 hour. Centrifuge the serum with PEG mixture under 2000 rpm for 15 mins, and discard the supernatant. Resuspend the precipitates with PBS 7.4 1X into 5 mL, adding 1/5 volume of the serum solution (1 mL) 50% (W/V) PEG 10K; the second time, mix well and leave it at 4 degrees for 30 mins. Centrifuge the serum with PEG mixture under 2000 rpm for 15 mins, and discard the supernatant. Resuspend the precipitates with PBS 7.4 1X into 1 mL for further FPLC sec column purification.

Fast protein liquid chromatography purification

An automated FPLC system ÄKTA Go FPLC Cytiva equipped with a size exclusion column HiPrep Sephacryl S-500 HR column was used to purify lipoprotein-cholesterol nanoparticles. The samples were dispersed in Dulbecco's phosphate-buffered saline PBS 1X pH 7.4 and were eluted in PBS 1X at a constant flow rate of 0.5 mL/min. 2ml of the sample was injected into the column using a coil loop. The sample absorption at 280 nm was automatically recorded and then used to collect desired fractions. The fraction volume was kept constant at 3 ml throughout the runs.

Characterization of lipoprotein-cholesterol nanoparticles

SDS-PAGE: NuPAGE™ 4 to 12% Bis-Tris gel was used in this experiment. 3 μg protein-containing serum from cancer patients and healthy donors and lipoprotein-cholesterol nanoparticle samples extracted from cancer patients and healthy donors were dissolved in PBS 7.4 1X into 10 μL, adding together with Novex™ Tris-Glycine SDS sample loading buffer (2X) 10

μL. Electrophoresis running buffer was using MES buffer, and the gel was stained by Coomassie blue gel staining solution. The final gel was imaged by a Bio-Rad gel imaging system.

DLS: Lipoprotein-cholesterol nanoparticle product solutions were in miliq water with a concentration of 1 mg/mL. Eppendorf disposable cuvette with absorbance range 220 - 1600 nm was used. 100 μL volume was put in the cuvette and measured by instrument Malvern NanoZS with condition manually scan for 10 runs under room temperature.

AUC: Analytical ultracentrifugation was performed in a Beckman XL-A analytical ultracentrifuge using an An50Ti or An60Ti rotor at 20°C. Concentration profiles as a function of radial positions and time were acquired with UV absorption scanning optics of the ultracentrifuge. These sedimentation velocity experiments were carried out using Titanium double-sector centerpieces at speeds from 10 000-20 000 rpm. The PBS 1x buffer was used in the reference sector, and in the sample sector, the sample with OD in the range from 0.5-1 was used. The sedimentation data were analyzed by fitting a numerical solution of Lamm's differential equation to the concentration profiles using the Sedfit program v16.36. Diffusion-corrected differential sedimentation coefficient distributions c(s) was used to evaluate the sedimentation constants of the samples.

TEM: Samples of lipoprotein-cholesterol nanoparticles were diluted to 0.8 mg/ml (optical OD at 280 nm 0.5) with Dulbecco's phosphate-buffered saline buffer (PBS) 1x and then stained by aqueous uranyl acetate (0.5 wt%) on a carbon film grid. The dry samples were imaged by transmission electron microscopy (TEM) operated at 200KV. The acquired images were analyzed by ImageJ v. 1.53.

Proteomic analysis

Sample preparation for Mass Spectrometry

Each sample was digested by filter aided sample preparation (FASP)[283] with minor modifications. All buffer exchanges were performed on a bench centrifuge at 10'000 rpm. Proteins (Serum, Nanoparticle and HDL samples initial protein content: 20 μg; LDL samples initial protein content: 15μg) were reduced with 10 mM TCEP in 8M Urea, 0.1M Tris-HCl pH 8.0 at 37°C

for 60 mins and further alkylated with 40 mM Chloroacetamide in 8 M Urea, 0.1 M Tris-HCl pH 8.0 at 37°C for 45 mins light protected. Proteins were digested overnight at 37°C using 1/50 w/w enzyme-to-protein ratio with a combination of mass spectrometry grade trypsin (Pierce) and LysC (Wako) supplemented with 10 mM $CaCl_2$. Generated peptides were eluted sequentially with 3 x 50 µl of 4% TFA and desalted on C18 Empore StageTips using the standard protocol.[284] Purified peptides were dried down by vacuum centrifugation. For TMT labeling, dried peptides were first reconstituted in 10 µl 100 mM HEPES pH 8 and 4 µl of TMT solution (25 µg/µl in pure acetonitrile) was then added. TMT Labelling was performed at room temperature for 90 mins, and reactions were quenched with hydroxylamine (0.3% v/v final) for 10 mins. A minor fraction of TMT-labeled samples were then pooled at a 1:1 ratio across all samples. A single shot control LC-MS run was performed to ensure similar peptide mixing across each TMT channel to avoid the need for further excessive normalization. Quantities of each TMT-labeled sample were adjusted according to the control run. The combined samples were then desalted using a 100 mg SEP-PAK C18 cartridge according to provider recommendations and vacuum centrifuged. Pooled samples were fractionated into 12 fractions using an Agilent OFF-Gel 3100 system following the manufacturer's instructions. The resulting fractions were desalted again using SDB-RPS Empore StageTips and dried by vacuum centrifugation.

LC-MS/MS analysis

Each individual fraction was resuspended in 2% Acetonitrile; 0.1% Formic acid and nano-flow separations were performed on a Dionex Ultimate 3000 RSLC nano UPLC system online connected with an Exploris 480 Orbitrap Mass Spectrometer. A capillary pre-column (Acclaim Pepmap C18; 3µm-100Å; 2cm x 75µm ID) was used for sample trapping and cleaning. Analytical separations were performed at 250nl/min over a 150min. biphasic gradients on a 50cm long in-house packed capillary column (75µm ID; ReproSil-Pur C18-AQ 1.9µm silica beads; Dr. Maisch). Acquisitions were performed through Top Speed Data-Dependent acquisition mode using 3 seconds cycle time. First MS scans were acquired at a resolution of 120'000 (at 200m/z), and the most intense parent ions were selected and fragmented by High energy Collision Dissociation (HCD) with a Normalized Collision Energy (NCE) of 36% using an isolation window of 0.7m/z. Fragmented ions scans were acquired with a resolution of 45'000 (at 200m/z), and selected ions were then excluded for the following 45s.

Data analysis

Raw data were processed using SEQUEST, Mascot, MS Amanda[285] and MSFragger[286] in Proteome Discoverer v.2.4 against the Uniprot Human Reference Proteome (LM210129, 77'027 entries). Enzyme specificity was set to trypsin, and a minimum of six amino acids was required for peptide identification. Up to two missed cleavages were allowed, and a 1% FDR cut-off was applied both at peptide and protein identification levels. For the database search, carbamidomethylation (C), TMT tags (K and Peptide N termini) were set as fixed modifications, whereas oxidation (M) was considered as a variable. The resulting text files were processed through in-house written R scripts (version 3.6.3). Two steps of normalization were applied. The first step of normalization was the sample loading normalization[287]. Assuming that total protein abundances were equal across the TMT channels, the reporter ion intensities of all spectra were summed, and each channel was scaled according to this sum so that the sum of reporter ion signals per channel equals the average of the signals across samples. Then, the Trimmed M-Mean normalization step was also applied using the package EdgeR[288] (version 3.26.8). Assuming that the majority of proteins in the samples are non-differentially abundant, this second step calculates normalization factors according to these presumed unchanged protein abundances. During this process, proteins with high or low abundances and proteins with larger or smaller fold-changes were not considered. Differential protein expression analysis was performed using the R Bioconductor package limma (version 3.40.6),[289] followed by the Benjamini-Hochberg multiple testing correction method.[290] Adjusted P values lower than 0.05 (FDR < 0.05) were considered as significant.

Safety consideration

No unexpected or unusually high safety hazards were encountered.

Chapter 5 Conclusion

5.1 Achieved results

Peptide engineering for personalized cancer vaccine development

In this work, a carrier-free neoepitope-based cancer vaccine delivery system was developed. This approach described here based on a highly efficient covalent conjugation of amines in DMSO or aqueous solution doesn't require the use of any denaturing conditions such as heating and therefore showed high promise for the delivery of a wide range of individualized neoepitopes with good compatibility. First of all, on the material preparation wise, this strategy shows > 99% incorporation efficiency of antigen peptides, adjuvant and remarkably loading capacity of cargos. The intracellular traceless release of antigens was also proved for efficient antigen processing and presentation by DCs. Besides, the versatility of this platform was also investigated by extending the preparation of nanovaccine with diverse structures and properties, including neoantigens identified from mouse tumors.

The LNs targeting efficiency in *vivo* of this nanovaccine is remarkably high and shows 10.2-, 7.6-, and 5.5-fold higher than free antigen peptide, adjuvant, and a simple mixture of the two, respectively. Furthermore, the efficiency of antigen capture by APCs in LNs in *vivo* was proved 14.0- and 17.7-fold higher of this nanovaccine compared to a mixture of free antigen peptide and adjuvant in the absence or presence of Montanide, respectively. And at the same time, co-delivery of adjuvant still keeps the stimulation of BMDCs to a similar level as a monomeric adjuvant, while cross-primed antigen-specific naive OT-1 $CD8^+$ T cells are greatly enhanced compared to monomeric antigen peptides. The mechanism why this nanovaccine can promote the cross-presentation of antigens was investigated and explained. At last, this work also showed T cell immune response and antitumor activity induced by this nanovaccine in *vivo*, it elicited a high frequency (6.00%) of antigen-specific $CD8^+$ T cells immune response and was 7.8- and 10-fold higher compared to the mixture of antigen peptide and adjuvant in solution and Montanide, respectively. It also remarkably expanded the antigen-specific T effective memory cells to a number 10.5- and 22.8-fold greater than a simple mixture of antigen peptide and adjuvant in solution and Montanide, respectively. Mice immunized with this nanovaccine showed significantly delayed tumor growth and prolonged survival.

As a conclusion, this system is a facile, effective, and versatile vaccine platform for the delivery of peptide neoantigens to enhance personalized cancer immunotherapy. It allows co-delivery of peptide antigens and molecular adjuvants of diverse structures and properties, which is a highly desired property as individually identified neoantigens from patients could vastly differ in physiochemical properties. Besides, this carrier-free delivery strategy, like other direct assemblies of antigen peptide or protein with non-covalent assembly reported, has its unique advantage of minimizing the potential risk of immunogenicity and toxicity from these additional carrier materials.

Protein engineering for antiviral drug development

In this work, an easy manufacture, broad-spectrum effective, and versatile protein-based antiviral platform was developed. This approach described here is based on a simple one-step chemical reaction under room temperature and can be easily scale-up or scale-down with a yield > 80%. Modified proteins with high re-producibility showed not only effective antiviral inhibition but also a good virucidal effect. Two important key factors, ligand density and hydrophobic force were shown significantly influenced antiviral inhibition and viricidal effect.

As a proof of concept, BSA, the most abundant serum protein, was used as the core. By varying the ligand density during the reaction, we could turn an inert protein into an antiviral material with inhibitory activity: the antiviral inhibition EC_{50} increased from 0.052 μM (56% ligand density) to 23.6 μM (22% ligand density) to loss of all inhibition (11% ligand density). By varying ligand hydrophobic length from 3 to 6 to 12 -CH_2-, the final functionalized protein's antiviral inhibition EC_{50} remains in the similar range (<0.2 μM), but it converts from virustatic (3 and 6 -CH_2-) to virucidal (12 -CH_2-). Besides, the versatility of this approach is also proved by varying the protein core. Crossing a range of isoelectric points and molecular weights, we can turn any protein into an effective antiviral material by applying the same conjugation method. In this work, three different proteins, BSA, Avidin, and Cytochrome C were used as protein cores while maintaining the same synthesis protocol; all products showed effective antiviral inhibition ($EC_{50\text{-BSA}}$ = 0.052 μM, $EC_{50\text{-Avidin}}$ = 0.208 μM, $EC_{50\text{-Cyto C}}$ = 0.592 μM). At last, this protein-based non-toxic virucidal material was also proved displaying broad-spectrum antiviral inhibition against Herpes simplex virus (HSV-2) with EC_{50} = 0.149 μM against Influenza virus (H1N1) with EC_{50} = 0.04 nM, against SARS-CoV-2 (Alpha) virus with EC_{50} = 2.42 μM.

As a conclusion, this protein-based antiviral approach is facile for manufacture, high re-producible, scalable, versatile, and broad-spectrum effective for potential clinical translation. Besides, this novel platform uses natural protein as a core base, it's biocompatible, and the protein itself can be inert or functional, i.e., enzymes or therapeutical antibodies, which add additional value for synergistic combinational therapy.

Lipoprotein-cholesterol nanoparticles for cancer diagnosis

In this work, a non-invasive lipoprotein-cholesterol nanoparticle-based cancer biomarker detection method potentially for cancer diagnosis was established based on our preliminary test. The lipoprotein-cholesterol nanoparticle extraction approach described here is a simple and reproducible method. By simply using PEG 10K to precipitate these lipoprotein-cholesterol nanoparticles in the serum, we can successfully eliminate the most abundant inert protein serum albumin and accumulate low abundance proteins, which is usually masked by serum albumins.

In this proteomic analysis, TMT isobaric tag labeling was applied in order to reduce the variance between each experiment due to different ionization efficiency, allowing high-throughput quantification. In experiment quality control, up to two missed cleavages were allowed, and a 1% FDR cut-off was applied both at peptide and protein identification levels. Besides, the principal component analysis after two steps of normalization (sample loading normalization and trimmed M-Mean normalization) was performed, and results indicate both were heterogeneous of healthy serum and cancer diseased serum, but relatively homogeneous of healthy lipoprotein-cholesterol nanoparticles and heterogeneous of cancer diseased lipoprotein-cholesterol nanoparticles, which might occur due to patient's gender, age and cancer stage. This needs to be further confirmed by a large number of cancer patients' samples.

Besides, in cancer diseased and healthy lipoprotein-cholesterol nanoparticle pairwise comparison, within false discovery rate less than 0.05, differentially expressed proteins either upregulated or downregulated proteins number is proved around 10 times compared to directly detect from serum itself (cancer diseased vs. healthy samples), which makes this detection system is more sensitive and increase the accuracy of a cancer diagnosis. The differentially expressed proteins level indicates the different biological processes, including cell differentiation,

metabolic process, and defense response in cellular components in cancer patients while compared to healthy people, and they are potential can be used as fingerprints for cancer diagnosis. As a conclusion, based on our preliminary test data, this lipoprotein-cholesterol nanoparticle-based cancer biomarker detection method might provide a novel, more sensitive, and accurate system, potentially applicable for future clinical use.

5.2 Future development

Peptide engineering for personalized cancer vaccine development

Vaccine either for cancer or infectious disease development under normal circumstances typically takes up to 10-15 years due to its complexity. However, the recent special case of vaccine development for SARS-CoV-2, the virus that causes COVID-19, only takes about one year from the virus first identified to vaccine receive emergency use authorization from FDA. Creating a vaccine in under one year is a great challenge; it requires global cooperation for research and data share distribution because, during a global pandemic, time was a luxury the world could not afford, and thanks to the funding sources ranging from the government to the private sectors. Different types of vaccines have been developed accordingly in this pandemic, such as DNA vaccine, mRNA vaccine, non-replicating viral vector vaccine, inactivated vaccine, live attenuated vaccine, and subunit vaccine. Although in this work, we used a subunit vaccine, it would be interesting we made a brief comparison between different techniques.

DNA vaccine like INO-4800 for COVID-19 does not require live viruses, the manufacturing process is also relatively straightforward, storage condition is not critical, but the vaccination method is limited, which usually requires high transfection like electroporation and mutation in host DNA is possible. Compared to DNA vaccines that need to deliver into the nucleus, mRNA vaccine only needs to enter the cytoplasm; thus, theoretically, they are safer. Currently available mRNA vaccines like BNT162b2 and Moderna mRNA-1273, although they reach high protection efficacy > 90%, the long-term immune effect is not satisfactory. The immune protection generated by the vaccine declined rapidly within one year, and no cellular immune response plus side effects such as headaches, fatigue, and muscle pain were observed. Non-replicating viral vectors like adenovirus vaccines, for instance, CanSino and AstraZeneca, with a double-stranded DNA genome can generate relatively high effectiveness but may not be

suitable for people with recessive infectious viruses. Inactivated vaccines are the most common type of vaccine; they are usually safe and can induce good humoral immune responses; the problem is the cellular T-cell immune response is generally weak, which is essential, especially in cancer vaccine development. Besides, vaccine production requires a high concentration of live viruses, which potentially cause a biological safety risk. Compared to the inactivated vaccine, live attenuated vaccine always has very good immunogenicity and can induce lasting systemic immunity, the risk of this type of vaccine is it might restore virulence in the body due to retrograde mutations, cannot give it to immunosuppressed individuals plus the storage is very critical.[291,292]

The last type of vaccine is virus-like particle and nanoparticle subunit vaccine, which is also the case in this research work. Subunit vaccines usually use antigens like peptides or purified proteins, which enhance the safety and scalability compared to the whole-pathogen vaccines. The disadvantage of subunit vaccine is they are generally weak immunogenic therefore requires extra adjuvants combination. Strategies via using virus-like particles or nanoparticles are aiming for increasing immunogenicity, stability, and target delivery to enhance immune efficacy.[293] In case of cancer vaccine development, except humoral immune response, cellular immune response, especially like $CD8^+$ T cell response, is essential, and every vaccine preparation technique has its pros and cons, in this case, subunit vaccine has its unique advantages but at the same time still requires further improvement on the target secondary lymphoid delivery of vaccine components and enhancement on cross-priming antigen-specific T cell immune response.

In this work, we envision that this carrier-free neoepitope-based cancer vaccine delivery strategy can be readily extended to the co-delivery of multiple heterogeneous epitopes in the form of peptides, proteins (e.g., whole tumor cell lysate), or replicon mRNAs/DNAs encoding the neoepitopes. Implementation of various responsive chemistry in the linker-monomer could potentially impart different responsiveness to this vaccine delivery platform, facilitating triggered release of antigens and/or adjuvants by intracellular stimuli including pH change, reactive oxygen species, protease, etc. Thus, in the future, what we could do is first expand neoepitope-based antigen peptides diversity both from mice origin and human origin, then from peptides to protein and mRNAs/DNAs. Extending the co-delivery of multiple heterogeneous epitopes-based antigens from one or more than one tumor can also be established. Implementation of various stimuli-responsive such as pH, thermal, light, enzymatic, ROS, etc., linkers

for novel vaccine formulation would also be interesting. At last, cancer vaccines, except for prophylactic purposes but for therapeutic purposes on solid tumors, would also be essential to be investigated.

Protein engineering for antiviral drug development

Antiviral drug development is always challenging, not only due to the reason that viruses tend to use the host's cells to replicate, which makes it more difficult to design safe and effective antivirals with minimal interference to the host organism but also because viruses are constantly keeping mutation, which increases the obstacles for effective antiviral drugs development. Based on virus-specific infection life cycle, researchers get inspired and develop rational antiviral drug design strategies such as attacking viruses at every stage of their life cycles. The current major type of antiviral drugs is to interfere with the virus components synthesis and assembly after they invade a host cell, and most FDA-approved antiviral drugs are small molecules. Despite the rapid progress in the biomedical techniques of antiviral drug development, there are still many challenges to discover new promising antiviral targets and drugs.

As it usually takes years to develop and get a new antiviral drug approved for use because identifying the chemical compounds targeting the virus, testing its efficacy and safety both in preclinical and clinical is a long process, not even mention the input cost; however, the high frequency of virus mutation, new emerging and re-emerging viruses make the whole antiviral drug development dramatically lagged, it is unlikely to result in timely and effective therapies against these numerous pathogens causing sometimes rare but lethal infections. Based on these observations, broad-spectrum antivirals that can act on multiple viruses are highly demanded. Macromolecules including polypeptides, proteins, and nanoparticles are particularly attractive due to their multivalency and versatility, thus potentially displaying a broad-spectrum antiviral function and lowering the risk of drug resistance for emerging and muted viruses.

Most broad-spectrum antivirals use the strategy to block the ability of the virus from attaching to the host cell membrane and releasing its viral genes. There are usually two ways either mimicking the virus-associated protein (VAP) to develop analogues of targeting protein or mimicking the cellular receptor and binding to the VAP. The former one can compete for binding to cellular receptors to reduce the virus attachment, and the latter one can compete

binding to virus-associated proteins. These types of antivirals are focused on VAP anti-idiotype antibodies, anti-cellular receptor antibodies, and natural ligands of the cellular receptors. However, monoclonal antibody-based antivirals, although they are usually highly specific and effective, they are also very costly. The production of the monoclonal antibody also needs a careful operation, tedious purification, and it's very difficult to scale up. Besides, the side-effect of monoclonal antibodies such as immunogenicity still remains a big concern.

Synthetic ligands mimicking cellular receptors are usually attached to the surface of nanoparticles or other carriers to display their antiviral inhibition. A lot of metal core and polymer core were used together with these ligands and were shown to have antiviral effects. But to date, no protein core with ligands functionalization has been reported for antivirals, which might be due to the complexity of the nature of the protein. Thus, in this work, we used model non-functional protein cores in this initial demonstration, by simple one-step chemical functionalization, all protein products showed well-established antiviral effects, one protein product even displayed virucidal effect, further studies will investigate functional, and potentially targeting protein cores such as monoclonal antibodies or some enzymes involving in viral replication circle. Additionally, other ligands with a range of physicochemical properties (e.g., charge and hydrophobicity) will be further investigated; the aim is to open the door to virus-targeted virucidal materials.

Lipoprotein-cholesterol nanoparticles for cancer diagnosis

Cancer biomarker detection directly from biological fluids is always challenging due to its natural complexity. Although multiple detection techniques based on optical microchips have been developed for a variety of components in blood, urine fluids detection with good convenience and cost-effectiveness, their reliability is still a big challenge. The assay sensitivity, like binding efficiency between the probe and target molecule, anti-interference ability towards the nonspecific binding, and specificity of different types of cancers, also needs to be improved, and the technique needs to be standardized.

Proteins are known as vital biomolecules for many aspects of life, including cancer in living organisms. Most protein biomarkers are in the biggest body fluid blood. Directly analyzing protein cancer biomarkers in blood, especially those with very low abundance, is still a very

big challenge. One reason is that proteins cannot be amplified like nucleic acids; thus, it requires high sensitivity and accuracy of the technique; besides, proteins are also sensitive to detection environments such as temperature, pH, and ionic strength, which makes it even more difficult in low concentration; furthermore, the biggest challenge is the direct tracking of traces of protein cancer biomarkers in crude biological samples like blood is hindered by the high background of other non-cancer related proteins in high abundance such as serum albumin.

Techniques commonly used for protein cancer biomarkers detection such as ELISA, electrochemical-based sensors (electrochemical impedance spectroscopy, electrochemiluminescence), field-effect transistors, microfluidic-based point-of-care platforms, sensors by using optical techniques such as light scattering, fluorescent, SPR, and FRET, which display their unique advantages like no need washing steps, straightforward signals, were utilized, although they are relatively cheap, the challenge of lack of specificity and non-specific adsorption still limit their application for directly measuring complex samples like blood or serum. In clinical studies, mass spectrometry is considered a key technique for metabolic cancer biomarker studies due to its high sensitivity, wide dynamic detection range, high resolution, and can analysis extremely complex biological fluids like blood and serum. It's not very convenient and usually requires very expensive deliciated instruments, but it's a reliable and reproducible quantitative analysis technique. Liquid chromatography-mass spectrometry together with tandem mass tag plays an important role in comprehensive proteomics of complex samples like blood or serum.

As no cancer biomarker current available can be taken as a "perfect" biomarker for prediction, diagnosis, and monitoring simultaneously, a single cancer biomarker, even an "ideal" one is tended to have high sensitivity for detection but relatively low specificity for various cancer types, which will raise the risk of false-positive signals. One possible strategy is to evaluate a panel of cancer biomarkers that are already established as important and necessary. As tumor tissue releasing biomarkers into the bloodstream are usually in very low abundance, this natural phenomenon makes them difficult to be detected while other non-cancer related proteins appear in much higher concentrations during directly analyzing component proteins in plasma or serum. In order to increase the low abundance cancer biomarker protein signal, nanomaterials were investigated on spontaneous interaction with plasma proteins and forming protein "corona" on the surface of nanoparticles such as gold, silica, or liposomes. Researchers utilize these adsorbed proteins for cancer biomarker detection; however, non-specific protein adsorption like serum albumin cannot be totally avoided. Besides, the invasive method by

injecting nanoparticles into the body for collecting proteins is still arguable to accept in clinical use.

In this work, we established a non-invasive lipoprotein-cholesterol nanoparticle-based cancer biomarker detection system. Instead of injecting extra artificial nanomaterials into the body, we developed a method to extract lipoprotein-cholesterol nanoparticles directly from serum with high yield, which can successfully eliminate most abundant protein serum albumin in plasma, increasing low abundant protein signal, thus potentially enhancing the detection sensitivity and accuracy of a protein biomarker panel. The current preliminary work was focused on 5 clinical patients with melanoma cancer, but future work would expand to a large number of patients and investigate different cancer types, the influence of patients' gender, age, and stage of cancer. Besides, the lipoprotein-cholesterol nanoparticle extraction protocol will also be further optimized and simplified. Furthermore, this type of lipoprotein-cholesterol nanoparticles was proved to contain lipids and nucleic acids except for proteins in our preliminary experiments; thus, another two branches of directions lipidomic and genomics on cancer biomarker research would also be interesting to investigate in the near future.

References

1. Brannigan, J. A. & Wilkinson, A. J. Protein engineering 20 years on. *Nat. Rev. Mol. Cell Biol.* **3**, 964–970 (2002).

2. Hodgson, D. R. W. & Sanderson, J. M. The synthesis of peptides and proteins containing non-natural amino acids. *Chem. Soc. Rev.* **33**, 422–430 (2004).

3. Conibear, A. C. Deciphering protein post-translational modifications using chemical biology tools. *Nat. Rev. Chem.* **4**, 674–695 (2020).

4. Macek, B. *et al.* Protein post-translational modifications in bacteria. *Nat. Rev. Microbiol.* **17**, 651–664 (2019).

5. Maskarinec, S. A. & Tirrell, D. A. Protein engineering approaches to biomaterials design. *Curr. Opin. Biotechnol.* **16**, 422–426 (2005).

6. Anderson, D. G., Burdick, J. A. & Langer, R. Smart biomaterials. *Science (80-.).* **305**, 1923–1924 (2004).

7. Sakiyama-Elbert, S. & Hubbell, J. F UNCTIONAL B IOMATERIALS : Design of Novel. *Biomed. Eng. (NY).* 183–201 (2001).

8. Hirano, Y. & Mooney, D. J. Peptide and Protein Presenting Materials for Tissue Engineering. *Adv. Mater.* **16**, 17–25 (2004).

9. Griffith, L. G. & Naughton, G. Tissue engineering - Current challenges and expanding opportunities. *Science (80-.).* **295**, (2002).

10. Rege, N. K. *et al.* Structure-based stabilization of insulin as a therapeutic protein assembly via enhanced aromatic–aromatic interactions. *J. Biol. Chem.* **293**, 10895–10910 (2018).

11. Chapman, T. M. & Perry, C. M. Insulin detemir: A review of its use in the management of type 1 and 2 diabetes mellitus. *Drugs* **64**, 2577–2595 (2004).

12. Perego, G., Ghidini, A., Luciani, A. & Petrelli, F. Antibody-drug conjugates in treating older patients suffering from cancer: what is the real value? *Hum. Vaccin. Immunother.* 1–4 (2021). doi:10.1080/21645515.2021.1999711

13. Pan, J. *et al.* Self-blockade of PD-L1 with bacteria-derived outer-membrane vesicle for enhanced cancer immunotherapy. *Adv. Mater.* e2106307 (2021). doi:10.1002/adma.202106307

14. Zhang, B. C. *et al.* Efficient CRISPR/Cas9 gene-chemo synergistic cancer therapy via a stimuli-responsive chitosan-based nanocomplex elicits anti-tumorigenic pathway effect. *Chem. Eng. J.* **393**, 124688 (2020).

15. Alsaiari, S. K. *et al.* Endosomal Escape and Delivery of CRISPR/Cas9 Genome Editing Machinery Enabled by Nanoscale Zeolitic Imidazolate Framework. *J. Am. Chem. Soc.* **140**, 143–146 (2018).

16. Sun, W. *et al.* CRISPR-Cas12a delivery by DNA-mediated bioresponsive editing for cholesterol regulation. *Sci. Adv.* **6**, 1–12 (2020).

17. Lampinen, V., Tamminen, K., Hankaniemi, M. M. & Malm, M. Antigenicity and immunogenicity of HA2 and M2e influenza virus antigens conjugated to norovirus-like , VP1 capsid-based particles by the SpyTag / SpyCatcher technology. *Virol. J.* **566**, 89–97 (2022).

18. Kang, S., Kim, Y., Shin, Y., Song, J. J. & Jon, S. Antigen-Presenting, Self-Assembled Protein Nanobarrels as an Adjuvant-Free Vaccine Platform against Influenza Virus. *ACS Nano* **15**, 10722–10732 (2021).

19. Hoffmann, M. A. G. *et al.* Nanoparticles presenting clusters of CD4 expose a universal vulnerability of HIV-1 by mimicking target cells. *Proc. Natl. Acad. Sci. U. S. A.* **117**, 18719–18728 (2020).

20. Hoffmann, M. A. G., Kieffer, C. & Bjorkman, P. J. In *vitro* characterization of engineered red blood cells as viral traps against HIV-1 and SARS-CoV-2. *Mol. Ther. - Methods Clin. Dev.* **21**, 161–170 (2021).

21. Zhu, D., Li, X., Liu, X., Wang, J. & Wang, Z. Designing bifunctionalized gold nanoparticle for colorimetric detection of Pb 2+ under physiological condition. *Biosens. Bioelectron.* **31**, 505–509 (2012).

22. Mu, C. J., LaVan, D. A., Langer, R. S. & Zetter, B. R. Self-assembled gold nanoparticle molecular probes for detecting proteolytic activity in vivo. *ACS Nano* **4**, 1511–1520 (2010).

23. Gupta, S., Andresen, H., Ghadiali, J. E. & Stevens, M. M. Kinase-actuated immunoaggregation of peptide-conjugated gold nanoparticles. *Small* **6**, 1509–1513 (2010).

24. Saxena, V. K. *et al.* Functionalizing gold nanoparticles with bluetongue virus multiple peptide antigens utilizing gold-thiol interaction: A novel approach to develop pen side test. *Res. Vet. Sci.* **93**, 1531–1536 (2012).

25. Khan, M. U., Saqib, Q. M., Hassan, G. & Bae, J. All printed organic humidity sensor based on egg albumin. *Sens. Bio-Sensing Res.* **28**, 100337 (2020).

26. Cui, M. *et al.* Antifouling sensors based on peptides for biomarker detection. *TrAC - Trends Anal. Chem.* **127**, 115903 (2020).

27. Guo, C. X. *et al.* RGD-peptide functionalized graphene biomimetic live-cell sensor for real-time detection of nitric oxide molecules. *ACS Nano* **6**, 6944–6951 (2012).

28. Wu, C., Zhu, P., Liu, Y., Du, L. & Wang, P. Field-Effect Sensors Using Biomaterials for Chemical Sensing. *Sensors* 1–15 (2021).

29. Mart, R. J., Osborne, R. D., Stevens, M. M. & Ulijn, R. V. Peptide-based stimuli-responsive biomaterials. *Soft Matter* **2**, 822–835 (2006).

30. Krishna, O. D. & Kiick, K. L. Protein- and peptide-modified synthetic polymeric biomaterials. *Biopolymers* **94**, 32–48 (2010).

31. Shimoboji, T. *et al.* Photoresponsive polymer – enzyme switches. *Proc. Natl. Acad. Sci. U. S. A.* **99**, 16592–16596 (2002).

32. Melero, I. *et al.* Therapeutic vaccines for cancer: an overview of clinical trials. *Nat. Rev. Clin. Oncol.* **11**, 509–24 (2014).

33. Rosenberg, S. A., Yang, J. C. & Restifo, N. P. Cancer immunotherapy: moving beyond current vaccines. *Nat. Med.* **10**, 909–915 (2004).

34. Johansen, P., Mohanan, D., Martínez-Gómez, J. M., Kündig, T. M. & Gander, B. Lympho-geographical concepts in vaccine delivery. *J. Control. Release* **148**, 56–62 (2010).

35. Irvine, D. J., Swartz, M. A. & Szeto, G. L. Engineering synthetic vaccines using cues from natural immunity. *Nat. Mater.* **12**, 978–990 (2013).

36. Amigorena, S. & Savina, A. Intracellular mechanisms of antigen cross presentation in dendritic cells. *Curr. Opin. Immunol.* **22**, 109–117 (2010).

37. Brode, S. & MacAry, P. A. Cross-presentation: Dendritic cells and macrophages bite off more than they can chew! *Immunology* **112**, 345–351 (2004).

38. Itano, A. A. *et al.* Distinct dendritic cell populations sequentially present antigen to CD4 T cells and stimulate different aspects of cell-mediated immunity. *Immunity* **19**, 47–57 (2003).

39. Johansen, P. *et al.* Direct intralymphatic injection of peptide vaccines enhances immunogenicity. *Eur. J. Immunol.* **35**, 568–574 (2005).

40. Maloy, K. J. *et al.* Intralymphatic immunization enhances DNA vaccination. *Proc. Natl. Acad. Sci. U. S. A.* **98**, 3299–3303 (2001).

41. Bachmann, M. F. & Jennings, G. T. Vaccine delivery: A matter of size, geometry, kinetics and molecular patterns. *Nat. Rev. Immunol.* **10**, 787–796 (2010).

42. Swartz, M. A. Immunomodulatory roles of lymphatic vessels in cancer progression. *Cancer Immunol. Res.* **2**, 701–707 (2014).

43. McLennan, D. N., Porter, C. J. H. & Charman, S. A. Subcutaneous drug delivery and the role of the lymphatics. *Drug Discov. Today Technol.* **2**, 89–96 (2005).

44. Liu, H. *et al.* Structure-based programming of lymph-node targeting in molecular vaccines. *Nature* **507**, 519–522 (2014).

45. Hanson, M. C. *et al.* Nanoparticulate STING agonists are potent lymph node-targeted vaccine adjuvants. *J. Clin. Invest.* **125**, 2532–2546 (2015).

46. Smirnov, D., Schmidt, J. J., Capecchi, J. T. & Wightman, P. D. Vaccine adjuvant activity of 3m-052: An imidazoquinoline designed for local activity without systemic cytokine induction. *Vaccine* **29**, 5434–5442 (2011).

47. Reddy, S. T., Rehor, A., Schmoekel, H. G., Hubbell, J. A. & Swartz, M. A. In vivo targeting of dendritic cells in lymph nodes with poly(propylene sulfide) nanoparticles. *J. Control. Release* **112**, 26–34 (2006).

48. Manolova, V. *et al.* Nanoparticles target distinct dendritic cell populations according to their size. *Eur. J. Immunol.* **38**, 1404–1413 (2008).

49. Fifis, T. *et al.* Size-Dependent Immunogenicity: Therapeutic and Protective Properties of Nano-Vaccines against Tumors. *J. Immunol.* **173**, 3148–3154 (2004).

50. Shen, H. *et al.* Enhanced and prolonged cross-presentation following endosomal escape of exogenous antigens encapsulated in biodegradable nanoparticles. *Immunology* **117**, 78–88 (2006).

51. Moon, J. J. *et al.* Interbilayer-crosslinked multilamellar vesicles as synthetic vaccines for potent humoral and cellular immune responses. *Nat. Mater.* **10**, 243–251 (2011).

52. Fang, R. H. *et al.* Cancer cell membrane-coated nanoparticles for anticancer vaccination and drug delivery. *Nano Lett.* **14**, 2181–2188 (2014).

53. Gubin, M. M. *et al.* Checkpoint blockade cancer immunotherapy targets tumour-specific mutant antigens. *Nature* **515**, 577–581 (2014).

54. Hacohen, N., Fritsch, E. F., Carter, T. A., Lander, E. S. & Wu, C. J. Getting personal with neoantigen-based therapeutic cancer vaccines. *Cancer Immunol. Res.* **1**, 11–15 (2013).

55. Fritsch, E. F., Hacohen, N. & Wu, C. J. Personal neoantigen cancer vaccines: The momentum builds. *Oncoimmunology* **3**, (2014).

56. Yadav, M. *et al.* Predicting immunogenic tumour mutations by combining mass spectrometry and exome sequencing. *Nature* **515**, 572–576 (2014).

57. Castle, J. C. *et al.* Exploiting the mutanome for tumor vaccination. *Cancer Res.* **72**, 1081–1091 (2012).

58. Kreiter, S. *et al.* Mutant MHC class II epitopes drive therapeutic immune responses to cancer. *Nature* **520**, 692–696 (2015).

59. Carreno, B. M. *et al.* A dendritic cell vaccine increases the breadth and diversity of melanoma neoantigen-specific T cells. *Science (80-.).* **348**, (2015).

60. Sahin, U. *et al.* Personalized RNA mutanome vaccines mobilize poly-specific therapeutic immunity against cancer. *Nature* **547**, 222–226 (2017).

61. Ott, P. A. *et al.* An immunogenic personal neoantigen vaccine for patients with melanoma. *Nature* **547**, 217–221 (2017).

62. Aldous, A. R. & Dong, J. Z. Personalized neoantigen vaccines: A new approach to cancer immunotherapy. *Bioorganic Med. Chem.* **26**, 2842–2849 (2018).

63. Zhu, G. *et al.* Intertwining DNA-RNA nanocapsules loaded with tumor neoantigens as synergistic nanovaccines for cancer immunotherapy. *Nat. Commun.* **8**, (2017).

64. Kuai, R., Ochyl, L. J., Bahjat, K. S., Schwendeman, A. & Moon, J. J. Designer vaccine nanodiscs for personalized cancer immunotherapy. *Nat. Mater.* **16**, 489–498 (2017).

65. Julien, F. *et al.* Immunization with analogue peptide in combination with CpG and Montanide expands tumor antigen-specific CD8+ T cells in melanoma patients. *J. Immunother.* **31**, 781–791 (2008).

66. Kenter, G. G. *et al.* Vaccination against HPV-16 Oncoproteins for Vulvar Intraepithelial Neoplasia. *N. Engl. J. Med.* **361**, 1838–1847 (2009).

67. Magarian Blander, J. & Medzhitov, R. Toll-dependent selection of microbial antigens for presentation by dendritic cells. *Nature* **440**, 808–812 (2006).

68. Khan, S. *et al.* Distinct uptake mechanisms but similar intracellular processing of two different toll-like receptor ligand-peptide conjugates in dendritic cells. *J. Biol. Chem.* **282**, 21145–21159 (2007).

69. Zom, G. G. *et al.* Efficient induction of antitumor immunity by synthetic toll-like receptor ligand-peptide conjugates. *Cancer Immunol. Res.* **2**, 756–764 (2014).

70. Luo, Y. *et al.* The Dual Role of Lipids of the Lipoproteins in Trumenba, a Self-Adjuvanting Vaccine Against Meningococcal Meningitis B Disease. *AAPS J.* **18**, 1562–1575 (2016).

71. Cai, H. *et al.* Synthetic multivalent glycopeptide-lipopeptide antitumor vaccines: Impact of the cluster effect on the killing of tumor cells. *Angew. Chemie - Int. Ed.* **53**, 1699–1703 (2014).

72. Skakuj, K. *et al.* Conjugation Chemistry-Dependent T-Cell Activation with Spherical Nucleic Acids. *J. Am. Chem. Soc.* **140**, 1227–1230 (2018).

73. Miller, N. E. *et al.* Secretion of adipokines by human adipose tissue in vivo: Partitioning between capillary and lymphatic transport. *Am. J. Physiol. - Endocrinol. Metab.* **301**, 659–667 (2011).

74. Tang, L. *et al.* Aptamer-functionalized, ultra-small, monodisperse silica nanoconjugates for targeted dual-modal imaging of lymph nodes with metastatic tumors. *Angew. Chemie - Int. Ed.* **51**, 12721–12726 (2012).

75. Reddy, S. T. *et al.* Exploiting lymphatic transport and complement activation in nanoparticle

vaccines. *Nat. Biotechnol.* **25**, 1159–1164 (2007).

76. Rosalia, R. A. *et al.* Dendritic cells process synthetic long peptides better than whole protein, improving antigen presentation and T-cell activation. *Eur. J. Immunol.* **43**, 2554–2565 (2013).

77. Bijker, M. S. *et al.* Superior induction of anti-tumor CTL immunity by extended peptide vaccines involves prolonged, DC-focused antigen presentation. *Eur. J. Immunol.* **38**, 1033–1042 (2008).

78. Moyer, T. J., Zmolek, A. C. & Irvine, D. J. Beyond antigens and adjuvants: Formulating future vaccines. *J. Clin. Invest.* **126**, 799–808 (2016).

79. Wadhwa, M. S., Collard, W. T., Adami, R. C., McKenzie, D. L. & Rice, K. G. Peptide-mediated gene delivery: Influence of peptide structure on gene expression. *Bioconjug. Chem.* **8**, 81–88 (1997).

80. Varkouhi, A. K., Scholte, M., Storm, G. & Haisma, H. J. Endosomal escape pathways for delivery of biologicals. *J. Control. Release* **151**, 220–228 (2011).

81. Rudra, J. S., Tian, Y. F., Jung, J. P. & Collier, J. H. A self-assembling peptide acting as an immune adjuvant. *Proc. Natl. Acad. Sci. U. S. A.* **107**, 622–627 (2010).

82. Chiu, Y. C., Gammon, J. M., Andorko, J. I., Tostanoski, L. H. & Jewell, C. M. Modular Vaccine Design Using Carrier-Free Capsules Assembled from Polyionic Immune Signals. *ACS Biomater. Sci. Eng.* **1**, 1200–1205 (2015).

83. Qiu, F. *et al.* Poly(propylacrylic acid)-peptide nanoplexes as a platform for enhancing the immunogenicity of neoantigen cancer vaccines. *Biomaterials* **182**, 82–91 (2018).

84. Qiu, L. *et al.* Endolysosomal-Escape Nanovaccines through Adjuvant-Induced Tumor Antigen Assembly for Enhanced Effector CD8+ T Cell Activation. *Small* **14**, 1–11 (2018).

85. Kramer, K., Shields, N. J., Poppe, V., Young, S. L. & Walker, G. F. Intracellular Cleavable CpG Oligodeoxynucleotide-Antigen Conjugate Enhances Anti-tumor Immunity. *Mol. Ther.* **25**, 62–70 (2017).

86. Tsoras, A. N. & Champion, J. A. Cross-Linked Peptide Nanoclusters for Delivery of Oncofetal Antigen as a Cancer Vaccine. *Bioconjug. Chem.* **29**, 776–785 (2018).

87. Wang, K. *et al.* 'Minimalist' Nanovaccine Constituted from Near Whole Antigen for Cancer Immunotherapy. *ACS Nano* **12**, 6398–6409 (2018).

88. Luo, M. *et al.* A STING-activating nanovaccine for cancer immunotherapy. *Nat. Nanotechnol.* **12**, 648–654 (2017).

89. Li, A. W. *et al.* A facile approach to enhance antigen response for personalized cancer vaccination. *Nat. Mater.* **17**, 528–534 (2018).

90. Wilson, D. S. *et al.* Antigens reversibly conjugated to a polymeric glyco-adjuvant induce protective humoral and cellular immunity. *Nat. Mater.* **18**, 175–185 (2019).

91. Holmes, K. K., Bertozzi, S., Bloom, B. R. & Jha, P. *Major Infectious Diseases*. *Disease Control Priorities (third edition) vol-6* (2017). doi:10.5005/jp/books/11021_11

92. Shretta, R. *et al.* Tracking development assistance and government health expenditures for 35 malaria-eliminating countries: 1990-2017. *Malar. J.* **16**, 1–11 (2017).

93. Madhav, N. *et al.* Chapter 17 - Pandemics: Risks, Impacts, and Mitigation. *Dis. Control Priorities, 3rd Ed. Improv. Heal. reducing poverty* 315–345 (2014).

94. Excler, J. L., Saville, M., Berkley, S. & Kim, J. H. Vaccine development for emerging infectious diseases. *Nat. Med.* **27**, 591–600 (2021).

95. Parpia, A. S., Ndeffo-Mbah, M. L., Wenzel, N. S. & Galvani, A. P. Effects of response to 2014-2015 ebola outbreak on deaths from malaria, HIV/AIDS, and tuberculosis, West Africa. *Emerg. Infect. Dis.* **22**, 433–441 (2016).

96. Pustil, R. L. Global AIDS UPDATE. *AIDS* **17 Suppl 4**, (2016).

97. Ko, K. *et al.* Function and glycosylation of plant-derived antiviral monoclonal antibody. *Proc. Natl. Acad. Sci. U. S. A.* **100**, 8013–8018 (2003).

98. Rofifah, D. Virus Life Cycle. *Mol. Virol. Hum. Pathog. Viruses* 31–45 (2020).

99. Trottier, B. *et al.* new england journal. 2175–2185 (2003).

100. Meanwell, N. A. *et al.* Inhibitors of HIV-1 Attachment: The Discovery and Development of Temsavir and its Prodrug Fostemsavir. *J. Med. Chem.* **61**, 62–80 (2018).

101. Lieberman-Blum, S. S., Fung, H. B. & Bandres, J. C. Maraviroc: A CCR5-receptor antagonist for the treatment of HIV-1 infection. *Clin. Ther.* **30**, 1228–1250 (2008).

102. Bishop, N. E. Examination of potential inhibitors of hepatitis A virus uncoating. *Intervirology* **41**, 261–271 (1998).

103. Almela, M. J., González, M. E. & Carrasco, L. Inhibitors of poliovirus uncoating efficiently block the early membrane permeabilization induced by virus particles. *J. Virol.* **65**, 2572–2577 (1991).

104. Hay, A. J., Wolstenholme, A. J., Skehel, J. J. & Smith, M. H. The molecular basis of the specific anti-influenza action of amantadine. *EMBO J.* **4**, 3021–3024 (1985).

105. Dolin, R. *et al.* A CONTROLLED TRIAL OF AMANTADINE AND RIMANTADINE IN THE PROPHYLAXIS OF INFLUENZA A INFECTION. *N. Engl. J. Med.* **307**, 580–584 (1982).

106. Wagstaff, A. J., Faulds, D. & Goa, K. L. Aciclovir: a reappraisal of its antiviral activity, pharmacokinetic properties and therapeutic efficacy. *Drug Eval.* **47**, 153–205 (1994).

107. Wilde, M. I. & Langtry, H. D. Zidovudine. **46**, 515–578 (1993).

108. Jarvis, B. & Faulds, D. Lamivudine: A review of its therapeutic potential in chronic hepatitis B. *Drugs* **58**, 101–141 (1999).

109. Klumpp, K. *et al.* Two-metal ion mechanism of RNA cleavage by HIV RNase H and mechanism-based design of selective HIV RNase H inhibitors. *Nucleic Acids Res.* **31**, 6852–6859 (2003).

110. Geary, R. S., Henry, S. P. & Grillone, L. R. Fomivirsen: Clinical pharmacology and potential drug interactions. *Clin. Pharmacokinet.* **41**, 255–260 (2002).

111. Stein, D. A., Skilling, D. E., Iversen, P. L. & Smith, A. W. Inhibition of vesivirus infections in mammalian tissue culture with antisense morpholino oligomers. *Antisense Nucleic Acid Drug Dev.* **11**, 317–325 (2001).

112. Deas, T. S. *et al.* Inhibition of Flavivirus Infections by Antisense Oligomers Specifically Suppressing Viral Translation and RNA Replication. *J. Virol.* **79**, 4599–4609 (2005).

113. Kinney, R. M. *et al.* Inhibition of Dengue Virus Serotypes 1 to 4 in Vero Cell Cultures with Morpholino Oligomers. *J. Virol.* **79**, 5116–5128 (2005).

114. Neuman, B. W. *et al.* Antisense Morpholino-Oligomers Directed against the 5′ End of the Genome Inhibit Coronavirus Proliferation and Growth†. *J. Virol.* **78**, 5891–5899 (2004).

115. McCaffrey, A. P., Meuse, L., Karimi, M., Contag, C. H. & Kay, M. A. A potent and specific morpholino antisense inhibitor of hepatitis C translation in mice. *Hepatology* **38**, 503–508 (2003).

116. Ryu, K. J. & Lee, S. W. Identification of the Most Accessible Sites to Ribozymes on the Hepatitis C Virus Internal Ribosome Entry Site. *J. Biochem. Mol. Biol.* **36**, 538–544 (2003).

117. Bai, J., Rossi, J. & Akkina, R. Multivalent anti-CCR5 ribozymes for stem cell-based HIV type 1 gene therapy. *AIDS Res. Hum. Retroviruses* **17**, 385–399 (2001).

118. Kräusslich, H.-G. & Bartenschlager, R. *Anti-viral strategies. Handbook of Experimental Pharmacology* **189**, (2009).

119. Rider, T. H. *et al.* Broad-spectrum antiviral therapeutics. *PLoS One* **6**, (2011).

120. Sodeik, B., Griffiths, G., Ericsson, M., Moss, B. & Doms, R. W. Assembly of vaccinia virus: effects of rifampin on the intracellular distribution of viral protein p65. *J. Virol.* **68**, 1103–1114 (1994).

121. Falke, D. Zanamivir. *Tagliche Prax.* **41**, 403–407 (2000).

122. McClellan, K. & Perry, C. M. Oseltamivir: A review of its use in influenza. *Drugs* **61**, 263–283 (2001).

123. Samuel, C. E. Antiviral actions of interferons. *Clin. Microbiol. Rev.* **14**, 778–809 (2001).

124. Razonable, R. R. Antiviral drugs for viruses other than human immunodeficiency virus. *Mayo Clin. Proc.* **86**, 1009–1026 (2011).

125. Arts, E. J. & Hazuda, D. J. HIV-1 antiretroviral drug therapy. *Cold Spring Harb. Perspect. Med.* **2**, (2012).

126. Gordon, C. J., Tchesnokov, E. P., Schinazi, R. F. & Götte, M. Molnupiravir promotes SARS-CoV-2 mutagenesis via the RNA template. *J. Biol. Chem.* **297**, 100770 (2021).

127. Pelegrin, M., Naranjo-Gomez, M. & Piechaczyk, M. Antiviral Monoclonal Antibodies: Can They Be More Than Simple Neutralizing Agents? *Trends Microbiol.* **23**, 653–665 (2015).

128. Bekerman, E. & Einav, S. Combating emerging viral threats. *Science (80-.).* **348**, 282–283 (2015).

129. Haag, R. & Kratz, F. Polymer therapeutics: Concepts and applications. *Angew. Chemie - Int. Ed.* **45**, 1198–1215 (2006).

130. Fosgerau, K. & Hoffmann, T. Peptide therapeutics: Current status and future directions. *Drug Discov. Today* **20**, 122–128 (2015).

131. Kuroki, A., Tay, J., Lee, G. H. & Yang, Y. Y. Broad-Spectrum Antiviral Peptides and Polymers. *Adv. Healthc. Mater.* **2101113**, 2101113 (2021).

132. Pasut, G. & Veronese, F. M. Polymer-drug conjugation, recent achievements and general strategies. *Prog. Polym. Sci.* **32**, 933–961 (2007).

133. Vlieghe, P. *et al.* Synthesis of new covalently bound κ-carrageenan-AZT conjugates with improved anti-HIV activities. *J. Med. Chem.* **45**, 1275–1283 (2002).

134. Giammona, G., Cavallaro, G., Fontana, G., Pitarresi, G. & Carlisi, B. Coupling of the antiviral agent zidovudine to polyaspartamide and in *vitro* drug release studies. *J. Control. Release* **54**, 321–331 (1998).

135. Du, T. *et al.* Carbon dots as inhibitors of virus by activation of type I interferon response. *Carbon N. Y.* **110**, 278–285 (2016).

136. Iannazzo, D. *et al.* Synthesis and anti-HIV activity of carboxylated and drug-conjugated multi-walled carbon nanotubes. *Carbon N. Y.* **82**, 548–561 (2015).

137. Castro-Mayorga, J. L. *et al.* Antiviral properties of silver nanoparticles against norovirus surrogates and their efficacy in coated polyhydroxyalkanoates systems. *LWT - Food Sci. Technol.* **79**, 503–510 (2017).

138. Galdiero, S. *et al.* Silver nanoparticles as potential antiviral agents. *Molecules* **16**, 8894–8918 (2011).

139. Lee, G. H. *et al.* Antioxidative and antiinflammatory activities of quercetin-loaded silica nanoparticles. *Colloids Surfaces B Biointerfaces* **143**, 511–517 (2016).

140. Lee, M.-Y. *et al.* Hyaluronic Acid À Gold Nanoparticle / Interferon R Complex for Targeted Treatment of Hepatitis C Virus. *ACS Nano* 9522–9531 (2012).

141. Zheng, K., Setyawati, M. I., Leong, D. T. & Xie, J. Antimicrobial Gold Nanoclusters. *ACS Nano* **11**, 6904–6910 (2017).

142. Song, Z. *et al.* Virus capture and destruction by label-free graphene oxide for detection and disinfection applications. *Small* **11**, 1771–1776 (2015).

143. Cagno, V. *et al.* Broad-spectrum non-toxic antiviral nanoparticles with a virucidal inhibition mechanism. *Nat. Mater.* **17**, 195–203 (2018).

144. Takizawa, N. & Yamasaki, M. Current landscape and future prospects of antiviral drugs derived from microbial products. *J. Antibiot. (Tokyo).* **71**, 45–52 (2018).

145. Chaudhuri, S., Symons, J. A. & Deval, J. Innovation and trends in the development and approval of antiviral medicines: 1987–2017 and beyond. *Antiviral Res.* **155**, 76–78 (2018).

146. Pour, P. M., Fakhri, S., Asgary, S., Farzaei, M. H. & Echeverría, J. The signaling pathways, and therapeutic targets of antiviral agents: Focusing on the antiviral approaches and clinical perspectives of anthocyanins in the management of viral diseases. *Front. Pharmacol.* **10**, 1–23 (2019).

147. Richman, D. D. Antiviral drug resistance. *Antiviral Res.* **71**, 117–121 (2006).

148. Cojocaru, F. D. *et al.* Nanomaterials designed for antiviral drug delivery transport across biological barriers. *Pharmaceutics* **12**, 1–34 (2020).

149. Durai, R. D. Drug delivery approaches of an antiviral drug: A comprehensive review. *Asian J. Pharm.* **9**, 1–12 (2015).

150. Chen, R. *et al.* Antiviral drug delivery system for enhanced bioactivity, better metabolism and pharmacokinetic characteristics. *Int. J. Nanomedicine* **16**, 4959–4984 (2021).

151. Vigant, F., Santos, N. C. & Lee, B. Broad-spectrum antivirals against viral fusion. *Nat. Rev. Microbiol.* **13**, 426–437 (2015).

152. Broggi, A., Granucci, F. & Zanoni, I. Type III interferons: Balancing tissue tolerance and resistance to pathogen invasion. *J. Exp. Med.* **217**, 1–12 (2020).

153. Lazear, H. M., Nice, T. J. & Diamond, M. S. Interferon-λ: Immune Functions at Barrier Surfaces and Beyond. *Immunity* **43**, 15–28 (2015).

154. Walker, L. M. & Burton, D. R. Passive immunotherapy of viral infections: 'super-antibodies' enter the fray. *Nat. Rev. Immunol.* **18**, 297–308 (2018).

155. van Riel, D. & de Wit, E. Next-generation vaccine platforms for COVID-19. *Nat. Mater.* **19**, 810–812 (2020).

156. Lembo, D. *et al.* Auto-associative heparin nanoassemblies: A biomimetic platform against the heparan sulfate-dependent viruses HSV-1, HSV-2, HPV-16 and RSV. *Eur. J. Pharm. Biopharm.* **88**, 275–282 (2014).

157. Klimyte, E. M., Smith, S. E., Oreste, P., Lembo, D. & Dutch, R. E. Inhibition of Human Metapneumovirus Binding to Heparan Sulfate Blocks Infection in Human Lung Cells and Airway Tissues. *J. Virol.* **90**, 9237–9250 (2016).

158. Riblett, A. M. *et al.* A Haploid Genetic Screen Identifies Heparan Sulfate Proteoglycans Supporting Rift Valley Fever Virus Infection. *J. Virol.* **90**, 1414–1423 (2016).

159. Bergstrom, D. E. *et al.* Polysulfonates derived from metal thiolate complexes as inhibitors of HIV-1 and various other enveloped viruses in *vitro*. *Antivir. Chem. Chemother.* **13**, 185–195 (2002).

160. De Souza E Silva, J. M. *et al.* Viral Inhibition Mechanism Mediated by Surface-Modified Silica Nanoparticles. *ACS Appl. Mater. Interfaces* **8**, 16564–16572 (2016).

161. Broglie, J. J. *et al.* Antiviral activity of gold/copper sulfide core/shell nanoparticles against human norovirus virus-like particles. *PLoS One* **10**, 1–14 (2015).

162. Chakrabarty, A. N., Mookerjee, M. & Dastidar, S. G. Screening for anti-HIV drugs that can combine virucidal and virustatic activities synergistically. *Int. J. Antimicrob. Agents* **14**, 215–220 (2000).

163. Sung, H. *et al.* Global Cancer Statistics 2020: GLOBOCAN Estimates of Incidence and Mortality Worldwide for 36 Cancers in 185 Countries. *CA: A Cancer Journal for Clinicians* **71**, 209–249 (2021).

164. Sawyers, C. L. The cancer biomarker problem. *Nature* **452**, 548–552 (2008).

165. Golubnitschaja, O. & Flammer, J. What Are the Biomarkers for Glaucoma? *Surv. Ophthalmol.* **52**, 155–161 (2007).

166. Thorlacius, S. *et al.* Population-based study of risk of breast cancer in carriers of BRCA2 mutation. *Lancet* **352**, 1337–1339 (1998).

167. Bertok, T. *et al.* Novel prostate cancer biomarkers: Aetiology, clinical performance and sensing applications. *Chemosensors* **9**, (2021).

168. Khafaei, M., Miri, A., Kiani, E., Danesh, E. & Naderi, M. Early diagnostic biomarkers of Lung cancer; a review study. *Cent. Asian J. Med. Pharm. Sci. Innov.* **1**, 114–130 (2021).

169. Adamaki, M. & Zoumpourlis, V. Prostate Cancer Biomarkers: From diagnosis to prognosis and precision-guided therapeutics. *Pharmacol. Ther.* **228**, 107932 (2021).

170. Kartikasari, A. E. R., Huertas, C. S., Mitchell, A. & Plebanski, M. Tumor-Induced Inflammatory Cytokines and the Emerging Diagnostic Devices for Cancer Detection and Prognosis. *Front. Oncol.* **11**, 1–16 (2021).

171. Xiao, Q. *et al.* High-throughput proteomics and AI for cancer biomarker discovery. *Adv. Drug Deliv. Rev.* **176**, 113844 (2021).

172. Wankhede, N. L. *et al.* Advances in Bioresearch Biomarkers of cancer : A Comprehensive Review. (2021). doi:10.15515/abr.0976-4585.12.1.221233

173. Shaw, R. J. Glucose metabolism and cancer. *Curr. Opin. Cell Biol.* **18**, 598–608 (2006).

174. Yu, M. Circulating cell-free mitochondrial DNA as a novel cancer biomarker: Opportunities and challenges. *Mitochondrial DNA* **23**, 329–332 (2012).

175. Jakupciak, J. P. *et al.* Mitochondrial DNA as a cancer biomarker. *J. Mol. Diagnostics* **7**, 258–267 (2005).

176. Ellinger, J. *et al.* Circulating mitochondrial DNA in serum: A universal diagnostic biomarker for patients with urological malignancies. *Urol. Oncol. Semin. Orig. Investig.* **30**, 509–515 (2012).

177. Hay, N. & Sonenberg, N. Upstream and downstream of mTOR. *Genes Dev.* **18**, 1926–1945 (2004).

178. Tee, A. R. & Proud, C. G. Staurosporine inhibits phosphorylation of translational regulators linked to mTOR. *Cell Death Differ.* **8**, 841–849 (2001).

179. Baselga, J. Targeting tyrosine kinases in cancer: The second wave. *Science (80-.).* **312**, 1175–1178 (2006).

180. Blackburn, E. H. Telomere states and cell fates. *Nature* **408**, 53–56 (2000).

181. Saffroy, R. *et al.* New perspectives and strategy research biomarkers for hepatocellular carcinoma. *Clin. Chem. Lab. Med.* **45**, 1169–1179 (2007).

182. Tornesello, M. L., Buonaguro, L., Giorgi-Rossi, P. & Buonaguro, F. M. Viral and cellular biomarkers in the diagnosis of cervical intraepithelial neoplasia and cancer. *Biomed Res. Int.* **2013**, (2013).

183. Desmetz, C., Mange, A., Maudelonde, T. & Solassol, J. Autoantibody signatures: Progress and perspectives for early cancer detection. *J. Cell. Mol. Med.* **15**, 2013–2024 (2011).

184. Garnis, C. & Lam, W. L. Genetic alteration and gene expression modulation during cancer progression. *Mol. Cancer* **23**, 1–23 (2004).

185. Baylin, S. B. & Ohm, J. E. Epigenetic gene silencing in cancer - A mechanism for early oncogenic pathway addiction? *Nat. Rev. Cancer* **6**, 107–116 (2006).

186. Fearon, E. R. Molecular genetics of colorectal cancer. *Annu. Rev. Pathol. Mech. Dis.* **6**, 479–507 (2011).

187. Sekido, Y., Fong, K. M. & Minna, J. D. Molecular Genetics of Lung Cancer. *Annu. Rev. Med.* **54**, 73–87 (2003).

188. Elo, J. P. & Visakorpi, T. Molecular genetics of prostate cancer. *Ann. Med.* **33**, 130–141 (2001).

189. Oren, M. Decision making by p53: Life, death and cancer. *Cell Death Differ.* **10**, 431–442 (2003).

190. Muller, P. A. J. & Vousden, K. H. P53 mutations in cancer. *Nat. Cell Biol.* **15**, 2–8 (2013).

191. Henry, N. L. & Hayes, D. F. Cancer biomarkers. *Mol. Oncol.* **6**, 140–146 (2012).

192. Ostrow, K. L. *et al.* Molecular analysis of plasma DNA for the early detection of lung cancer by quantitative methylation-specific PCR. *Clin. Cancer Res.* **16**, 3463–3472 (2010).

193. Xiao, S., Wang, J. & Xiao, N. Micro RNAs as noninvasive biomarkers in bladder cancer detection: A diagnostic meta-analysis based on qRT-PCR data. *Int. J. Biol. Markers* **31**, e276–e285 (2016).

194. Kristensen, L. S. & Hansen, L. L. PCR-based methods for detecting single-locus DNA methylation biomarkers in cancer diagnostics, prognostics, and response to treatment. *Clin.*

Chem. **55**, 1471–1483 (2009).

195. Arya, S. K. & Estrela, P. Recent advances in enhancement strategies for electrochemical ELISA-based immunoassays for cancer biomarker detection. *Sensors (Switzerland)* **18**, (2018).

196. Kondo, T. Cancer biomarker development and two-dimensional difference gel electrophoresis (2D-DIGE). *Biochim. Biophys. Acta - Proteins Proteomics* **1867**, 2–8 (2019).

197. Wang, H., Wu, T., Li, M. & Tao, Y. Recent advances in nanomaterials for colorimetric cancer detection. *J. Mater. Chem. B* **9**, 921–938 (2021).

198. Bellassai, N., D'Agata, R., Jungbluth, V. & Spoto, G. Surface Plasmon Resonance for Biomarker Detection: Advances in Non-invasive Cancer Diagnosis. *Front. Chem.* **7**, 1–16 (2019).

199. Law, W. C., Yong, K. T., Baev, A. & Prasad, P. N. Sensitivity improved surface plasmon resonance biosensor for cancer biomarker detection based on plasmonic enhancement. *ACS Nano* **5**, 4858–4864 (2011).

200. Guerrini, L. & Alvarez-Puebla, R. A. Surface-enhanced raman spectroscopy in cancer diagnosis, prognosis and monitoring. *Cancers (Basel).* **11**, 1–15 (2019).

201. Lin, T. *et al.* Mass spectrometry-based targeted proteomics for analysis of protein mutations. *Mass Spectrom. Rev.* (2021). doi:10.1002/mas.21741

202. Zhang, T., He, Y., Wei, J. & Que, L. Nanostructured optical microchips for cancer biomarker detection. *Biosens. Bioelectron.* **38**, 382–388 (2012).

203. Kiio, L. K., Mbui, D. N., Ndangili, P. M., Onam, O. J. & Oloo, F. Current Biosensors Used for Early Detection of Lung Cancer Biomarkers. *Sci. Res. Community* **3**, 1–8 (2021).

204. Soda, N., Rehm, B. H. A., Sonar, P., Nguyen, N. T. & Shiddiky, M. J. A. Advanced liquid biopsy technologies for circulating biomarker detection. *J. Mater. Chem. B* **7**, 6670–6704 (2019).

205. Xu, J. J., Zhao, W. W., Song, S., Fan, C. & Chen, H. Y. Functional nanoprobes for ultrasensitive detection of biomolecules: An update. *Chem. Soc. Rev.* **43**, 1601–1611 (2014).

206. De La Rica, R. & Stevens, M. M. Plasmonic ELISA for the ultrasensitive detection of disease biomarkers with the naked eye. *Nat. Nanotechnol.* **7**, 821–824 (2012).

207. Gao, Z., Hou, L., Xu, M. & Tang, D. Enhanced Colorimetric Immunoassay Accompanying with

Enzyme Cascade Amplification Strategy for Ultrasensitive Detection of Low-Abundance Protein. *Sci. Rep.* **4**, 1–8 (2015).

208. Feng, L. *et al.* Detection of a prognostic indicator in early-stage cancer using functionalized graphene-based peptide sensors. *Adv. Mater.* **24**, 125–131 (2012).

209. Syedmoradi, L., Ahmadi, A., Norton, M. L. & Omidfar, K. A review on nanomaterial-based field effect transistor technology for biomarker detection. *Microchim. Acta* **186**, (2019).

210. Garcia-Cordero, J. L. & Maerkl, S. J. Microfluidic systems for cancer diagnostics. *Curr. Opin. Biotechnol.* **65**, 37–44 (2020).

211. Tang, C. K., Vaze, A., Shen, M. & Rusling, J. F. High-Throughput Electrochemical Microfluidic Immunoarray for Multiplexed Detection of Cancer Biomarker Proteins. *ACS Sensors* **1**, 1036–1043 (2016).

212. Sardesai, N. P., Kadimisetty, K., Faria, R. & Rusling, J. F. A microfluidic electrochemiluminescent device for detecting cancer biomarker proteins. *Anal. Bioanal. Chem.* **405**, 3831–3838 (2013).

213. Chikkaveeraiah, B. V., Mani, V., Patel, V., Gutkind, J. S. & Rusling, J. F. Microfluidic electrochemical immunoarray for ultrasensitive detection of two cancer biomarker proteins in serum. *Biosens. Bioelectron.* **26**, 4477–4483 (2011).

214. Agasti, S. S., Liong, M., Peterson, V. M., Lee, H. & Weissleder, R. Photocleavable DNA barcode-antibody conjugates allow sensitive and multiplexed protein analysis in single cell NIH Public Access $watermark-text $watermark-text $watermark-text. *J Am Chem Soc* **134**, 18499–18502 (2012).

215. Geißler, D., Stufler, S., Löhmannsröben, H. G. & Hildebrandt, N. Six-Color time-resolved förster resonance energy transfer for ultrasensitive multiplexed biosensing. *J. Am. Chem. Soc.* **135**, 1102–1109 (2013).

216. Im, H. *et al.* Label-free detection and molecular profiling of exosomes with a nano-plasmonic sensor. *Nat. Biotechnol.* **32**, 490–495 (2014).

217. Tabakman, S. M. *et al.* Plasmonic substrates for multiplexed protein microarrays with femtomolar sensitivity and broad dynamic range. *Nat. Commun.* **13**, 466 (2011).

218. Sinclair, J. & Timms, J. F. Quantitative profiling of serum samples using TMT protein labelling, fractionation and LC-MS/MS. *Methods* **54**, 361–369 (2011).

219. Rauniyar, N. & Yates, J. R. Isobaric labeling-based relative quantification in shotgun proteomics. *J. Proteome Res.* **13**, 5293–5309 (2014).

220. Bouchal, P. *et al.* Biomarker discovery in low-grade breast cancer using isobaric stable isotope tags and two-dimensional liquid chromatography-tandem mass spectrometry (iTRAQ-2DLC-MS/MS) based quantitative proteomic analysis. *J. Proteome Res.* **8**, 362–373 (2009).

221. Cedervall, T. *et al.* Understanding the nanoparticle-protein corona using methods to quntify exchange rates and affinities of proteins for nanoparticles. *Proc. Natl. Acad. Sci. U. S. A.* **104**, 2050–2055 (2007).

222. Hadjidemetriou, M., Al-ahmady, Z., Buggio, M., Swift, J. & Kostarelos, K. A novel scavenging tool for cancer biomarker discovery based on the blood-circulating nanoparticle protein corona. *Biomaterials* **188**, 118–129 (2019).

223. Hadjidemetriou, M. & Kostarelos, K. Nanomedicine: Evolution of the nanoparticle corona. *Nat. Nanotechnol.* **12**, 288–290 (2017).

224. Palchetti, S., Pozzi, D., Mahmoudi, M. & Caracciolo, G. Exploitation of nanoparticle-protein corona for emerging therapeutic and diagnostic applications. *J. Mater. Chem. B* **4**, 4376–4381 (2016).

225. Chapman, M. J., Goldstein, S., Lagrange, D. & Laplaud, P. M. A density gradient ultracentrifugal procedure for the isolation of the major lipoprotein classes from human serum. *J. Lipid Res.* **22**, 339–358 (1981).

226. Terpstra, A. H. M., Woodward, C. J. H. & Sanchez-Muniz, F. J. Sudan black B was obtained from George T. Gurr Ltd., London SW6, England. Ethylene glycol was from Boom B. V., 7940. *Anal. Biochem.* **111**, 149–157 (1981).

227. DELALLA, O. F., ELLIOTT, H. A. & GOFMAN, J. W. Ultracentrifugal studies of high density serum lipoproteins in clinically healthy adults. *Am. J. Physiol.* **179**, 333–337 (1954).

228. Lalla, O. de & Gofman, J. W. Ultracentrifugal Analysis of serum Lipoproteins. **82**, 2–36 (1953).

229. Gofman, J. W., Lindgren, F. T. & Elliott, H. Ultracentrifugal Studies of Lipoproteins of Human

Serum. *J. Biol. Chem.* (1949).

230. Skipski, V. P. *et al.* Lipid composition of human serum lipoproteins. *Biochem. J.* **104**, 340–352 (1967).

231. Shen, B. W., Scanu, A. M. & Kezdy, F. J. Structure of human serum lipoproteins inferred from compositional analysis. *Proc. Natl. Acad. Sci. U. S. A.* **74**, 837–841 (1977).

232. Warnick, G. R., Benderson, J. & Albers, J. J. Dextran sulfate-Mg2+ precipitation procedure for quantitation of high-density-lipoprotein cholesterol. *Clin. Chem.* **28**, 1379–1388 (1982).

233. Harris, N. *et al.* Three generations of high-density lipoprotein cholesterol assays compared with ultracentrifugation/dextran sulfate-Mg2+ method. *Clin. Chem.* **43**, 816–823 (1997).

234. Warnick, G. R., Nguyen, T. & Albers, A. A. Comparison of improved precipitation methods for quantification of high-density lipoprotein cholesterol. *Clin. Chem.* **31**, 217–222 (1985).

235. Mayfield, C., Warnick, G. R. & Albers, J. J. Evaluation of commercial heparin preparations for use in the heparin-Mn2+ method for measuring cholesterol in high-sensity lipoprotein. *Clin. Chem.* **25**, 1309–1313 (1979).

236. Warnick, G. R. & Albers, J. J. Heparin--Mn2+ quantitation of high-density-lipoprotein cholesterol: an ultrafiltration procedure for lipemic samples. *Clin. Chem.* **24**, 900–904 (1978).

237. Albers, J. J. *et al.* Multi-laboratory comparison of three heparin-Mn2+ precipitation procedures for estimating cholesterol in high-density lipoprotein. *Clin. Chem.* **24**, 853–856 (1978).

238. Tsai, L. Y., Peng, M. R., Tsai, S. M. & Hsieh, S. F. The determination of high density lipoprotein cholesterol separated by electrophoresis and sodium phosphotungstate/Mg2+ precipitation: a physical evaluation. *Gaoxiong Yi Xue Ke Xue Za Zhi* **5**, 498—504 (1989).

239. Russell Warnick, G., Mayfield, C., Benderson, J., Chen, J.-S. & Albers, J. J. HDL Cholesterol Quantitation by Phosphotungstate-Mg2+ and by Dextran Sulfate-Mn2+-Polyethylene Glycol Precipitation, Both with Enzymic Cholesterol Assay Compared with the Lipid Research Method. *Am. J. Clin. Pathol.* **78**, 718–723 (1982).

240. Izzo, C., Grillo, F. & Murador, E. Improved method for determination of high-density-lipoprotein cholesterol I. Isolation of high-density lipoproteins by use of polyethylene glycol 6000. *Clin. Chem.* **27**, 371–374 (1981).

241. Briggs, C. J., Anderson, D., Johnson, P. & Deegan, T. Evaluation of the Polyethylene Glycol Precipitation Method for the Estimation of High-Density Lipoprotein Cholesterol. *Ann. Clin. Biochem.* **18**, 177–181 (1981).

242. Viikari, J. Precipitation of Plasma Lipoproteins by PEG-6000 and Its Evaluation with Electrophoresis and Ultracentrifugation. *Scand. J. Clin. Lab. Invest.* **36**, 265–268 (1976).

243. Jeyarajah, E. J., Cromwell, W. C. & Otvos, J. D. Lipoprotein Particle Analysis by Nuclear Magnetic Resonance Spectroscopy. *Clin. Lab. Med.* **26**, 847–870 (2006).

244. Baumstark, D. *et al.* 1H NMR spectroscopy quantifies visibility of lipoproteins, subclasses, and lipids at varied temperatures and pressures. *J. Lipid Res.* **60**, 1516–1534 (2019).

245. Dyrby, M. *et al.* Analysis of lipoproteins using 2D diffusion-edited NMR spectroscopy and multi-way chemometrics. *Anal. Chim. Acta* **531**, 209–216 (2005).

246. Laggner, P. & Müller, K. W. The structure of serum lipoproteins as analysed by X-ray small-angle scattering. *Q. Rev. Biophys.* **11**, 371–425 (1978).

247. LAGGNER, P. *et al.* The Lipid Bilayer Structure of the Abnormal Human Plasma Lipoprotein X: An X-Ray Small-Angle-Scattering Study. *Eur. J. Biochem.* **77**, 165–171 (1977).

248. Kamstrup, P. R. Lipoprotein(a) and Cardiovascular Disease. *Clin. Chem.* **67**, 154–166 (2021).

249. Tsimikas, S. *et al.* Lipoprotein(a) Reduction in Persons with Cardiovascular Disease. *N. Engl. J. Med.* **382**, 244–255 (2020).

250. Anuurad, E., Boffa, M. B., Koschinsky, M. L. & Berglund, L. Lipoprotein(a): A Unique Risk Factor for Cardiovascular Disease. *Clin. Lab. Med.* **26**, 751–772 (2006).

251. Gordon, D. J. *et al.* High-density lipoprotein cholesterol and cardiovascular disease. Four prospective American studies. *Circulation* **79**, 8–15 (1989).

252. Krauss, R. M. Lipoprotein subfractions and cardiovascular disease risk. *Curr. Opin. Lipidol.* **21**, (2010).

253. Chen, J. *et al.* High density lipoprotein mimicking nanoparticles for atherosclerosis. *Nano Converg.* **7**, 1–14 (2020).

254. Woo, J. *et al.* Hypertension, lipoprotein(A), and apolipoprotein a-i as risk factors for stroke in

the chinese. *Stroke* **22**, 203–208 (1991).

255. FROSTEGÅRD, J. *et al.* Circulating oxidized low-density lipoprotein is increased in hypertension. *Clin. Sci.* **105**, 615–620 (2003).

256. Heresi, G. A., Aytekin, M., Newman, J., DiDonato, J. & Dweik, R. A. Plasma levels of high-density lipoprotein cholesterol and outcomes in pulmonary arterial hypertension. *Am. J. Respir. Crit. Care Med.* **182**, 661–668 (2010).

257. Drew, B. G. *et al.* High-density lipoprotein modulates glucose metabolism in patients with type 2 diabetes mellitus. *Circulation* **119**, 2103–2111 (2009).

258. Brown, W. V. Lipoprotein disorders in diabetes mellitus. *Med. Clin. North Am.* **78**, 143–161 (1994).

259. Taskinen, M. R. Quantitative and qualitative lipoprotein abnormalities in diabetes mellitus. *Diabetes* **41**, 12–17 (1992).

260. Howard, B. V. Lipoprotein metabolism in diabetes mellitus. *J. Lipid Res.* **28**, 613–628 (1987).

261. Nikolic, D. *et al.* Lipoprotein subfractisons in metabolic syndrome and obesity: Clinical significance and therapeutic approaches. *Nutrients* **5**, 928–948 (2013).

262. Mooradian, A. D., Haas, M. J., Wehmeier, K. R. & Wong, N. C. W. Obesity-related changes in high-density lipoprotein metabolism. *Obesity* **16**, 1152–1160 (2008).

263. Greene, N. P., Martin, S. E. & Crouse, S. F. Acute exercise and training alter blood lipid and lipoprotein profiles differently in overweight and obese men and women. *Obesity* **20**, 1618–1627 (2012).

264. Solfrizzi, V. *et al.* Lipoprotein(a), apolipoprotein E genotype, and risk of Alzheimer's disease. *J. Neurol. Neurosurg. Psychiatry* **72**, 732–736 (2002).

265. Schippling, S. *et al.* Increased Lipoprotein Oxidation in Alzheimer's Disease. *Free Radic. Biol. Med.* **28**, 351–360 (2000).

266. Walley, K. R., Boyd, J. H., Kong, H. J. & Russell, J. A. Low Low-Density Lipoprotein Levels Are Associated With, But Do Not Causally Contribute to, Increased Mortality in Sepsis*. *Crit. Care Med.* **47**, (2019).

267. Trinder, M. *et al.* Cholesteryl ester transfer protein influences high-density lipoprotein levels and survival in sepsis. *Am. J. Respir. Crit. Care Med.* **199**, 854–862 (2019).

268. Chien, J.-Y., Jerng, J.-S., Yu, C.-J. & Yang, P.-C. Low serum level of high-density lipoprotein cholesterol is a poor prognostic factor for severe sepsis*. *Crit. Care Med.* **33**, (2005).

269. Sakaguchi, S. Metabolic Disorders of Serum Lipoproteins in Endotoxin-Poisoned Mice: The Role of High Density Lipoprotein (HDL) and Triglyceride-Rich Lipoproteins. *Microbiol. Immunol.* **26**, 1017–1034 (1982).

270. Sud, N., Taher, J. & Su, Q. MicroRNAs and Noncoding RNAs in Hepatic Lipid and Lipoprotein Metabolism: Potential Therapeutic Targets of Metabolic Disorders. *Drug Dev. Res.* **76**, 318–327 (2015).

271. Yu, Y., Raka, F. & Adeli, K. The role of the gut microbiota in lipid and lipoprotein metabolism. *J. Clin. Med.* **8**, (2019).

272. Iqbal, J., Walsh, M. T., Hammad, S. M. & Hussain, M. M. Sphingolipids and Lipoproteins in Health and Metabolic Disorders. *Trends Endocrinol. Metab.* **28**, 506–518 (2017).

273. Alsheikh-Ali, A. A., Trikalinos, T. A., Kent, D. M. & Karas, R. H. Statins, Low-Density Lipoprotein Cholesterol, and Risk of Cancer. *J. Am. Coll. Cardiol.* **52**, 1141–1147 (2008).

274. Kritchevsky, S. B., Truong, K. N. & Tyroler, H. A. Changes in Plasma Lipid and Lipoprotein Cholesterol and Weight prior to the Diagnosis of Cancer. *Cancer Res.* **51**, 3198–3203 (1991).

275. Ganjali, S. *et al.* High-Density Lipoprotein Components and Functionality in Cancer: State-of-the-Art. *Trends Endocrinol. Metab.* **30**, 12–24 (2019).

276. Alexopoulos, C. G., Blatsios, B. & Avgerinos, A. Serum lipids and lipoprotein disorders in cancer patients. *Cancer* **60**, 3065–3070 (1987).

277. Hospital, G. S. & Branchi, A. Serum lipoprotein profile in patients with A comparison with non-cancer subjects. *Int J Clin Lab Res* **30**, 141–145 (2000).

278. Tan, T. *et al.* Targeting peptide-decorated biomimetic lipoproteins improve deep penetration and cancer cells accessibility in solid tumor. *Acta Pharm. Sin. B* **10**, 529–545 (2020).

279. Mirzaei, M. *et al.* New nanoprobe for breast cancer cell imaging based on low-density lipoprotein. *Artif. Cells, Nanomedicine Biotechnol.* **48**, 46–52 (2020).

280. Bruns, O. T. *et al.* Real-time magnetic resonance imaging and quantification of lipoprotein metabolism in vivo using nanocrystals. *Nat. Nanotechnol.* **4**, 193–201 (2009).

281. Ng, K. K., Lovell, J. F. & Zheng, G. Lipoprotein-inspired nanoparticles for cancer theranostics. *Acc. Chem. Res.* **44**, 1105–1113 (2011).

282. Johnsen, K. B., Gudbergsson, J. M., Andresen, T. L. & Simonsen, J. B. What is the blood concentration of extracellular vesicles? Implications for the use of extracellular vesicles as blood-borne biomarkers of cancer. *Biochim. Biophys. Acta - Rev. Cancer* **1871**, 109–116 (2019).

283. Wiśniewski, J. R., Zougman, A., Nagaraj, N. & Mann, M. Universal sample preparation method for proteome analysis. *Nat. Methods* **6**, 359–362 (2009).

284. Rappsilber, J., Mann, M. & Ishihama, Y. Protocol for micro-purification, enrichment, pre-fractionation and storage of peptides for proteomics using StageTips. *Nat. Protoc.* **2**, 1896–1906 (2007).

285. Dorfer, V. *et al.* MS Amanda, a universal identification algorithm optimized for high accuracy tandem mass spectra. *J. Proteome Res.* **13**, 3679–3684 (2014).

286. Kong, A. T., Leprevost, F. V., Avtonomov, D. M., Mellacheruvu, D. & Nesvizhskii, A. I. MSFragger: Ultrafast and comprehensive peptide identification in mass spectrometry-based proteomics. *Nat. Methods* **14**, 513–520 (2017).

287. Plubell, D. L. *et al.* Extended multiplexing of tandem mass tags (TMT) labeling reveals age and high fat diet specific proteome changes in mouse epididymal adipose tissue. *Mol. Cell. Proteomics* **16**, 873–890 (2017).

288. Robinson, M. D., McCarthy, D. J. & Smyth, G. K. edgeR: A Bioconductor package for differential expression analysis of digital gene expression data. *Bioinformatics* **26**, 139–140 (2009).

289. Ritchie, M. E. *et al.* Limma powers differential expression analyses for RNA-sequencing and microarray studies. *Nucleic Acids Res.* **43**, e47 (2015).

290. Klipper-Aurbach, Y. *et al.* Mathematical formulae for the prediction of the residual beta cell function during the first two years of disease in children and adolescents with insulin-dependent diabetes mellitus. *Med. Hypotheses* **45**, 486–490 (1995).

291. Vartak, A. & Sucheck, S. J. Recent advances in subunit vaccine carriers. *Vaccines* **4**, 1–18 (2016).

292. Han, X., Xu, P. & Ye, Q. Analysis of COVID-19 vaccines: Types, thoughts, and application. *J. Clin. Lab. Anal.* **35**, 1–7 (2021).

293. Brisse, M., Vrba, S. M., Kirk, N., Liang, Y. & Ly, H. Emerging Concepts and Technologies in Vaccine Development. *Front. Immunol.* **11**, 1–22 (2020).

Lixia Wei

Route Cantonal 37
1025 St-Sulpice, Vaud
Permit B
078 710 33 48
cathy.wei112@gmail.com
www.linkedin.com/in/lixia-wei-a7577699

Strength

- **Expertise in Immuno-Oncology, Vaccine, Cancer Biomarker Diagnosis**
- **Over 9 years of Lab research and 2 years of full-time Industry work**
- **Three Patents (two filed and one applying), the European Patent about Cancer vaccine attracts Venture Kick for financing to be a start-up company**
- **5 years of extensive management experience of research projects, good integration and communication skills**

Education

2017 – 2022 **EPFL (École polytechnique fédérale de Lausanne)**, Lausanne, Switzerland
Ph.D. - Immuno Oncology I Vaccine I Cancer biomarker diagnosis
– Best Poster Award in 5th International Symposium of the SFB 765 "Multivalency in Chemistry and Biology"

2013 – 2015 **ENS (École Normale Supérieure Paris-Saclay)**, Paris, France
Master of Science - MSc in molecular bio- & nano-photonics for biomedical application
– Ranking 2/37, Award: Category A scholarship from European Union

2006 – 2010 **Southwest University**, Chongqing, China
Bachelor of Science - BSc in Pharmaceutical Engineering
– Ranking 1/72, Award: Outstanding Graduates, Excellent Individual of Scientific and Technological Innovation

Professional experience

2017 – 2022 **Ph.D Research Fellow, Group SuNMIL and LBI**, EPFL, Lausanne, Switzerland
Lead Research Projects:
– Personalized cancer nanovaccine development
Works including vaccine formulation, analytical characterization, in vitro assay on primary immune cells (DC, B, T cells), pre-clinical in vivo immunization on animals.
– Cancer biomarker diagnosis
Work including diagnosis method establishment (serum nanoparticle extraction), analytical characterization, quality control, cancer biomarker profiling and analysis.
– Broad-Spectrum anti-viral drug development
Work including establish a customizable modification platform with protein and lipipeptide for broad-spectrum anti-viral purpose, formulation form, analytical characterization and antiviral effect evaluation.
Collaborative Project:
– Novel mRNA delivery system development
Work including involving scientific design, bio-analytical evaluation in vitro and accordingly improvement.
– Customizable protein scaffold platform for drug formulation
Work including engineering a customizable modification platform for installing new function onto protein scaffolds and demonstrate its utility in both antiviral and therapeutic protein delivery application.

2014 - 2015 **Master Research Fellow, Gustave Roussy**, CNRS, Paris, France
Research Project: Therapeutic electroporation for cancer drug delivery & treatment. Lead a sub-project to understand the mechanism of cell dealth by assessment of ER (endoplasmic reticulum) stress triggered by electric pulse delivery to human tumor cells

07-09 - 2014 **Master Research Fellow, Rice University**, Houston, U.S
Research project: NIR (Near-infrared) light triggered cancer drug release from gold (Au) nanoshell for drug delivery and cancer treatment. Work including investigating the binding mechanism between a poorly soluble cancer drug (Lapatinib) and double stranded DNA, drug release assay with NIR light.

01-07 - 2013 **Research Project Management assistant, Shanghai Tin Tsz Bio Valley Biological Engineering Co Ltd**, Shanghai, China

Responsible for part of grant proposal writing, arrangement of the research team daily distribution, advising and ordering research materials, tracking and report projects progress.

2011 – 2012 **Research Assistant, Chinese Academy of Science**, Shanghai, China

Responsible for a cooperative Project "Organic synthesis of potential drugs for cancer disease" with Les Laboratories Servier (France)

Works including synthesis a series of structurally diverse N-cinnamyl propane diamine compounds for the pharmaceutical bioactivity test in Les Laboratories Servier, and the successive structure modifications according to their results.

2009 - 2010 **Bachelor Research Fellow, Chongqing Daxin Pharmaceutical Co Ltd.**, Chongqing, China

Research Project: Separation and purification of antibiotics vancomycin from its fermented liquid by a simple, easy operated method-connection resin technology. (**Award**: Excellent Dissertations Appraisal)

Work including develop a simple and easy technology for purifying antibiotics vancomycin from fermentation, optimize each step operation parameters, improve the massive production in industry.

Publications & Patents

Patents **European Patent: Polymer or Polycondensate Based on Peptide, Linker and Optionally Other Monomers Method for Preparing the Same**

EP Application Nr: 19198817.9; Inventors: Li Tang, **Lixia Wei**, Yu Zhao. Filed on: 20.09.2019

Chinese National Patent: Method for Preparing Health-care Foods with Different Activities by Comprehensively Using Cornus Officinalis Glycosides

CN Application Nr: CN 201010162460.6; Inventors: Jun Deng, Jiaxu Wen, **Lixia Wei**. Filed on 30.04.2010

Publications **Lixia Wei**, Yu Zhao, Xiaomeng Hu, and Li Tang. Redox-Responsive Polycondensate Neoepitope for Enhanced Personalized Cancer Vaccine. ACS Central Science 2020 6 (3), 404-412

Suiyang Liao, **Lixia Wei**, Luciano A. Abriata, Francesco Stellacci. Control and Characterization of the Compactness of Single-Chain Nanoparticles. Macromolecules, 2021,54,24, 11459-11467

Xie YQ, Arik H, **Wei L**, Zheng Y, Suh H, Irvine DJ, Tang L. Redox-responsive interleukin-2 nanogel specifically and safely promotes the proliferation and memory precursor differentiation of tumor-reactive T-cells. Biomater. Sci., 2019,7, 1345-1357

Yu-Qing Xie, **Lixia Wei**, Li Tang. Immunoengineering with biomaterials for enhanced cancer immunotherapy. Wiley Interdiscip Rev Nanomed Nanobiotechnol. 2018, 10(4):e1506

Technical Skills

Laboratory
- Chemical organic synthesis and characterization such as HPLC, NMR, TLC, silica & resin column purification skills.
- Cell culture, in vitro cell related assays including "Drug cytotoxicity test", "Drug cell penetration", "Immune stimulation" "Drug antiviral dose-response and virucidal test", etc.
- Classical assays including PCR & RT-PCR, ELISA, SDS-PAGE, Western blot, etc.
- Fluent use instruments including "Flow Cytometry, Confocal Microscopy, Plate Reader, Dynamic lighter scattering (DLS), Z-potential, Transmission Electron Microscopy (TEM), etc."
- Licensed certificate to work with mice animals, perform injection, sacrifice, imaging, tissue processing

Computer
- Proficient use all related types of research and data analysis softwares including ChemDraw, MestReNova, Fiji, Prism, Origin, etc. General office softwares.

Soft skill
- Years of Lab management experiences, Effective and efficient scientific communication, Good intercultural intergration

Licenses & certifications

Drug and Device Product Development and Regulation in Europe and the United States, Issued Oct 2019 by San Diego State University and EPFL

RESAL Module 1: Introductory Course in Laboratory Animal Science, Issued Jun 2017 by Federation of European Laboratory Animal Science Associations

Python Fundamentals: Issued Feb 2022 by EPFL (Learning & Development)

Professional Photography: Graduation Certificate, Issued Dec 2021 by New York Institute of Photography

Languages

English: Full proficiency C1, **French**: Elemenary proficiency A2, **Chinese**: Native

Extra-curricular activities

Indoor and ourdoor climbing, Skiing, Hiking, Table tennis, Caligraphy, Photography